Mass generation in graphene and kagome metals

Supervisors:

Dr. Lars Fritz
Dr. Dirk Schuricht

Student:

Simone Ciceri
Student number 0592072

YEAR 2022-2023

Abstract

Kagome materials received profound attention in recent years, becoming some of the most prominent structures in condensed matter theory. They have been proposed as hosts for a large variety of quantum phases, such as spin liquids, unconventional superconductivity and topological phases of matter. At specific lattice filling the electronic bands have a semimetallic structure with a vanishing density of states, hosting Dirac, massless quasiparticles. This paradigm is well known in other materials, among which graphene stands first. When specific effects are taken into account, however, a gap is opened at the Dirac points and the quasiparticles become massive: a semimetal-insulator phase transition occurs. Such perturbations in graphene have been widely studied from different perspectives. Instead, the plethora of gap-opening terms in kagome lacks an established classification, and, in most cases, a clear physical interpretation. Recent work however indicates candidate kagome materials as strongly interacting compared to graphene. This suggests that mass terms are more likely to spontaneously originate, motivating interest in this research.

In this work we map the sixteen gap-opening terms of kagome materials into physical effects, leveraging information on the relative broken and preserved symmetries. The general features of kagome instabilities are then discussed with reference to graphene ones, picturing a complex and multifaced relation. The anomalous Hall effect and the spin-Hall effect, originally proposed for the honeycomb lattice, find a prominent host in kagome structures: contrarily to graphene, they are already relevant for nearest-neighbour hoppings, which generally represent the leading contribution. Remarkably, lattice deformation instabilities reflect one property of the model, namely that kagome lattice at 1/3 filling (Dirac points) can be mapped into a dimer model on the hexagonal lattice. Consistently, gap-opening distortions of lattice sites in one structure find a related bond-distortion in the other structure, and viceversa. The staggered, on-site potential which makes graphene an insulator has a dimerization pattern of alternating bonds as the corresponding mass in kagome, and similar mappings are found in more sophisticated distortions as Kekulé patterns. Lastly, honeycomb materials are known to have antiferromagnetic instability which leads to a trivial, insulating phase; instead, kagome materials suffer from magnetic frustration. At 1/3 filling however, orderings are possible thanks to the empty sites. Antiferromagnetic phases at the Dirac points are therefore gapped in both materials, with one difference: graphene AFM has a simple magnetic cell, while kagome AFM can be realised with enlarged magnetic cell. In conclusion, the established ground of graphene works as one additional benchmark, giving indications about the relevant instabilities of the two structures.

Contents

Chapter 1

Introduction

In crystalline materials, the component ions are arranged in regular patterns. Such periodical structures are remarkable for their symmetric aspect and for how these symmetries can be incorporated into the theoretical description. Among these structures, some allow the formation of single-layer crystals, which live in two dimensions. The first 2D material observed in nature was graphene (carbon), isolated in 2004 by Novoselov and Geim [12]. Both theoretical and experimental research on such material has seen tremendous success, with a consequent effort in developing and studying other 2D structures: more than a thousand monolayer materials have been predicted. The focus of this work is on two 2D crystal arrangements, honeycomb lattice and kagome lattice. In this venture, we will shed light on the interesting relationship between materials with these two structures, discussing the similarities and differences.

1.1 Insulators, metals and semimetals

Much of the properties of solid materials are encoded in the behaviour of the valence and conduction electrons. While core electrons are strongly bounded to the nuclei, the former are generally displaced among different crystal sites, and possibly free to move. Electronic band theory studies the energy levels which can, or cannot be accessed by valence electrons. It is necessarily rooted in the quantum-mechanical framework when low-energy regimes are considered and Pauli's exclusion principle plays a crucial role. Its formulation relies on the periodicity of the crystal: quantum wavefunctions of free electrons in a periodic potential are periodic functions modulated by plane waves (Bloch's theorem):

$$\psi_{i,k}(x) = u_i(x)e^{ikx}$$

Therefore, momentum k is a good quantum number, provided that wavefunctions ψ enjoy the same periodicity of the crystal (described by the reciprocal lattice vector K): $\psi_{i,k} = \psi_{i,k+K}$ The momentum space can therefore be restricted to the Brillouin zone, and the Hamiltonian can be block-diagonalized, where each block H_k (named Bloch Hamiltonian) has a dimension equal to the number of the periodic function $u_i(x)$. Each i-th eigenvalue $\varepsilon_i(k)$ of the Bloch Hamiltonian changes continuously with k, and is called **electronic band**[2]. When the chemical potential sits within the energy range of one band, electrons can increase their energy for an arbitrarily small electric field. This is the case with metals. Instead, if the chemical potential lies in the gap between two bands, the material is an insulator: to excite electrons a finite amount of energy is required. A possible configuration lies in between: in semimetals, two bands touch at a finite number of points where the density of states is vanishing, as shown in Figure 1.1 This is the case of graphene

and kagome materials when electrons are considered non-interacting and the chemical potential is specifically tuned. In particular such materials host bands that touch at points where they can be approximated as two corner-sharing cones. The linearized Hamiltonian around these points (named Dirac points) is the Dirac equation of Weyl quasiparticles (massless, chiral fermions)[1, 3, 6, 7, 9]. Such excitations behave as relativistic, massless fermions with the Fermi velocity v_F taking the role of the speed of light c [1] . Despite the strong difference in energy scale, the physics of these quasiparticles has intrinsic relativistic properties. An interesting example is given by the Klein paradox[1], which explains the surprisingly strong tunnelling through a potential barrier for relativistic fermions. In graphene and kagome such phenomenon prevents backscattering of the massless fermions emerging at the Dirac points [15, 16].
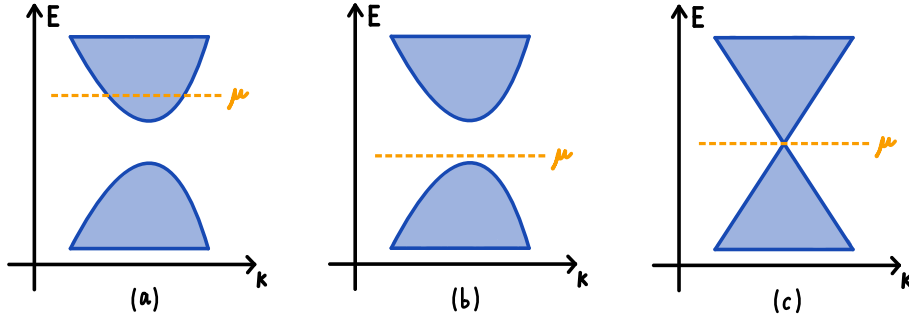

Figure 1.1: **(a)**Metallic, **(b)** insulating and **(c)** semimetallic band structures. The orange line indicates the chemical potential

1.2   Motivations and study overview

Kagome metals received profound attention in recent years, becoming some of the most prominent condensed-matter structures. They have been proposed as hosts for quantum spin liquids [19, 20], unconventional superconductivity[21], topological phases of matters[57], showing a wide spectrum of exotic quantum phases[59]. One reason for such variety and richness lies in the non-trivial geometry, which is responsible for an intriguing band structure. The presence of one flat band in momentum space (corresponding to charge localisation in real space) makes kagome metals an interesting setup for phenomena of strongly correlated electrons [22]. Although its conduction behaviour is generally metallic, at specific filling the bands show semimetallic structure with a vanishing density of state [11, 23], hosting Dirac, massless quasiparticles. Another important aspect deriving from its geometry is the presence of magnetic frustration. Structurally made of triangles, kagome is a perfect example of lattice geometry which strongly hinders antiferromagnetic order, as sketched in Figure 1.2. Remarkably, magnetic phases with fascinating features emerge from frustration [19].

In the present work, we focus on the semimetallic limit, where an effective Dirac theory emerges: specifically tuning the chemical potential, kagome materials become semimetals, and the effective Hamiltonian describes massless Dirac fermions. This paradigm is well known in other materials [10,

---

[1]The presence of Weyl quasiparticles is at the origin of the incorrect nomenclature used for graphene and kagome semimetals, which are often named as Weyl semimetals. However, as we discuss in the next section, certain perturbations open a gap at the Dirac points, and chirality is no more a good quantum number. In Weyl semimetals instead, perturbations can uniquely change the position of the Weyl nodes in the Brillouin zone, but not directly open a gap. In this case, the only way to annihilate Weyl nodes is to bring together a couple with opposite chirality[18, 42].
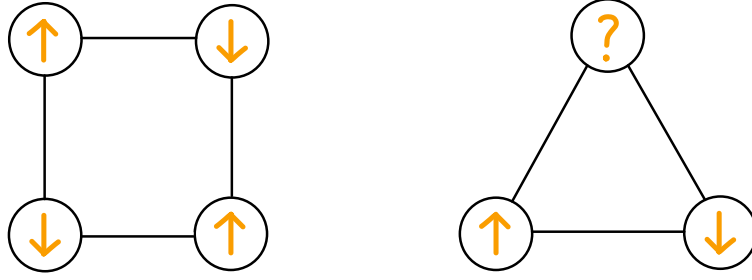
Figure 1.2: Antiferromagnetic ordering on the square lattice, and magnetic frustration on the triangular lattice. The energy of this last is degenerate with respect to the spin direction in the upper corner.

11], among which graphene stands first. Experimentally realised in 2004 [12], graphene has seen tremendous success, both theoretically and experimentally. Its popularity is rooted in its astonishing mechanical and transport properties. Extreme flexibility, low weight and remarkable strength are among its main characteristics[15]. A σ bond of the sp^2 hybridization is created between carbon atoms, making the structure particularly robust and creating the trigonal planar configuration. An additional p orbital, perpendicular to the plane, participates in a π bond, which is only half-filled. The two electrons involved in these bonds (the main actors in this thesis work) are responsible for graphene conduction properties. When considered non-interacting, these two electrons behave as Dirac quasiparticles, with linear dispersion relations at the Dirac points. Backscattering is prevented in this approximation, resulting in good transmission of heat and electric charges. However, specific effects are responsible for semimetal-insulator phase transition: if taken into account a gap is opened at the Dirac points, and the quasiparticles become massive (for this reason, these terms are named "mass terms"). This transition is usually associated with time-reversal or chiral symmetry breaking. The gap-opening perturbations in graphene have been partially classified in terms of symmetries [33], and widely studied from different perspectives [34–41, 46–48]. One viewpoint is the research line on topological phases of matters. Under particular interactions graphene shows quantum (spin) Hall effects [36], and conducting features of a topological insulator [57], a phase marked by gapped bulk and metallic states on the surface. One second, popular track concerns deformations of the lattice. Motivated by engineering applications such as carbon nanotubes[17, 38], lattice distortions, bending, straining, or twisting have been widely explored [39, 40, 42–44].

A semimetal-insulator phase transition is possible in kagome materials too, with equal mechanism at the fundamental level. Compared to graphene, however, the plethora of gap-opening terms in kagome lacks an established classification, and, in most cases, a clear physical interpretation. Filling this gap is motivated by two main reasons. Mazin et al. [23] showed that Sc-Herbertsmithite (kagome lattice) is strongly interacting compared to graphene, with a three times larger fine-structure constant[2]. Two possible conclusions appear to be in contrast. On one side, this fact indicates kagome materials as candidates for investigating phenomena of strongly correlated Dirac fermions. On the other side, it suggests that gap-opening effects are more likely

---

[2]The fine structure constant quantifies the strength of the Coulomb interaction, in the vacuum as in a medium. In the latter case, it is defined as the quantity

$$\alpha = \frac{e^2}{4\pi\epsilon_0\epsilon_r} \frac{1}{\hbar v_F}$$

where ϵ_r is the relative permittivity of the medium, e the elementary charge, v_F the Fermi velocity of the electrons.

to spontaneously originate, making the system an insulator. Identification and classification of these terms, and investigations about their spontaneous generation is one possible way to untie this knot. The second reason concerns the non-trivial relation between graphene and kagome materials. These two enjoy equal lattice symmetries, encoded in the p6m wallpaper group. They both host massless quasiparticles at the Dirac cones, which existence is protected by time reversal and chiral symmetries. In principle, one would expect a similar correspondence between the two families of gap-opening terms. Surprisingly, however, many differences are present: kagome is made of three sublattices instead of two, with strong consequences on the relevant instabilities that might arise. A canonical example is the emergence of magnetic configuration: while graphene is a perfect host for antiferromagnetic structure (which makes the system an insulator), kagome materials suffer from frustration, which discourages ordering. One underlying narrative of this thesis is to shed light on these analogies and disparities.

Our work is structured as follows. In the remaining part of this chapter, we introduce the tight-binding model, which describes non-interacting electrons hopping on the honeycomb and kagome lattice. We show the underlying mechanism leading to the semimetal-insulator phase transition, shared by all the gap-opening terms. In the second chapter, we define the theoretical framework to represent symmetries in quantum mechanics (and in field theory), with specific attention to graphene and kagome materials. We implement operators for reflection and rotation symmetries of these two lattices, along with symmetry operators of the respective free-electrons quantum theory. We leverage these tools as classifiers for the gap-opening terms, with reference to the broken or preserved symmetries. In the following chapter, we identify each mass term with a physical effect, for both considered lattices. Lacking an accurate overview in this framework, Chapter 3 is an alternation of literature-reviewing sections - predominant for graphene - and contributions of the present author, more consistent instead for kagome materials. Finally, we qualitatively discuss the spontaneous emergence of a few of these terms.

The main goals of this thesis can therefore be resumed as follows: *(i)* the identification of bilinear terms leading to a gap opening, i.e. a quantum transition between a semimetallic and an insulating phase; *(ii)* classification of mass terms according to symmetry arguments *(iii)* mapping of such instabilities into physical phenomena, both for graphene and kagome materials; *(iv)* discussion of fundamental analogies and differences between these two families. This investigation is a crucial step to address the relevance of such contributions and to establish whether they spontaneously arise from Coulomb interaction.

1.3 Tight-binding model of graphene

The tight-binding (TB) Hamiltonian describes the hoppings of free electrons. For the spinless case, it can be written in second quantization as

$$H = -t \sum_{\langle i,j \rangle} \psi_i^\dagger \psi_j \tag{1.1}$$

The summation is taken between nearest-neighbouring sites, and the parameter t represents the matrix element between two neighbouring orbitals:

$$-t = t_{ij} = \int dx\, \phi_j^*(x) U(x) \phi_i(x) \tag{1.2}$$

where $U(x)$ is the periodic potential. This quantity, also named *hopping amplitude*, takes the value $t \approx 2.8\text{eV}$ in graphene[15]. The sign of t is generally determined by the potential $U(x)$, according to

Eq.1.2: attractive potentials typically result in a negative sign of the integral. The energy spectrum depends linearly on t: a sign flip, therefore, relates particles with holes. If the Hamiltonian enjoys particle-hole symmetries, its spectrum is unchanged by the transformation $t \to -t$. [3]

(a)   (b)
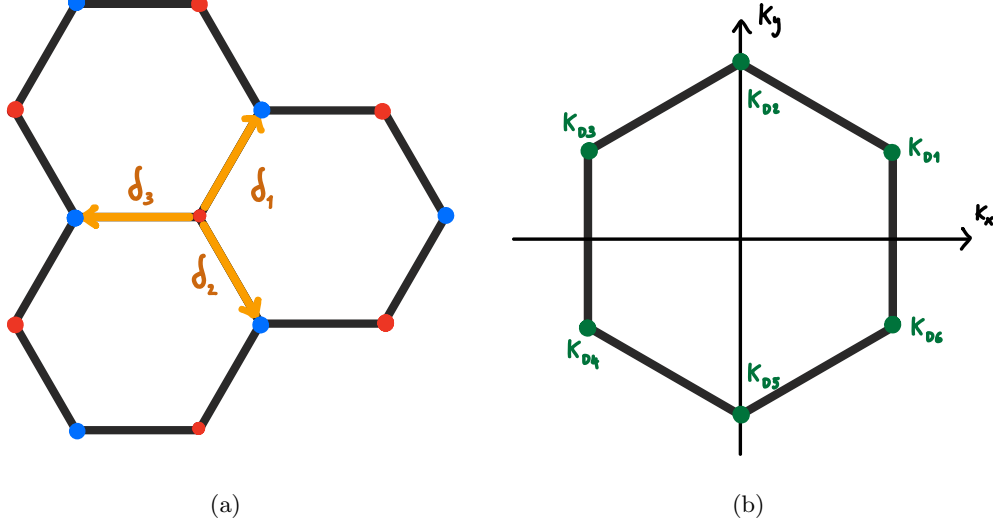
Figure 1.3: **(a)** Honeycomb lattice and **(b)** it's Brullouin zone. Sublattice vectors δ_i and Dirac points are drawn in orange and green respectively.

The kagome lattice of graphene is made of two intersecting Bravais lattices, which we label as A and B (see Figure 1.3a). The lattice vectors, connecting sites on the same sublattice, are given by

$$\alpha_1 = \frac{\ell}{2}\left(3, \sqrt{3}\right) \qquad \alpha_2 = \frac{\ell}{2}\left(3, -\sqrt{3}\right) \qquad \alpha_3 = \alpha_1 - \alpha_2 = \ell\left(0, \sqrt{3}\right) \tag{1.3}$$

We study electrons hopping on this structure, described by fermionic field operators a_i or b_i, depending on the considered sublattice. The TB Hamiltonian takes the following form [14]

$$H = -t \sum_{x_i \in A} \left(a_i^\dagger b_{i+\delta_1} + a_i^\dagger b_{i+\delta_2} + a_i^\dagger b_{i+\delta_3}\right) + h.c. \tag{1.4}$$

where the sublattice vectors are

$$\delta_1 = \frac{\ell}{2}\left(1, \sqrt{3}\right) \qquad \delta_2 = \frac{\ell}{2}\left(1, -\sqrt{3}\right) \qquad \delta_3 = \ell\left(-1, 0\right) \tag{1.5}$$

and ℓ is the lattice spacing. We exploit translational symmetry by Fourier transformation of the field operators:

$$a_i = \frac{1}{\sqrt{N/2}} \sum_{k \in \mathcal{B}} e^{ikx_i} a_k \tag{1.6}$$

---

[3]In the continuum the sign of kinetic energy is constrained by stronger reasons: the kinetic operator $\frac{p^2}{2m}$ has positive spectrum, it is bounded from below but not from above, therefore is sign cannot be inverted. Any discrete version of the Laplacian is instead bounded from below and above, removing such constrain.

The sum runs over the Brillouin zone, which is depicted in Figure 1.3b, and N is the number of lattice sites. The reciprocal of the kagome lattice is given by a honeycomb rotated of $\pi/2$.

$$\begin{aligned} H &= -\frac{t}{N/2} \sum_{x_i \in A} \sum_{k,k'} e^{ix_i(k-k')} \left(a_k^\dagger b_{k'} e^{ik'\delta_1} + a_k^\dagger b_{k'} e^{ik'\delta_2} + a_k^\dagger b_{k'} e^{ik'\delta_3} \right) + h.c. \\ &= -t \sum_k \sum_j a_k^\dagger b_k e^{ik\delta_j} + h.c. \end{aligned} \tag{1.7}$$

where we used that $\sum_{x_i \in A} e^{ix_i(k-k')} = \frac{N}{2}\delta_{k,k'}$. Defining the field operator $\Psi_k = (a_k, b_k)^T$ This expression can be written in matrix notation as

$$H = -t \sum_{k \in BZ} \Psi_k^\dagger \begin{pmatrix} 0 & \sum_j e^{ik\delta_j} \\ \sum_j e^{-ik\delta_j} & 0 \end{pmatrix} \Psi_k \tag{1.8}$$

Two electronic bands are encoded in the two eigenvalues of the Bloch Hamiltonian:

$$\epsilon_\pm(k) = \pm t \sqrt{3 + 2\cos\left(\sqrt{3}\ell k_y\right) + 4\cos\left(\frac{\sqrt{3}\ell}{2}k_y\right)\cos\left(\frac{3\ell}{2}k_x\right)} \tag{1.9}$$

The two energy bands are symmetric with respect to $\epsilon = 0$, which is a feature of the sublattice (chiral) symmetry $A \leftrightarrow B$, and charge (particle-hole) symmetry. In addition, the two bands touch each other at single points of the Brouillon zone, named Dirac points. We count six in total, of which only two belong to the reciprocal unit cell since the others are part of neighbouring cells. These two points, taken from different sublattices, are independent and are usually named *valleys*. A possible choice is

$$K_{D1} = \left(\frac{2\pi}{3\ell}, \frac{2\pi}{3\sqrt{3}\ell}\right) \qquad K_{D2} = \left(\frac{2\pi}{3\ell}, -\frac{2\pi}{3\sqrt{3}\ell}\right) \tag{1.10}$$
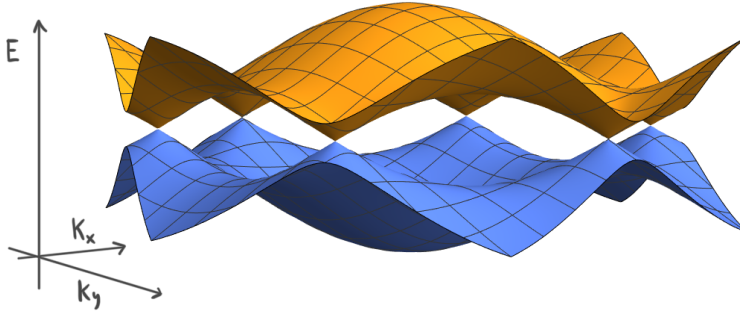
Figure 1.4:
Electronic bands of graphene in the Brillouin zone

1.3.1 Low energy expansion

This model has in fact semimetallic band structure, with a vanishing density of state at the band junction. A low energy expansion around these nodes ($E \approx 0$) reveals the Dirac nature of this semimetal: in the vicinity of Dirac points electrons behave as massless particles propagating at the

Fermi velocity $v_F = -\frac{3}{2}\ell t$. The Bloch Hamiltonian for $K_{D1} + q$ takes indeed the form of a Dirac Hamiltonian:

$$h(K_{D1} + k) = -\frac{3}{2}\ell t \begin{pmatrix} 0 & k_x + ik_y \\ k_x - ik_y & 0 \end{pmatrix} = v_F \left(k_x \tau_1 - k_y \tau_2 \right) \tag{1.11}$$

$$h(K_{D2} + k) = -\frac{3}{2}\ell t \begin{pmatrix} 0 & k_x - ik_y \\ k_x + ik_y & 0 \end{pmatrix} = v_F \left(k_x \tau_1 + k_y \tau_2 \right) \tag{1.12}$$

where τ_i are the Pauli matrices. It's worth noticing that the Fermi velocity depends on the considered material. We can include the degree of freedom encoded in the valleys by rewriting the Hamiltonian as

$$\mathcal{H}(k) = v_F \left(k_x \, \sigma_0 \otimes \tau_1 + k_y \, \sigma_3 \otimes \tau_2 \right) \tag{1.13}$$

where σ_i are the Pauli matrices acting on the valley subspace. Until now, we considered a spinless system. For a general spinful system the Hamiltonian becomes

$$\mathcal{H}(k) = v_F \left(k_x \, s_0 \otimes \sigma_0 \otimes \tau_1 + k_y \, s_0 \otimes \sigma_3 \otimes \tau_2 \right) \tag{1.14}$$

Here, τ_i, σ_i, and s_i are the Pauli matrices acting on the sublattice, valley and spin subspace respectively. The full field operator in this space is given by

$$\Psi_q = \begin{pmatrix} a_{q\uparrow+} & b_{q\uparrow+} & a_{q\uparrow-} & b_{q\uparrow-} & a_{q\downarrow+} & b_{q\downarrow+} & a_{q\downarrow-} & b_{q\downarrow-} \end{pmatrix}^T \tag{1.15}$$

1.4   Tight-binding model on the kagome lattice

Figure 1.5: **(a)** Kagome lattice and **(b)** it's Brullouin zone. Sublattice vectors δ_{ij} and Dirac points are drawn in orange and green respectively.

The tight-binding model Hamiltonian for spinful particles reads

$$H = -t \sum_{\langle i,j \rangle, s} \psi_{is}^\dagger \psi_{js} \tag{1.16}$$

where the summation is taken between near-neighbors $\langle i, j \rangle$, and over the spin index s. The kagome lattice has three sub-lattices A, B, C. The respective field operators are

$$\Psi_{is} = (a_{is}, b_{is}, c_{is})^T \tag{1.17}$$

and the three sublattice vectors are shown in figure 1.5a:

$$\delta_{ab} = \ell(1, 0)^T \qquad \delta_{bc} = \frac{\ell}{2}(1, \sqrt{3})^T \qquad \delta_{cd} = \frac{\ell}{2}(-1, \sqrt{3})^T \tag{1.18}$$

We follow the procedure of the previous section to block-diagonalize the TB Hamiltonian in momentum space. After Fourier transformation indeed, the Hamiltonian reads[25]

$$H = -\frac{t}{N/3} \sum_s \sum_{x_i \in A} \sum_{k,k'} e^{ix_i(k-k')} \left[a_{ks}^\dagger b_{k's} \left(e^{ik'\delta_{ab}} + e^{-ik'\delta_{ab}} \right) + \right.$$

$$\left. + a_{ks}^\dagger c_{k's} \left(e^{ik'\delta_{ac}} + e^{-ik'\delta_{ac}} \right) + b_{ks}^\dagger c_{k's} \left(e^{ik'\delta_{bc}} + e^{-ik'\delta_c} \right) \right] + h.c. \tag{1.19}$$

$$= -2t \sum_s \sum_k \cos\left(k \cdot \delta_{ab}\right) a_{ks}^\dagger b_{ks} + \cos\left(k \cdot \delta_{ac}\right) a_{ks}^\dagger c_{ks} + \cos\left(k \cdot \delta_{bc}\right) b_{ks}^\dagger c_{ks} + h.c.$$

Again, the Hamiltonian can be written in the matrix form as

$$H = \sum_s \sum_{k \in \mathcal{B}} \Psi_s^\dagger(k) h(k) \Psi_s(k) \tag{1.20}$$

The Bloch Hamiltonian is

$$h(k) = -2t \begin{pmatrix} 0 & \cos\left(k \cdot \delta_{ab}\right) & \cos\left(k \cdot \delta_{ac}\right) \\ \cos\left(k \cdot \delta_{ab}\right) & 0 & \cos\left(k \cdot \delta_{bc}\right) \\ \cos\left(k \cdot \delta_{ac}\right) & \cos\left(k \cdot \delta_{bc}\right) & 0 \end{pmatrix} \tag{1.21}$$

and where $\Psi_s(k) = \left(a_s(k), b_s(k), c_s(k) \right)^T$ are the annihilation operators in momentum space, and the summation in $k = (k_x, k_y)^T$ runs over the first Brillouin zone, represented in Figure 1.5b. This Hamiltonian has three bands:

$$E(k) = \begin{cases} -t\left(1 \pm \sqrt{3 + 2\sum_i \cos\left(2k \cdot \delta_i\right)}\right) \\ 2t \end{cases} \tag{1.22}$$

The two lower bands have a structure similar to graphene, with six Dirac points. One additional flat band sits on top at energy $2t$. Dirac points belong to the reciprocal lattice, which has a honeycomb structure, made of two sublattices. Three of the six Dirac points belong to one sublattice, and three to the other. However, among the six, only two (one from each sub-lattice) belong to the unit cell, because of the periodicity of the crystal. These two points take the name of **valleys**. The low energy expansion (see next paragraph) is mildly affected by the choice of the two points, in the following sense: the theories which emerge in linear approximation at the different Dirac points are equivalent, up to a gauge transformation. Such a relation ensures equivalent spectrum properties. However, transformations of the Hamiltonian that mix these 6 points require extra care. This will be investigated in more depth in section 2.2.1.
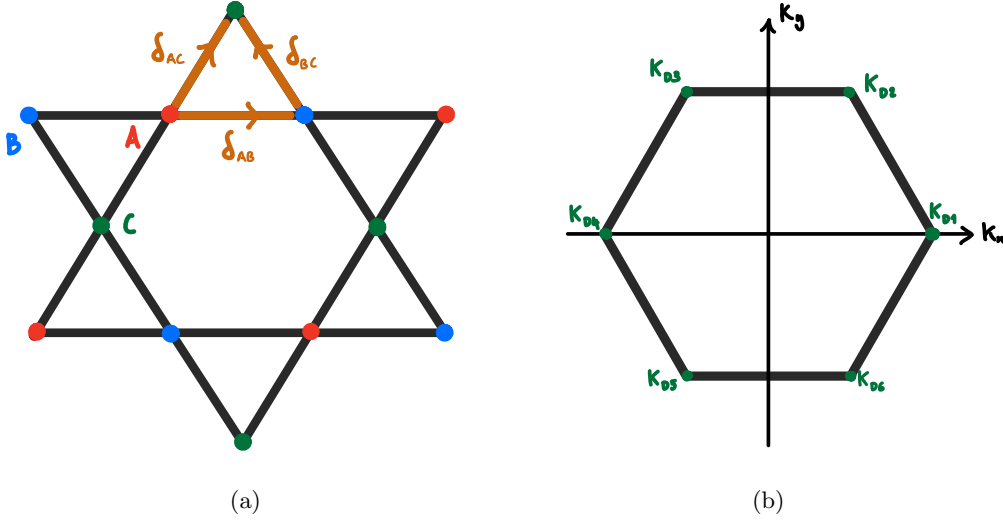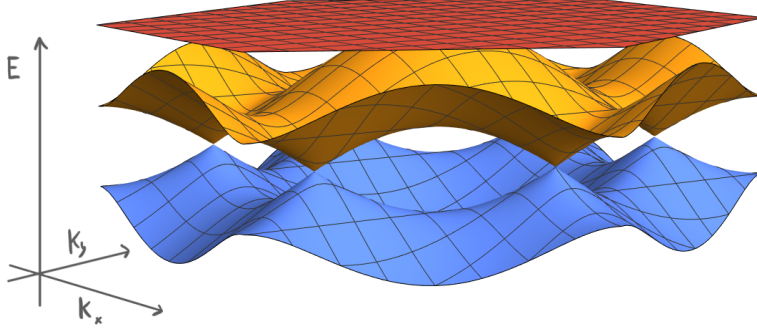
Figure 1.6:
Electronic bands of graphene in the Brillouin zone

1.4.1 Low energy expansion

We expand $h(k)$ up to linear terms, at the Dirac points K_{D1} and K_{D4}:

$$K_{D1} = \left(\frac{2\pi}{3\ell}, 0 \right)^T \qquad K_{D4} = \left(-\frac{2\pi}{3\ell}, 0 \right)^T \qquad (1.23)$$

The matrix elements can be approximated as

$$\cos\left[(K_{D1} + k) \cdot \delta_{ab}\right] \simeq -\frac{1}{2} - \frac{\sqrt{3}}{2}\ell k_x \qquad\qquad \cos\left[(K_{D4} + k) \cdot \delta_{ab}\right] \simeq -\frac{1}{2} + \frac{\sqrt{3}}{2}\ell k_x \quad (1.24)$$

$$\cos\left[(K_{D1} + k) \cdot \delta_{ac}\right] \simeq \frac{1}{2} - \frac{\sqrt{3}}{4}\ell k_x - \frac{3}{4}\ell k_y \quad \cos\left[(K_{D4} + k) \cdot \delta_{ac}\right] \simeq \frac{1}{2} + \frac{\sqrt{3}}{4}\ell k_x + \frac{3}{4}\ell k_y \quad (1.25)$$

$$\cos\left[(K_{D1} + k) \cdot \delta_{bc}\right] \simeq \frac{1}{2} - \frac{\sqrt{3}}{4}\ell k_x + \frac{3}{4}\ell k_y \quad \cos\left[(K_{D4} + k) \cdot \delta_{bc}\right] \simeq \frac{1}{2} + \frac{\sqrt{3}}{4}\ell k_x - \frac{3}{4}\ell k_y \quad (1.26)$$

The linearized Bloch Hamiltonian therefore reads

$$h(K_{D1} + k) = -t \begin{pmatrix} 0 & 1 + \sqrt{3}\ell k_x & -1 + \frac{\sqrt{3}}{2}\ell k_x + \frac{3}{2}\ell k_y \\ 1 + \sqrt{3}\ell k_x & 0 & -1 + \frac{\sqrt{3}}{2}\ell k_x - \frac{3}{2}\ell k_y \\ -1 + \frac{\sqrt{3}}{2}\ell k_x + \frac{3}{2}\ell k_y & -1 + \frac{\sqrt{3}}{2}\ell k_x - \frac{3}{2}\ell k_y & 0 \end{pmatrix} \qquad (1.27)$$

$$h(K_{D4} + k) = h(K_{D1} - k)$$

1.4.2 Flat band decoupling

We transform the linearized Hamiltonian in order to decouple the flat band from the other two, at the Dirac point. To do that, we consider the matrix U that diagonalises $h(K_{D1}) = h(K_{D4})$ Eq.1.27, meaning that it decouples the three bands at the Dirac point. In principle, one could find a k-dependent transformation U_k, to diagonalise the Bloch Hamiltonian at each point in the
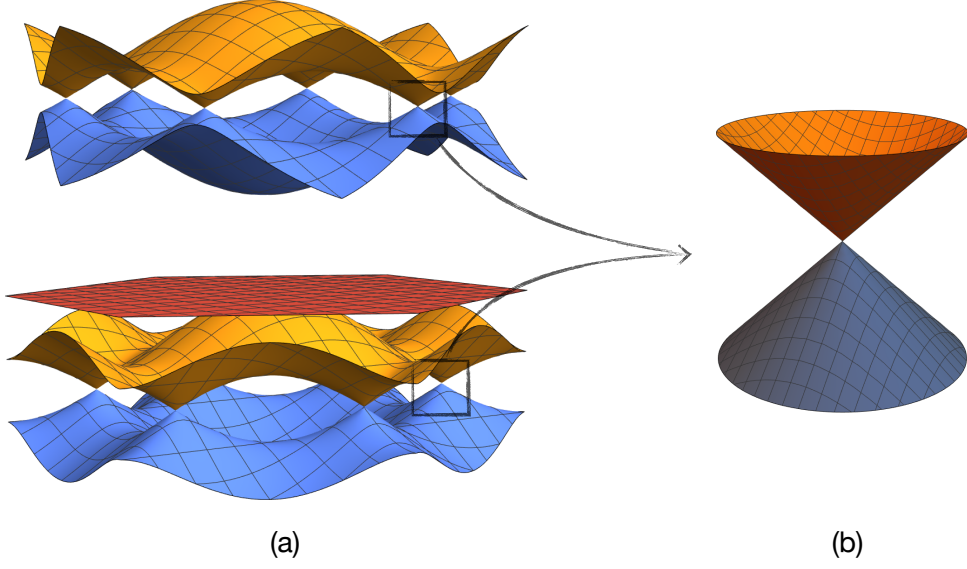
Figure 1.7: **(a)** Electronic bands of graphene (top) and kagome (bottom) tight-binding model and **(b)** their linear approximation at the Dirac points.

Brillouin zone. The two lower bands touch at the Dirac points: consistently, $h(K_{Di})$ is doubly degenerated. The choice of basis vectors in this subspace is arbitrary.

$$U = \left[\frac{1}{\sqrt{2}} \begin{pmatrix} 0 \\ 1 \\ 1 \end{pmatrix}, \quad \frac{1}{\sqrt{6}} \begin{pmatrix} 2 \\ -1 \\ 1 \end{pmatrix}, \quad \frac{1}{\sqrt{3}} \begin{pmatrix} -1 \\ -1 \\ 1 \end{pmatrix} \right] = \left[\tilde{A}, \tilde{B}, \tilde{C} \right] \tag{1.28}$$

Another transformation becomes useful. We define two new momenta:

$$k_1 = \frac{1}{2}(k_x - \sqrt{3}k_y) \tag{1.29}$$

$$k_2 = \frac{1}{2}(\sqrt{3}k_x + k_y) \tag{1.30}$$

The transformed linearized Hamiltonian reads

$$\tilde{h}(K_{D1} + k) = U h(K_{D1} + k) U^{-1} = \begin{pmatrix} -t - v_f k_1 & -v_f k_2 & \frac{v_f}{\sqrt{2}} k_2 \\ -v_f k_2 & -t + v_f k_1 & \frac{v_f}{\sqrt{2}} k_1 \\ \frac{v_f}{\sqrt{2}} k_2 & \frac{v_f}{\sqrt{2}} k_1 & 2t \end{pmatrix} \tag{1.31}$$

$$\tilde{h}(K_{D4} + k) = \tilde{h}(K_{D1} - k) \tag{1.32}$$

where $v_f = \sqrt{3}\ell t$ can be seen as the effective Fermi velocity. The 2x2 block in the left-upper corner describes the two low-energy bands, while the other terms describe the coupling of these lasts with the flat band $E = 2t$. The flat band contributes to the low-energy theory with terms of order $\mathcal{O}(k^2)$

and can be therefore neglected. In the subspace of low-energy bands (2x2, left-upper block), the Hamiltonian reads

$$\tilde{\mathcal{H}}(k) = \tilde{h}(K_{D1} + k) = -t\mathbb{1} - v_f \left(k_1 \ \tau_3 + k_2 \ \tau_1\right) \tag{1.33}$$

where τ_i is the i-th Pauli matrix acting on the **sublattice subspace**. For the other valley K_{D4}, k enters with a minus sign. We absorb the term proportional to the identity into the chemical potential, i.e. we consider $1/3$ lattice filling. Including the valley degree of freedom, the Hamiltonian reads:

$$\tilde{\mathcal{H}}(k) = -v_f \left(k_1 \ \sigma_3 \otimes \tau_3 + k_2 \ \sigma_3 \otimes \tau_1\right) \tag{1.34}$$

where σ_i is the i-th Pauli matrix acting on the **valley subspace**. We can include the spin degree of freedom in our picture, using that $\tilde{H}(k)$ is spin-independent:

$$\tilde{\mathcal{H}}(k) = -v_f \left(k_1 \ s_0 \otimes \sigma_3 \otimes \tau_3 + k_2 \ s_0 \otimes \sigma_3 \otimes \tau_1\right) \tag{1.35}$$

where s_i is the i-th Pauli matrix acting on the **spin subspace**.

1.4.3 Hilbert space of the model

In the following sections, we are going to consider possible bilinear terms (or **mass** terms), asking whether they open a gap at the Dirac cones, and which symmetries they preserve or break. Since the most general mass term may involve spin or valley dependence, we will take bilinear operators acting on the following Hilbert space:

$$\mathbb{H}_3 \equiv \underbrace{\mathbb{C}^2}_{\text{Spin space}} \otimes \underbrace{\mathbb{C}^2}_{\text{Valleys sp.}} \otimes \underbrace{\mathbb{C}^3}_{\text{Sublattices sp.}} \tag{1.36}$$

In this thesis, we are interested in the vicinity of the Dirac points $E \approx -t$ (often referred to as **low energy** theory). We therefore project these operators in $\mathbb{H}_2$ subspace of $\mathbb{H}_3$, which describes the two low-energy bands:

$$\mathbb{H}_2 \equiv \underbrace{\mathbb{C}^2}_{\text{Spin space}} \otimes \underbrace{\mathbb{C}^2}_{\text{Valleys sp.}} \otimes \underbrace{\mathbb{C}^2}_{\text{Low-en. bands}} \tag{1.37}$$

1.5 2D Semimetal-insulator phase transition

We study bilinear terms that open a gap at the Dirac points, separating the two low-energy bands and making the system an insulator. We address the problem within the Dirac formalism, considering a two-dimensional Hilbert space. A generalisation to larger dimensional spaces (e.g. if one includes spin and valley) is straightforward. We start with the following Dirac Hamiltonian:

$$H = p_1\alpha_1 + p_2\alpha_2 + mM \tag{1.38}$$

where $p_{1,2}$ are the momenta operator in two directions, and $\alpha_{1,2}$ Pauli matrices (or, more generally, some D-dimensional matrices satisfying fermionic commutation relations $\{\alpha_i, \alpha_j\} = 2\delta_{ij}$). To find the conditions for m to be a mass scale and M to be a gap-opening matrix, we consider the square of the Hamiltonian:

$$H^2 = p_1^2 + p_2^2 + mp_1 \left\{\alpha_1, M\right\} + mp_2 \left\{\alpha_2, M\right\} + m^2 M^2 \tag{1.39}$$

If the mass terms satisfy the following relations

$$\{\alpha_i, M\} = 0 \qquad\qquad M^2 = 1 \qquad\qquad (1.40)$$

we obtain

$$H^2 = p_1^2 + p_1^2 + m^2 M^2 \qquad\qquad (1.41)$$

which yields the dispersion relation of Dirac particle with mass m:

$$\epsilon_{\mathbf{p}} = \pm\sqrt{\mathbf{p}^2 + m^2} \qquad\qquad (1.42)$$

From now on, we refer to terms satisfying Eq.1.40 as **gap terms**, because of the gap of amplitude $2\,|m|$ opening at the Dirac point. A graphical sketch of the gapless ($m = 0$) and gapped dispersion relation Eq.1.42 are reported in Figure 1.8.
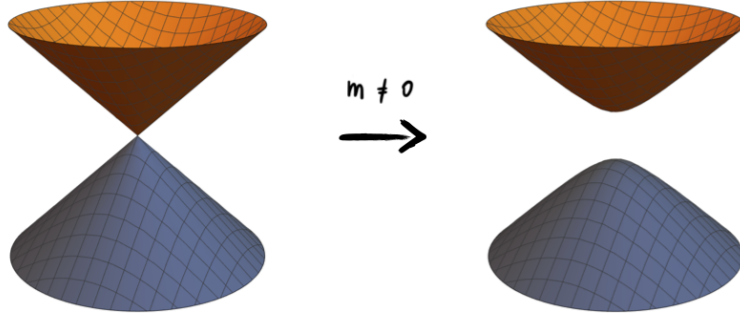
Figure 1.8: Semimetal-insulator phase transition: a gap opens at the Dirac points, and the fermionic quasiparticles acquire a finite mass.

1.5.1 Graphene

Low-energy approximation of the TB Hamiltonian in graphene is an operator which belongs to the following Hilbert space:

$$\mathbb{H}_2 \equiv \underbrace{\mathbb{C}^2}_{\text{Spin space}} \otimes \underbrace{\mathbb{C}^2}_{\text{Valleys sp.}} \otimes \underbrace{\mathbb{C}^2}_{\text{Sublattices sp.}} \qquad\qquad (1.43)$$

The general mass term in this theory is therefore an operator of the kind

$$\mathcal{M}_{ijk} = s_i \otimes \sigma_j \otimes \tau_k \qquad\qquad (1.44)$$

s_i, σ_i, τ_i are identity matrices ($i = 0$) and Pauli matrices ($i = 1, 2, 3$). Between the 64 operators forming a basis for $\mathbb{H}_2$, 16 anti-commute with the graphene Hamiltonian Eq. 1.14. The list can be found in Table 2.2, and it corresponds (up to a change of basis) to the list obtained in [33].

1.5.2 Kagome

Mass terms in the low-energy theory of kagome are operators acting on $\mathbb{H}_2$. We name them

$$\mathcal{M}_{ijk} = s_i \otimes \sigma_j \otimes \tau_k \tag{1.45}$$

where i, j, k run in $\{0, 1, 2, 3\}$. These operators do not involve couplings with the flat band. We embed the gap terms in the full space $\mathbb{H}_3$ in the following way:

$$\tilde{M}_{ijk} = s_i \otimes \sigma_j \otimes \begin{pmatrix} \tau_k & & 0 \\ & & 0 \\ 0 & 0 & 0 \end{pmatrix} \tag{1.46}$$

We have 64 possible mass terms, but only 16, reported in Tab.2.2, anti-commute with the Hamiltonian opening a gap. At the time of writing, such classification is not present in the literature on kagome metals.

Note that we are working in the decoupled representations, in which the Hamiltonian is diagonal at the Dirac points. The mass term in the original representation (same as Eq. 1.21) are obtained using

$$M_{ijk} = U^{-1} \tilde{M}_{ijk} U \tag{1.47}$$

Coupling with the flat band One may wonder if a gap can be opened by the coupling between the low-energy bands $|\psi_{1,2}\rangle$, and the flat band $|\psi_3\rangle$. We refer to operators acting on $\mathbb{H}_3$ (in the representation Eq.1.31):

$$\tilde{V} = \begin{pmatrix} 0 & 0 & a \\ 0 & 0 & b \\ a^* & b^* & c \end{pmatrix} \tag{1.48}$$

In perturbation theory, the first-order corrections to the low-energy bands vanish:

$$E_1^{(1)} = \langle \psi_1 | \tilde{V} | \psi_1 \rangle = 0 \tag{1.49}$$

$$E_1^{(2)} = \langle \psi_2 | \tilde{V} | \psi_2 \rangle = 0 \tag{1.50}$$

A finite contribution comes from second-order corrections

$$E_1^{(2)} = \frac{\left| \langle \psi_1 | \tilde{V} | \psi_3 \rangle \right|^2}{t - 2t} = -\frac{|a|^2}{t} \tag{1.51}$$

$$E_2^{(2)} = \frac{\left| \langle \psi_2 | \tilde{V} | \psi_3 \rangle \right|^2}{t - 2t} = -\frac{|b|^2}{t} \tag{1.52}$$

If $|a|^2 \neq |b|^2$ a gap opens. However, we notice that this gap is proportional to $\frac{1}{t}$, and therefore can be neglected.

1.5.3 On the choice of Dirac points

Note: *For conciseness we set the following discussion for one structure. We choose kagome lattice because it requires one additional passage, namely the flat band decoupling. An equivalent (and simpler) derivation can be obtained for the honeycomb lattice.*

In the previous section we considered the low-energy expansion of the TB hamiltonians, around two Dirac points of the kagome bands, K_{D1} and K_{D4}. This choice however is arbitrary, as far as the two points are taken from different sublattices (referring to Fig.1.5b, one point needs to have an even index, and the other odd index). For instance, the low-energy hamiltonians around K_{D1} and K_{D3} are said to be equivalent, because these two points are related by reciprocal lattice vectors. In this section we address this correspondence, and we discuss how it applies to the gap-opening terms. For the following discussion, we label the low-energy Hamiltonian H with two upper indices (ij), that indicate the two chosen Dirac points (according to Fig. 1.5b). For example, Hamiltonian Eq.1.35 is labeled as $H^{(14)}$. When only one index is present, we refer to the hamiltonian acting on one single valley.

As we anticipated in the previous section, expanding around different points results in different Hamiltonians, which however share the same spectral properties. This is not accidental. A gauge transformation[4] relates the different expansions. In particular, the 3x3 Hamiltonian expanded around K_{D1} is related to the one around the equivalent Dirac points via

$$H^{(1)} = \mathcal{G}_1 H^{(3)} \mathcal{G}_1^{-1} \qquad\qquad H^{(1)} = \mathcal{G}_2 H^{(5)} \mathcal{G}_2^{-1} \tag{1.54}$$

where

$$\mathcal{G}_1 = \mathrm{diag}\,(1, -1, 1) \qquad\qquad \mathcal{G}_2 = \mathrm{diag}\,(-1, 1, 1) \tag{1.55}$$

The 3x3 Hamiltonian expanded around K_{D4} is instead related with the other two equivalent points as

$$H^{(4)} = \mathcal{G}_2 H^{(2)} \mathcal{G}_2^{-1} \qquad\qquad H^{(4)} = \mathcal{G}_1 H^{(6)} \mathcal{G}_1^{-1} \tag{1.56}$$

We then characterised the equivalence of Dirac points with a **gauge symmetry**, which is reflected in equal spectral properties. We show one explicit example to clarify the discussion. The linearized hamiltonians at the Dirac point K_{D1} and K_{D3} are

$$
\begin{aligned}
h(K_{D1} + k) &\simeq \begin{pmatrix} 0 & -1 - \sqrt{3}k_x & 1 - \frac{\sqrt{3}}{2}\left(k_x + \sqrt{3}k_y\right) \\ -1 - \sqrt{3}k_x & 0 & 1 + \frac{\sqrt{3}}{2}\left(-k_x + \sqrt{3}k_y\right) \\ 1 - \frac{\sqrt{3}}{2}\left(k_x + 3k_y\right) & 1 + \frac{\sqrt{3}}{2}\left(-k_x + \sqrt{3}k_y\right) & 0 \end{pmatrix} \\
h(K_{D3} + k) &\simeq \begin{pmatrix} 0 & 1 + \sqrt{3}k_x & 1 - \frac{\sqrt{3}}{2}\left(k_x + \sqrt{3}k_y\right) \\ 1 + \sqrt{3}k_x & 0 & -1 - \frac{\sqrt{3}}{2}\left(-k_x + \sqrt{3}k_y\right) \\ 1 - \frac{\sqrt{3}}{2}\left(k_x + 3k_y\right) & -1 - \frac{\sqrt{3}}{2}\left(-k_x + \sqrt{3}k_y\right) & 0 \end{pmatrix}
\end{aligned}
\tag{1.57}
$$

The two are equal up to a transformation of the field operators

$$\begin{pmatrix} a_k \\ b_k \\ c_k \end{pmatrix} \qquad \rightarrow \qquad \begin{pmatrix} a_k \\ -b_k \\ c_k \end{pmatrix} \tag{1.58}$$

which corresponds indeed to the gauge transformation $\mathcal{G}_1$ defined in Equation 1.55.

---

[4]We name $\mathcal{G}$ a "gauge" transformation because it can be written as the following transformation on the second quantized fields:

$$\hat{c}_j' = e^{i\phi_j}\hat{c}_j \tag{1.53}$$

where $\hat{c}_j$ are the creation operators on the sublattices A, B, C. Note that this relation resembles the usual gauge transformation $\psi'(x) = e^{i\Lambda(x)}\psi(x)$.

We discuss now how this symmetry applies to the gap opening terms. We know that "equivalent" hamiltonians are related via one precise gauge transformation. This implies that the respective mass terms (i.e. the additional anti-commuting terms) are related by the same gauge transformation[5]. The implication of this finding is that each mass term corresponds to a family of gap-opening terms, which are gauge related. Even more: all these related mass terms enjoys or breaks the same symmetries. In our future discussion, we can therefore drop the indices ij, and refer to a generic mass term M_{abc}, being aware it corresponds to a family of gauge-related operators in the original representation.

This discussion needs extra-care in kagome materials, because the additional passage of decoupling the flat-band is required. For each $H^{(ij)}$ indeed one can find a unitary transformation that *(1)* decouples the flat band and *(2)* transforms the Hamiltonian into $H^{(14)}$ Eq.1.35. This last point is allowed by the degenerate nature of the low-energy subspace. At the Dirac point indeed there is a two-dimensional subspace associated with the same eigenvalue, and one is able to choose the basis of eigenvectors which gives that precise form of the Hamiltonian $\tilde{H}$. For each $H^{(ij)}$, we define $U_{(ij)}$ as this precise unitary operator, i.e. the operator such that

$$U_{(ij)}H^{(ij)}U_{(ij)}^{-1} = \tilde{H} \tag{1.59}$$

The form of the transformation $U_{(ij)}$ depends on the particular Dirac points ij, but again the gauge symmetry relates them[6].

---

[5]Mass terms of gauge-related hamiltonians are related by the same gauge transformation: if $H^{(i)} = \mathcal{G}H^{(j)}\mathcal{G}^{-1}$ and $\{H^{(j)}, M^{(j)}\} = 0$ then we can define $M^{(i)} = \mathcal{G}M^{(j)}\mathcal{G}^{-1}$, which anti-commutes with $H^{(i)}$:

$$\{H^{(i)}, M^{(i)}\} = \mathcal{G}\{H^{(j)}, M^{(j)}\}\mathcal{G}^{-1} = 0$$

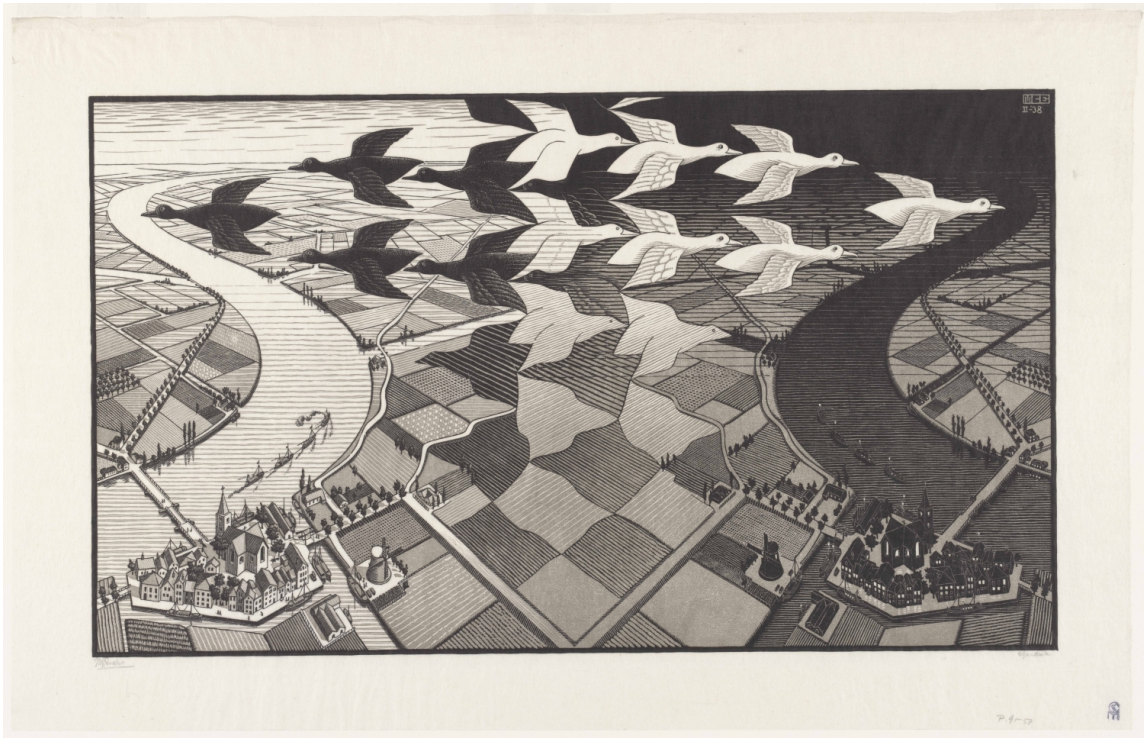[6]The relation between the operators $U_{(ij)}$ can be obtained as follows:

$$\begin{cases} H^{(ij)} = U_{(ij)}^{-1}\tilde{H}U_{(ij)} \\ H^{(ij)} = \mathcal{G}H^{(kl)}U_{ij} \end{cases} \implies H_{kl} = U_{kl}^{-1}\tilde{H}U_{kl} = \mathcal{G}^{-1}H_{ij}\mathcal{G} = \mathcal{G}^{-1}U_{ij}^{-1}\tilde{H}U_{ij}\mathcal{G} \tag{1.60}$$

Therefore

$$\boxed{U_{kl} = U_{ij}\mathcal{G}} \tag{1.61}$$

Chapter 2

Symmetries

2.1 Anti-unitary symmetries

Symmetries constitute a powerful tool in quantum mechanics. The formulation of a generic QM problem can be largely simplified when its symmetries are exploited, thanks to a dimensional reduction [26, 28]. In quantum mechanics, symmetries are represented by *unitary* or *anti-unitary* operators[1]. Symmetry transformations are indeed required to preserve probability densities. Quantities such as $|\langle\psi|\phi\rangle|^2$ must be invariant under a symmetry transformations $|\psi\rangle \to |U\psi\rangle$, and this is only possible if $\langle U\psi|U\phi\rangle = \langle\psi|\phi\rangle$ (U unitary operator) or instead $\langle U\psi|U\phi\rangle = \langle\psi|\phi\rangle^* = \langle\phi|\psi\rangle$ (U anti-unitary operator).

When tackling a QM problem (i.e. finding eigenvalues and eigenstates of the Hamiltonian) the typical procedure is to find unitary operators U that commute with the Hamiltonian: $[U, H] = 0$. If U exists, there exists a basis of the Hilbert space in which H and U are simultaneously block-diagonal[2]. Each block is associated with an eigenvalue of U, and it is called an *irreducible representation* (irrep) of the symmetry. One can repeat this procedure for all the unitary operators U_i which commute with H, producing the finest block structure. One may wonder if something can be said about the structure of each block. Since unitary symmetries are already taken into account, a possible answer comes from the anti-unitary ones.
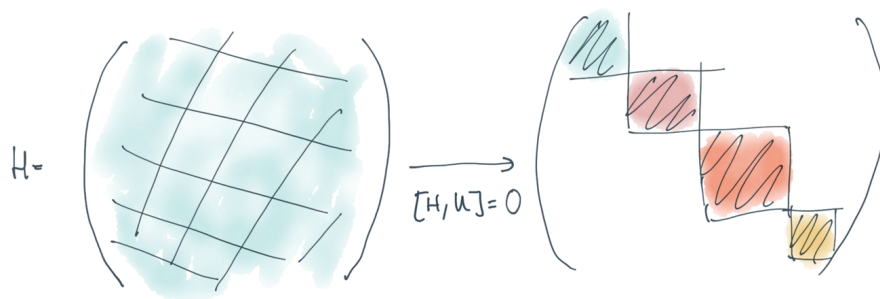
Figure 2.1: Block-diagonalization of the Hamiltonian into irreps of a symmetry operator. Image taken from [28].

In the next chapter, we define two anti-unitary symmetries, time-reversal $\mathcal{T}$ and charge (particle-hole) $\mathcal{C}$, that respectively commute and anti-commute with the Hamiltonian[28]. We sketch an argument to prove that these two are exhaustive [29]: $\mathcal{T}$ and $\mathcal{P}$ describe all the anti-unitary symmetries, up to multiplication by a unitary operator. Moreover, we describe one last symmetry (chirality), which is unitary, but it anti-commutes with the Hamiltonian (instead of commuting). In conclusion, we apply this formalism to the relevant examples: the tight-binding model on graphene and the kagome lattice.

---

[1]An operator U is said to be **unitary** if

- it is linear
- $U^\dagger = U^{-1}$, or alternatively $\langle U\psi|U\phi\rangle = \langle\psi|\phi\rangle$.

An operator U is said to be **anti-unitary** if

- it is anti-linear (i.e. $U\alpha|\psi\rangle = \alpha^* U|\psi\rangle$)
- $\langle U\psi|U\phi\rangle = \langle\psi|\phi\rangle^*$.

[2]More precisely, U is diagonal and H is block-diagonal

2.1.1 Time reversal

Time reversal operator $\mathcal{T}$ is the transformation which inverts the time axis direction. It is anti-unitary since

$$\mathcal{T}x\mathcal{T}^{-1} = x \qquad \mathcal{T}p\mathcal{T}^{-1} = -p \tag{2.1}$$

and therefore

$$\mathcal{T}i\mathcal{T}^{-1} = \hbar\mathcal{T}\left[x,p\right]\mathcal{T}^{-1} = -\hbar\left[x,p\right] = -i$$

It can therefore be written as

$$\mathcal{T} = U_T \cdot \mathcal{K} \tag{2.2}$$

where $\mathcal{K}$ is the complex conjugation operator[3], and U_T is unitary[4]. It can be seen from Eqs.2.1 that $\mathcal{T}$ flips the direction of the angular momentum. In the same way, also the spin (that can be seen as a magnetic momentum) is flipped:

$$\mathcal{T}s\mathcal{T}^{-1} = -s \tag{2.3}$$

The Hamiltonian is said to be $\mathcal{T}$-invariant if

$$\mathcal{T}H\mathcal{T}^{-1} = H \qquad \rightarrow \qquad U_T H^* U_T^{-1} = H \tag{2.4}$$

i.e. if $\mathcal{T}$ commutes with H. Using that time-reversal flips the momentum and commutes with the hamiltonian, we obtain this last relation in momentum space:

$$\boxed{U_T h_k^* U_T^{-1} = h_{-k}}$$

The square of the time reversal operator $\mathcal{T}^2 = U_T \mathcal{K} U_T \mathcal{K} = U_T U_T^*$ has two possible eigenvalues[5]:

$$\lambda_{\mathcal{T}^2} = \begin{cases} +1 & \text{spinless / integer spin} \\ -1 & \text{half integer spin} \end{cases} \tag{2.6}$$

Example: spin 1/2   We are interested now to write explicitly the form of U_T in the case of a spin 1/2 particle[6]. One can immediately see that the complex conjugation flips the y component of the spin σ_y, and leaves untouched the others. U_T therefore must commute with σ_y, and anti-commute with σ_x, σ_z. A solution is given by

$$U_T = -i\sigma_y \tag{2.7}$$

---

[3]The action of the complex conjugation on the operators is as follows:

$$\mathcal{K}U\mathcal{K}^{-1} = U^*$$

[4]It can be proven that any anti-unitary operator can be written as a composition of a unitary operator and complex conjugation.

[5]The reason is that $U = U_T U_T^*$ is a unitary (then linear) map from the irrep (the Hilbert subspace represented by the Hamiltonian sub-block) to itself. Therefore by Schur's Lemma, it must be a multiple of the identity $U = U_T U_T^* = e^{i\phi}\mathbb{1}$. Then

$$U_T^* U_T U_T^* = U_T^* e^{i\phi} = e^{-i\phi} U_T^* \tag{2.5}$$

which only solution is $e^{i\phi} = \pm 1$

[6]We consider uniquely the spin degree of freedom. The Hilbert space of the system is therefore given by $\mathbb{H} = \mathbb{C}^2$.

where one can explicitly see that $\mathcal{T}^2 = -1$. A general solution for any spin s is given by a rotation of π around the y axis:

$$U_T = \exp\left(-i\pi s_y\right) \tag{2.8}$$

Kramer's degeneracy   If the Hamiltonian is time-reversal symmetric and $\lambda_{\mathcal{T}^2} = -1$, it immediately follows that any energy eigenstate $|n\rangle$ is (at least) doubly degenerate: there exists another state $\mathcal{T}|n\rangle$ with the same energy

$$H\mathcal{T}|n\rangle = \mathcal{T}H|n\rangle = \epsilon_n T|n\rangle \tag{2.9}$$

We sketch now a proof that $|n\rangle$ and $\mathcal{T}|n\rangle$ are distinct states. Suppose $|n\rangle$, $\mathcal{T}|n\rangle$ to be the same state. Then we would have $\mathcal{T}|n\rangle = e^{i\alpha}|n\rangle$. Therefore

$$\mathcal{T}^2|n\rangle = \mathcal{T}e^{i\alpha}|n\rangle = e^{-i\alpha}\mathcal{T}|n\rangle = e^{-i\alpha}e^{i\alpha}|n\rangle = |n\rangle$$

which implies $\mathcal{T}^2 = 1$, contradicting our hypothesis.

2.1.2   Charge (particle-hole) symmetry

Charge (or particle-hole) is an anti-unitary symmetry that relates a particle excitation with a hole excitation. Multiple definitions can be found in literature, often interchanging the two names. This variety seems to arise from the presence of two different concepts, which are in fact strongly related. **Charge** symmetry, inherited from the high-energy context, relates an excitation of charge $+q$ and energy $+\epsilon$ with an excitation of opposite charge $-q$ and opposite energy $-\epsilon$. **Particle-hole** symmetry instead, relates an excitation of charge $+q$ and energy $+\epsilon$ with an excitation of opposite charge $-q$ but equal energy[7]. These two concepts are strongly related, and therefore often interchanged. In this venture, we consider **charge** symmetry, since more popular in literature.

Given its anti-unitarity, $\mathcal{C}$ can be written as

$$\boxed{\mathcal{C} = U_C \cdot \mathcal{K}} \tag{2.10}$$

A Hamiltonian is said to be charge-symmetric if

$$\mathcal{C}H\mathcal{C}^{-1} = -H \qquad \rightarrow \qquad U_C H^* U_C^{-1} = -H$$

i.e. $\mathcal{C}$ anti-commutes with H. In momentum space, this relation reads

$$\boxed{U_C h_k^* U_C^{-1} = -h_{-k}}$$

where we used that anti-unitary symmetries flip the momentum. The anti-commutation relation has a strong consequence on the spectrum. For each energy level $+\epsilon$ indeed, another with opposite energy is guaranteed:

$$H\mathcal{C}|\epsilon\rangle = -\mathcal{C}H|\epsilon\rangle = -\epsilon\mathcal{C}|\epsilon\rangle \tag{2.11}$$

Given the same arguments used for $\mathcal{T}$, we can assert that $\mathcal{C}^2$ has two possible eigenvalues $\lambda_{\mathcal{C}^2} = \pm 1$.

---

[7]An example is given by the filled Fermi sphere of non-interacting electrons in presence of a positively charged background. One can obtain two excitations with equal energy by adding an electron or by removing one (adding a hole).

2.1.3 Exhaustivity

we show now that these two symmetries are exhaustive, meaning that we can write all the anti-unitary symmetries in terms of $\mathcal{T}$ and $\mathcal{C}$, and other unitary symmetries[29]. First, notice that $\mathcal{T}$ and $\mathcal{C}$ are not equivalent, since (when present) the first commutes with H, while the second anti-commutes.

Let's suppose the existence of a second anti-unitary operator, H-commuting. We name $\mathcal{T}_1$ and $\mathcal{T}_2$ the original and the new time-reversal operator respectively. Then we can define $\mathcal{T}_{12} \equiv \mathcal{T}_1 \mathcal{T}_2 = U_{T_1} U_{T_2}^*$. Because product of two anti-unitary operators, $\mathcal{T}_{12}$ is unitary and it commutes with H:

$$[\mathcal{T}_{12}, H] = \mathcal{T}_1 [\mathcal{T}_2, H] + [\mathcal{T}_1, H] \mathcal{T}_2 = 0$$

If not already done, $\mathcal{T}_{12}$ can be used to refine the block-diagonalization of the Hamiltonian, and the new time-reversal operators can be written as

$$\mathcal{T}_2 = \pm \mathcal{T}_1 \mathcal{T}_{12}$$

Therefore, all the possible anti-unitary operators that commute with H, are related through multiplication by unitary operators that commute with the Hamiltonian. We say that they are equivalent *modulo* (left) right-multiplication by a unitary operator. A similar procedure can be done for any new anti-unitary operator C_2 that anti-commutes with H, using that

$$[\mathcal{C}_{12}, H] = \mathcal{C}_1 \{\mathcal{C}_2, H\} - \{\mathcal{C}_1, H\} \mathcal{C}_2 = 0$$

After refining the block structure of H, there is no additional insight by considering different time-reversal (anti-unitary, H-commuting) or charge operators (anti-unitary, H-anticommuting). We can therefore safely consider just one $\mathcal{T}$ and one $\mathcal{C}$.

2.1.4 Chirality (sublattice), a particular unitary symmetry

Following the previous discussion, one may be convinced we exhausted the possible symmetries. There is however another one. Chirality (or sublattice), defined as the product of time-reversal and charge symmetry, is unitary (since the product of two anti-unitary) and anti-commutes with H.

$$\mathcal{S} = \mathcal{T}\mathcal{C} = U_T U_C^* \tag{2.12}$$

Sometimes, chirality is also defined as $\mathcal{S} = \mathcal{C}\mathcal{T}$. These two versions are equivalent, up to a change of basis. Chirality is indeed a distinct kind of symmetry, compared for example to $\mathcal{T}_{12}$ or $\mathcal{C}_{12}$. The reason is that, if the system is chiral-symmetric $\mathcal{S}$ anti-commutes with the Hamiltonian (instead of commuting):

$$\mathcal{S}H\mathcal{S}^{-1} = -H \tag{2.13}$$

This last relation can be written in momentum space by realising that momentum is unchanged by chiral symmetry (which is indeed the composition of two momentum-flipping transformations):

$$\boxed{\mathcal{S}h_k\mathcal{S}^{-1} = -h_k} \tag{2.14}$$

$\mathcal{S}$, therefore, cannot be included in the group of symmetry used to block-diagonalise the Hamiltonian. Again, we can consider only one chiral symmetry because any other unitary operator that anti-commutes with H is equivalent to $\mathcal{S}$ up to a multiplication by a unitary operator that commutes with H (following the procedure explained in section 2.1.3).

In chiral-symmetric systems, for each energy eigenvalue, another with an opposite value is present:

$$H\mathcal{S}\left|\epsilon\right> = -\mathcal{S}H\left|\epsilon\right> = -\epsilon\mathcal{S}\left|\epsilon\right>$$

By Schur's Lemma, the square of the chiral operator is a multiple of the identity:

$$\mathcal{S}^2 = e^{i\alpha}\mathbb{1} \tag{2.15}$$

Nothing can be said about the phase α. This because $\mathcal{S} = U_T U_C^*$ and the phases of U_T, U_C are arbitrary. Therefore, we only distinguish the case in which chirality is present ($\mathcal{S}^2 = 1$) or not ($\mathcal{S}^2 = 0$).

2.1.5   The Ten-Fold Way

Name	property	symm. relation	classification labels
Time-reversal	anti-unitary	$[\mathcal{T}, H] = 0$	$\mathcal{T}^2 = 0, \pm1$
Charge	anti-unitary	$\{\mathcal{C}, H\} = 0$	$\mathcal{C}^2 = 0, \pm1$
Chirality	unitary	$\{\mathcal{S}, H\} = 0$	$\mathcal{S}^2 = 0, 1$

Table 2.1: Additional symmetries of a quantum system. $\mathcal{T}, \mathcal{C}, \mathcal{S}$ are all the remaining symmetries left after exploiting all possible unitary and H-commuting symmetries that block-diagonalize the Hamiltonian.

We now have some tools to classify quantum Hamiltonians in terms of these symmetries. For time-reversal, we have three possible cases: the symmetry is present ($\mathcal{T}^2 = \pm1$) or not ($\mathcal{T}^2 = 0$). The same holds for charge symmetry. For each of these 3×3 cases, chiral symmetry is completely determined by the other two, excluding one: if $\mathcal{T}^2 = \mathcal{C}^2 = 0$ we could have $\mathcal{S}^2 = 0$ either $\mathcal{S}^2 = 1$. This last case happens when neither time reversal nor charge is present, but their composition is satisfied. We then have $9 + 1 = 10$ possibilities, giving rise to the *Ten-Fold Way* of classification.

2.1.6   Symmetries in second quantization

So far, we have described symmetries as operators acting on the first-quantized Hamiltonian. For interacting theories, however, it becomes convenient to express symmetries in second quantization. Because this formulation goes beyond the scope of this thesis, we are only going to sketch the main principles. We define symmetries in terms of their action on the field operators[29].

Unitarily realised symmetries   which commute with the Hamiltonian act as

$$\hat{\mathcal{U}}\,\hat{\psi}_i\,\hat{\mathcal{U}}^{-1} = \sum_j U_{ij}^\dagger\,\hat{\psi}_j \qquad\qquad \hat{\mathcal{U}}\,\hat{\psi}_i^\dagger\,\hat{\mathcal{U}}^{-1} = \sum_j \hat{\psi}_j^\dagger U_{jI} \tag{2.16}$$

where U is the respective first-quantized symmetry operator. These transformations reduce to the first quantized one ($UHU^{-1} = H$) when the theory is non-interacting.

Time reversal symmetry   is given by

$$\hat{\mathcal{T}}\,\hat{\psi}_i\,\hat{\mathcal{T}}^{-1} = \sum_j (U_T^\dagger)_{ij}\,\hat{\psi}_j \qquad\qquad \hat{\mathcal{T}}\,\hat{\psi}_i^\dagger\,\hat{\mathcal{T}}^{-1} = \sum_j \hat{\psi}_j^\dagger (U_T)_{ji} \tag{2.17}$$

Such transformation is antiunitary, as in first quantization.

Charge symmetry   requires some extra care. This transformation relates particles with holes, transforming creation into annihilation operators (and viceversa):

$$\hat{\mathcal{C}}\,\hat{\psi}_i\,\hat{\mathcal{C}}^{-1} = \sum_j (U_C^\dagger)_{ij}^*\,\hat{\psi}_j^\dagger \qquad\qquad \hat{\mathcal{C}}\,\hat{\psi}_i^\dagger\,\hat{\mathcal{C}}^{-1} = \sum_j \hat{\psi}_j (U_C)_{ji}^* \tag{2.18}$$

Surprisingly, charge conjugation is unitary in second quantization, but anti-unitary in first quantization, as one can check applying Eq2.18 to a non-interacting Hamiltonian.

Chirality (or sublattice)   relates particles with holes. However, contrarily to charge conjugation, it is *anti-unitary* in second quantization:

$$\hat{\mathcal{S}}\,\hat{\psi}_i\,\hat{\mathcal{S}}^{-1} = \sum_j (U_S^\dagger)_{ij}^*\,\hat{\psi}_j^\dagger \qquad\qquad \hat{\mathcal{S}}\,\hat{\psi}_i^\dagger\,\hat{\mathcal{S}}^{-1} = \sum_j \hat{\psi}_j (U_S)_{ji}^* \tag{2.19}$$

Symmetries operations which interchange particles with holes, are unitary in first quantization when anti-unitary in the second, and viceversa.

2.1.7   Tight-binding model in graphene

We apply the first-quantization formalism described above to the tight-binding model of spin $1/2$ particles hopping on the honeycomb lattice (graphene).

This system has two bands that touch at two independent Dirac points (valleys). By low-energy expansion around these points, one obtains a Hamiltonian that acts on the following Hilbert space:

$$\mathbb{H}_2 \equiv \underbrace{\mathbb{C}^2}_{\text{Spin space}} \otimes \underbrace{\mathbb{C}^2}_{\text{Valleys sp.}} \otimes \underbrace{\mathbb{C}^2}_{\text{Sublattices sp.}} \tag{2.20}$$

The full Hamiltonian in second quantization is given by

$$H = \sum_k \Psi_k^\dagger\,h(k)\,\Psi_k \tag{2.21}$$

where

$$\Psi = (A_{\uparrow+}, B_{\uparrow+}, A_{\uparrow-}, B_{\uparrow-}, A_{\downarrow+}, B_{\downarrow+}, A_{\downarrow-}, B_{\downarrow-},)^T \tag{2.22}$$

A, B are annihilation (creation) operators of the two distinct sublattices, the arrow index labels the spin degree of freedom, and the $\pm$ index labels the valley.

The single-particle Hamiltonian in momentum space is given by

$$h(k) = -v_f\left(s_0 \otimes \sigma_3 \otimes \tau_1\,k_x + s_0 \otimes \sigma_0 \otimes \tau_2\,k_y\right) \tag{2.23}$$

where s_i, σ_i, τ_i are Pauli matrices for $i = 1, 2, 3$, and the two-dimensional identity matrix for $i = 0$. They act on spin, valley and sublattice Hilbert spaces, respectively.

Time-reversal: Time reversal flips the spin and inverts the momenta, exchanging the two valleys. The two sublattices A, B are instead left unchanged. We therefore have:

$$\mathcal{T} = is_2 \otimes \sigma_1 \otimes \tau_0 \cdot \mathcal{K} \qquad \rightarrow \qquad U_T = is_2 \otimes \sigma_1 \otimes \tau_0 \tag{2.24}$$

where $\mathcal{K}$ is the complex conjugation operator, and U_T is unitary. The Bloch Hamiltonian $h(k)$ is time-reversal symmetric since $[h(k), \mathcal{T}] = 0$. One can also verify that $\mathcal{T}^2 = -\mathbb{1}$.

Chirality (sublattice) Before moving to charge, we first construct the sublattice (chirality) symmetry, and we derive charge conjugation in second place. Graphene is manifestly sublattice symmetric: its dispersion relation is made of two bands, symmetric w.r.t. the chemical potential $\mu = 0$. Sublattice flips the sign of one orbital w.r.t. to the other, leaving intact spin. The aspect of the operator in the valley degree of freedom requires extra care since the aspects of the Hamiltonian Eq.2.23 in the two valleys are not trivially related. One however can do a basis transformation for the fields $\Psi \rightarrow \Psi'$:

$$\Psi' = (B_{\uparrow+}, A_{\uparrow+}, A_{\uparrow-}, B_{\uparrow-}, B_{\downarrow+}, A_{\downarrow+}, A_{\downarrow-}, B_{\downarrow-},)^T \tag{2.25}$$

which results in a simpler form of the Hamiltonian:

$$h'(k) = -v_f\, s_0 \otimes \sigma_3 \otimes (\tau_1\, k_x + \tau_2\, k_y) \tag{2.26}$$

In this basis, it becomes immediate that the chiral symmetry has to pick up the respective signs of the Hamiltonians on each valley. Its form in the new and in the original basis is respectively

$$\begin{aligned} \mathcal{S}' &= s_0 \otimes \sigma_3 \otimes \tau_3 \\ \mathcal{S} &= s_0 \otimes \sigma_0 \otimes \tau_3 \end{aligned} \tag{2.27}$$

The Bloch Hamiltonian $h(k)$ is sublattice symmetric since $\{h(k), \mathcal{S}\} = 0$. One can also verify that $\mathcal{S}^2 = \mathbb{1}$.

It is instructive to neglect for a moment spin and valley degrees of freedom. In the sublattice space, the Hamiltonian becomes

$$h(k) = -v_f(k_x \tau_x + k_y \tau_y) \tag{2.28}$$

Thanks to the properties of Pauli matrices, it is immediate to see the existence of a third matrix (chirality matrix) τ_z which anti-commute with the Hamiltonian[8]. The situation would be drastically different for a system in 3+1 dimensions, with a generalised Hamiltonian $h(k) = k_x \tau_x + k_y \tau_y + k_z \tau_z$. A fourth anti-commuting matrix is not present, and we obtain massless fermions with a single chirality[18] at one Dirac point. By adding the valley degree of freedom chirality can be restored, obtaining nodes with opposite chirality. Differently from graphene, there is no possibility to gap out Dirac cones, since perturbation can only move them. The only way to obtain a gap is to join and annihilate the two nodes with opposite chirality. This is an example of a Weyl semimetal.

---

[8]Since the particles are massless, chirality and helicity are equivalent. One could indeed formulate the problem in terms of the helicity matrix which commute with the Hamiltonian, given by the projection of the sublattice pseudo-spin $\Sigma = (\tau_x, \tau_y)$ in the direction of motion:

$$\eta = \frac{\Sigma \cdot \vec{k}}{k}$$

Charge: We can finally obtain charge conjugation by inverting relation 2.12:

$$\mathcal{C} = \mathcal{T}^{-1} \cdot \mathcal{S} = -is_2 \otimes \sigma_1 \otimes \tau_3 \cdot \mathcal{K} \qquad \rightarrow \qquad U_C = is_2 \otimes \sigma_1 \otimes \tau_3 \tag{2.29}$$

where $\mathcal{K}$ is the complex conjugation operator, and U_C is unitary. One can verify that $\{h(k), \mathcal{C}\} = 0$, i.e. also charge symmetry is satisfied. Moreover, $\mathcal{C}^2 = -\mathbb{1}$. It is instructive to look at the action of $\mathcal{C}$ on the Schrodinger equation, when the system is coupled to an electromagnetic field, i.e. when the eigenvalue problem reads

$$-v_f \Big[s_0 \otimes \sigma_3 \otimes \tau_1 \left(-i\partial_x - eA_x \right) + s_0 \otimes \sigma_0 \otimes \tau_2 \left(-i\partial_y - eA_y \right) \Big] \psi = E\psi \tag{2.30}$$

The two terms of the Hamiltonian transform under charge conjugation as:

$$U_C \left[s_0 \otimes \sigma_3 \otimes \tau_1 \left(-i\partial_x - eA_x \right) \right]^* U_C^{-1} = U_C \left[s_0 \otimes \sigma_3 \otimes \tau_1 \right] U_C^{-1} \left(i\partial_x - eA_x \right)$$
$$= s_0 \otimes \sigma_3 \otimes \tau_1 \left(i\partial_x - eA_x \right)$$

$$U_C \left[s_0 \otimes \sigma_0 \otimes \tau_2 \left(-i\partial_y - eA_y \right) \right]^* U_C^{-1} = U_C \left[-s_0 \otimes \sigma_0 \otimes \tau_2 \right] U_C^{-1} \left(i\partial_y - eA_y \right)$$
$$= s_0 \otimes \sigma_0 \otimes \tau_2 \left(i\partial_y - eA_y \right)$$

since $[s_0 \otimes \sigma_3 \otimes \tau_1, U_C] = 0$ and $\{s_0 \otimes \sigma_0 \otimes \tau_2, U_C\} = 0$. The energy instead transforms as

$$\mathcal{C} E \mathcal{C}^{-1} = E$$

The total transformation then reads

$$-v_f \Big[s_0 \otimes \sigma_3 \otimes \tau_1 \left(-i\partial_x + eA_x \right) + s_0 \otimes \sigma_0 \otimes \tau_2 \left(-i\partial_y + eA_y \right) \Big] \psi' = -E\psi' \tag{2.31}$$

where $\psi' = \mathcal{C}\psi$. The charge-conjugate of ψ is therefore a field ψ' with opposite charge $(-e \rightarrow e)$ and opposite energy $(E \rightarrow -E)$. Its explicit form in the sublattice fields is

$$\mathcal{C}\Psi = \left(A_{\downarrow-}, -B_{\downarrow-}, A_{\downarrow+}, -B_{\downarrow+}, A_{\uparrow-}, -B_{\uparrow-}, A_{\uparrow+}, -B_{\uparrow+}, \right)^T \tag{2.32}$$

Note: We just showed how the low-energy expansion of the TB Hamiltonian in graphene is charge and chiral symmetric. However, this is the case when the chemical potential is tuned at $\mu = 0$. The filling of the lattice plays indeed an important role for the symmetries of the Hamiltonian and its ground state.

2.1.8 Tight-binding model on kagome lattice

Time reversal symmetry In the Hilbert space $\mathbb{H}_3$ time-reversal can be written as

$$\mathcal{T} = U_T \cdot \mathcal{K} = is_2 \otimes \sigma_1 \otimes \mathbb{1}_3 \cdot \mathcal{K} \tag{2.33}$$

The Hamiltonian is is $\mathcal{T}$-invariant since

$$\mathcal{T}\mathcal{H}(k)\mathcal{T}^{-1} = \mathcal{H}(-k) \qquad \rightarrow \qquad U_T \mathcal{H}^*(k) U_T^{-1} = \mathcal{H}(-k)$$

The form of $\mathcal{T}$ in the low-energy subspace is immediately found:

$$\mathcal{T} = is_2 \otimes \sigma_1 \otimes \tau_0 \cdot \mathcal{K} \tag{2.34}$$

where τ_0 is the identity operator.

Chirality (sublattice) symmetry   Differently from graphene, the full kagome Hamiltonian does not enjoy chiral symmetry, nor charge symmetry. The third, flat band makes the spectrum unsymmetrical under a sign flip. However, if the chemical potential is specifically tuned at the middle of the two symmetric bands (1/3 filling if the flat band sits on top, either 2/3 if it sits on the bottom) and only low-energy effects are considered, one can neglect the coupling with the flat band. The deriving low energy theory is, under this approximation, charge and chiral symmetric. We focus on such a case, working in the Hilbert space $\mathbb{H}_2$ in the decoupled representation (denoted with a Tilde in section 1.4.2), where the low-energy Hamiltonian has the form

$$h(k) = -v_f \; s_0 \otimes \sigma_3 \otimes (k_1 \; \tau_3 + k_2 \; \tau_1) \tag{2.35}$$

The chiral operator is proportional to τ_2 in the sublattice Hilbert space, spin-independent and it takes the respective signs in the two valleys:

$$\mathcal{S} = s_0 \otimes \sigma_3 \otimes \tau_2 \tag{2.36}$$

Charge (particle-hole) symmetry   Charge symmetry $\mathcal{C}$ (often labelled as *particle-hole* symmetry) can be obtained by the combination of time-reversal and the inverse of sublattice symmetry:

$$\mathcal{C} = \mathcal{T} \cdot \mathcal{S}^{-1}$$

The simplest form is obtained in the low-energy subspace $\mathbb{H}_2$, where

$$\mathcal{C} = U_C \cdot \mathcal{K} = s_2 \otimes \sigma_2 \otimes \tau_2 \cdot \mathcal{K} \tag{2.37}$$

The Bloch Hamiltonian is charge-symmetric since

$$\mathcal{C}h(-k)\mathcal{C}^{-1} = -h(k) \qquad \rightarrow \qquad U_C h^*(-k) U_C^{-1} = -h(k)$$

Note again that these relations for $\mathcal{C}$ and $\mathcal{S}$ hold only if we specifically set the chemical potential and we neglect the coupling flat band. Extra care is needed if one wants to work in $\mathbb{H}_3$.

2.2 Lattice symmetries: p6m wallpaper group

Both honeycomb and kagome lattice symmetries are encoded in the wallpaper group p6m: these consist of 6 reflection axis, 1 rotation centre of order six, 2 of order three, and 3 of order two [27].

2.2.1 Reflections
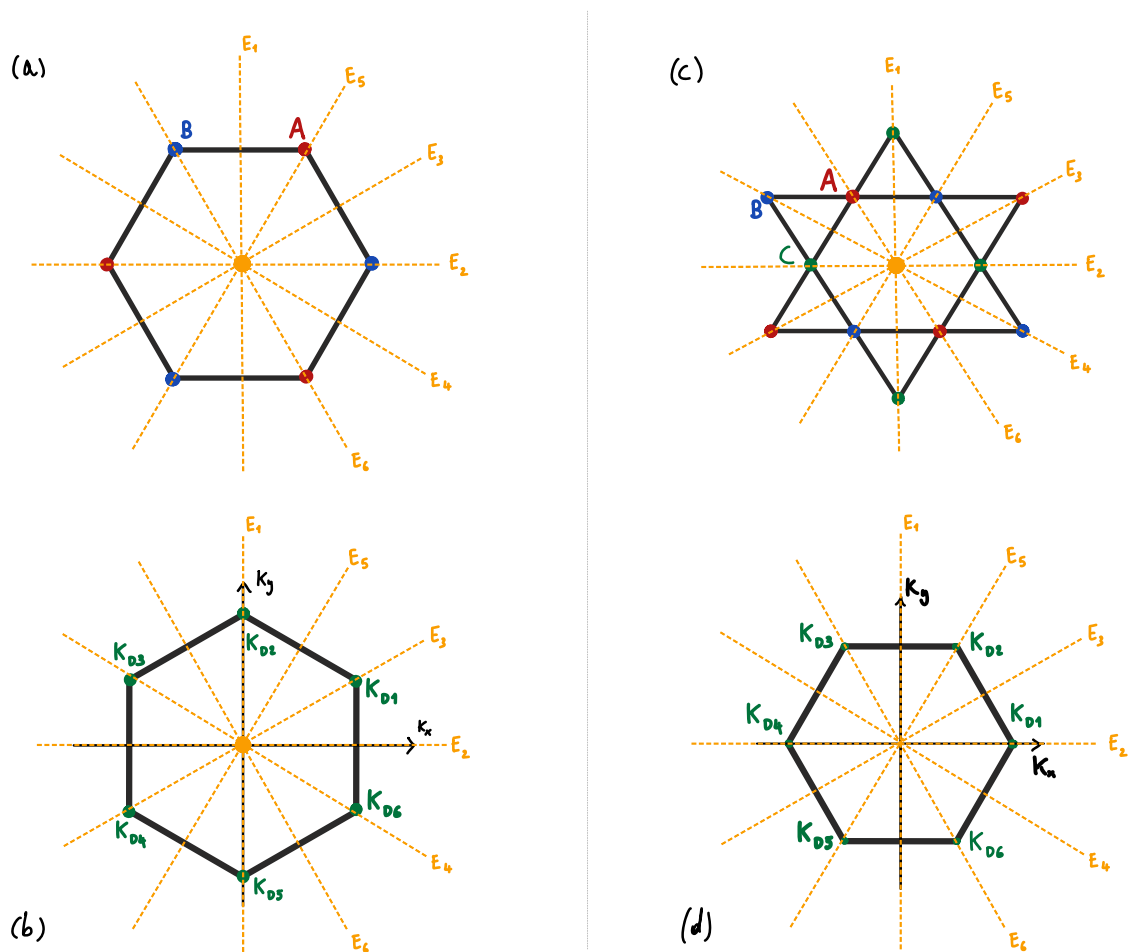
Figure 2.2: Reflection symmetries of the honeycomb lattice **(a)**, its Brullouin zone **(b)**, the kagome lattice **(c)** and **(d)** its Brullouin zone.

The general procedure to construct reflections is the following. One performs first a parity transformation (inversion), and subsequently a rotation of π around an axis $\vec{n}$ perpendicular to the one of reflection. The spin $\vec{s}$ is invariant under parity and transforms as a spin under the rotation around $\vec{n}$:

$$R_{\vec{n}}(\theta) = \exp\left(-i\theta\vec{n}\cdot\vec{s}\right) = \mathbb{1}\cos\left(\frac{\theta}{2}\right) - i\vec{n}\cdot\vec{s}\sin\left(\frac{\theta}{2}\right) \tag{2.38}$$

In two dimensions, one could figure the reflection uniquely as a rotation of π around the reflection axis. This procedure however flips the z component perpendicular to the $x - y$ plane, which is not consistent with a reflection. In addition, the spin would not transform correctly. The reader can convince himself of the difference with a simple experiment: he has to give one side to a mirror, and use one hand to simulate a spin in one direction parallel to the mirror plane (see Figure 2.3). He will observe the hand of his reflected twin spinning in the opposite direction. This is correctly described by π-rotation of the spin around one axis perpendicular to the mirror, and not parallel to it.

Figure 2.3: A spin parallel to a mirror plane gets reverted by reflection. We thank E. Muzzin for the drawing.

Geometrical symmetries in low-energy approximation require extra care: one has indeed to be careful about the origin of the expansion, and how it transforms under the symmetry. Let's consider an example: E_1 transforms K_{D1} into K_{D3} for honeycomb lattice, and K_{D1} into K_{D4} for kagome lattice; E_2 instead transforms K_{D1} into K_{D6} in graphene, and keeps K_{D1} unchanged in kagome (S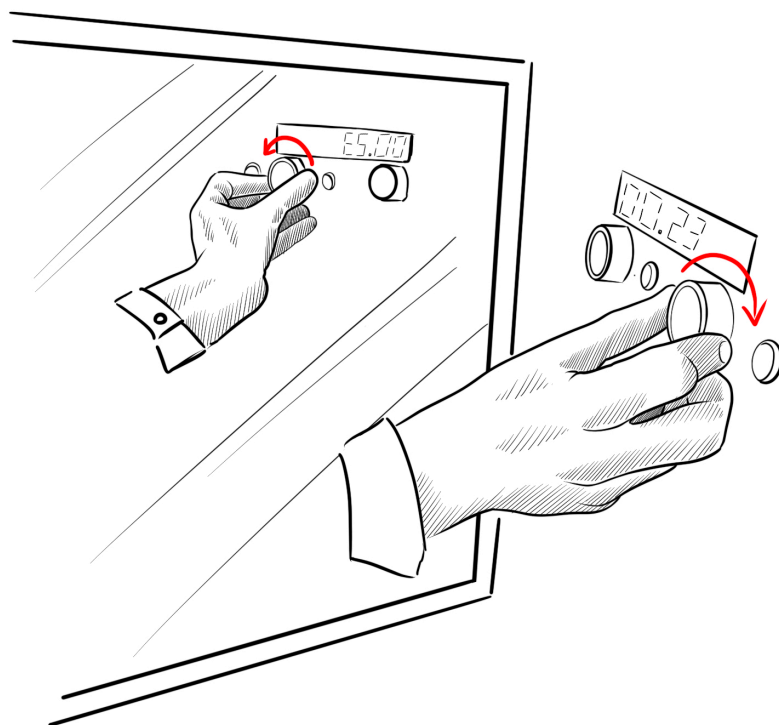ee Fig. 2.2). In general, these operations transform the Hamiltonian expanded around two Dirac points - let's say K_{Di}, K_{Dj} - into a Hamiltonian expanded around two different Dirac points K_{Dk}, K_{Dl}. While the full Hamiltonian has all the symmetry of the model (any of these transformations sends $H \to H$), its low-energy approximations are "less symmetric", meaning that any of these might be transformed one into another under symmetry operations: $H_{ij} \to H_{kl}$.

E1

Reflection $E1$ with respect to the y-axis transforms the spin with a rotation of π around the x-axis: $R_{\vec{x}}(\pi) = -is_1$. Its action on the momenta sends $k = (k_x, k_y) \to (-k_x, k_y)$. The valleys are untouched in graphene and swapped in kagome. Sublattices transform as $A \to B$, $B \to A$ in honeycomb lattice, and as $A \to B$, $B \to A$, $C \to C$ in kagome. Its operators are given by

$$E_1^{\bigcirc} = -is_1 \otimes \sigma_0 \otimes \tau_1 \tag{2.39}$$

$$E_1^{\text{✡}} = -is_1 \otimes \sigma_1 \otimes \begin{pmatrix} 0 & 1 & 0 \\ 1 & 0 & 0 \\ 0 & 0 & 1 \end{pmatrix} \tag{2.40}$$

The low energy Hamiltonians transform as

$$\bigcirc : \qquad E_1 H_{14}(k_x, k_y) E_1^{-1} = H_{14}(-k_x, k_y)$$
$$\text{✡} : \qquad E_1 H_{14}(k_x, k_y) E_1^{-1} = H_{36}(-k_x, k_y)$$

E2

Reflection $E2$ with respect to the x-axis transforms the spin with a rotation of π around the y-axis: $R_{\vec{y}}(\pi) = -is_3$. Its action on the momenta sends $k = (k_x, k_y) \to (k_x, -k_y)$, so that the valleys are swapped in graphene and untouched in kagome.

$$E_2^{\bigcirc} = -is_2 \otimes \sigma_1 \otimes \tau_0 \tag{2.41}$$

$$E_2^{\text{✡}} = -is_2 \otimes \sigma_0 \otimes \begin{pmatrix} 0 & 1 & 0 \\ 1 & 0 & 0 \\ 0 & 0 & 1 \end{pmatrix} \tag{2.42}$$

The kagome Hamiltonian transforms as

$$\bigcirc : \qquad E_2 H_{14}(k_x, k_y) E_2^{-1} = H_{14}(k_x, -k_y)$$
$$\text{✡} : \qquad E_2 H_{14}(k_x, k_y) E_2^{-1} = H_{36}(k_x, -k_y)$$

E3

Reflection $E3$ transforms the kagome sublattices as $A \to A$, $C \to B$, $B \to C$, and as $A \leftrightarrow B$ in graphene. Its action on the momenta sends $k = (k_x, k_y) \to k' = \left(\frac{k_x}{2} + \frac{\sqrt{3}}{2} k_y, \frac{\sqrt{3}}{2} k_x - \frac{k_y}{2} \right)$. The

spin transforms under a rotation of π around the axis parallel to the vector $\vec{n} = (-1/2, \sqrt{3}/2)$. Its operators are given by

$$E_3^{\bigcirc} = -\frac{i}{2}\left(-s_1 + \sqrt{3}s_y\right) \otimes \sigma_0 \otimes \tau_1 \tag{2.43}$$

$$E_3^{\maltese} = -\frac{i}{2}\left(-s_1 + \sqrt{3}s_y\right) \otimes \sigma_1 \otimes \begin{pmatrix} 1 & 0 & 0 \\ 0 & 0 & 1 \\ 0 & 1 & 0 \end{pmatrix} \tag{2.44}$$

The Hamiltonians transform as

$$\bigcirc: \qquad E_3 H_{14}(k_x, k_y) E_3^{-1} = H_{14}(k_1', k_2')$$
$$\maltese: \qquad E_3 H_{12}(k_x, k_y) E_3^{-1} = H_{12}(k_1', k_2')$$

E4

Reflection $E4$ transforms the momenta as $k = (k_x, k_y) \rightarrow k' = \left(\frac{k_x}{2} - \frac{\sqrt{3}}{2}k_y, \frac{-\sqrt{3}}{2}k_x - \frac{k_y}{2}\right)$. The spin transforms under a rotation of π around the axis parallel to the vector $\vec{n} = (1/2, \sqrt{3}/2)$. Its operators are given by

$$E_4^{\bigcirc} = -\frac{i}{2}\left(s_1 + \sqrt{3}s_y\right) \otimes \sigma_o \otimes \tau_1 \tag{2.45}$$

$$E_4^{\maltese} = -\frac{i}{2}\left(s_1 + \sqrt{3}s_y\right) \otimes \sigma_1 \otimes \begin{pmatrix} 0 & 0 & 1 \\ 0 & 1 & 0 \\ 1 & 0 & 0 \end{pmatrix} \tag{2.46}$$

Expanding the Hamiltonian around K_{D1} and K_{D6}, one can show that the symmetry holds since

$$\bigcirc: \qquad E_4 H_{36}(k_x, k_y) E_4^{-1} = H_{36}(k_1', k_2')$$
$$\maltese: \qquad E_4 H_{16}(k_x, k_y) E_4^{-1} = H_{16}(k_1', k_2')$$

E5

Reflection $E5$ transforms the momenta as $k = (k_x, k_y) \rightarrow k' = \left(-\frac{k_x}{2} + \frac{\sqrt{3}}{2}k_y, \frac{\sqrt{3}}{2}k_x + \frac{k_y}{2}\right)$. The spin transforms under a rotation of π around the axis parallel to the vector $\vec{n} = (-\sqrt{3}/2, 1/2)$. Its operators are given by

$$E_5^{\bigcirc} = -\frac{i}{2}\left(-\sqrt{3}s_1 + s_y\right) \otimes \sigma_1 \otimes \tau_0 \tag{2.47}$$

$$E_5^{\maltese} = -\frac{i}{2}\left(-\sqrt{3}s_1 + s_y\right) \otimes \sigma_0 \otimes \begin{pmatrix} 0 & 0 & 1 \\ 0 & 1 & 0 \\ 1 & 0 & 0 \end{pmatrix} \tag{2.48}$$

One can show that the symmetry holds since

$$\bigcirc: \qquad E_5 H_{12}(k_x, k_y) E_5^{-1} = H_{12}(k_1', k_2')$$
$$\maltese: \qquad E_5 H_{52}(k_x, k_y) E_5^{-1} = H_{52}(k_1', k_2')$$

E6

Reflection $E6$ transforms the momenta as $k = (k_x, k_y) \to k' = \left(-\frac{k_x}{2} - \frac{\sqrt{3}}{2}k_y, -\frac{\sqrt{3}}{2}k_x + \frac{k_y}{2} \right)$. The spin transforms under a rotation of π around the axis parallel to the vector $\vec{n} = (\sqrt{3}/2, 1/2)$. Its operators are given by

$$E_6^{\bigcirc} = -\frac{i}{2} \left(\sqrt{3}s_1 + s_y \right) \otimes \sigma_1 \otimes \tau_0 \tag{2.49}$$

$$E_6^{\text{✡}} = -\frac{i}{2} \left(\sqrt{3}s_1 + s_y \right) \otimes \sigma_0 \otimes \begin{pmatrix} 1 & 0 & 0 \\ 0 & 0 & 1 \\ 0 & 1 & 0 \end{pmatrix} \tag{2.50}$$

The Hamiltonians transform as

$$\bigcirc: \qquad E_6 H_{32}(k_x, k_y) E_6^{-1} = H_{32}(k_1', k_2')$$
$$\text{✡}: \qquad E_6 H_{36}(k_x, k_y) E_6^{-1} = H_{36}(k_1', k_2')$$

2.2.2 Rotations
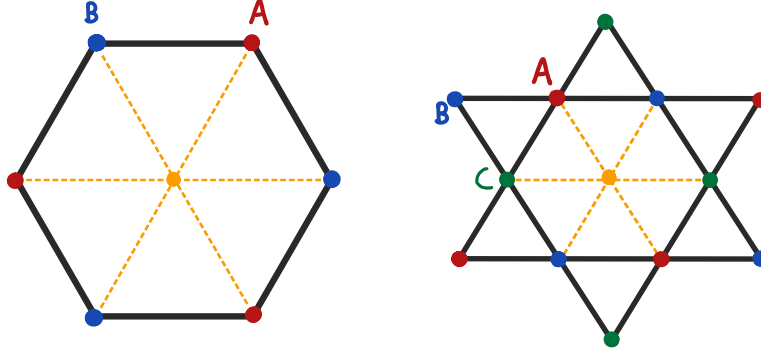
Figure 2.4: Rotation centre of order six in honeycomb and kagome lattice

In this section, we consider rotation around the centre of the hexagons (centre of order six).

R11: rotation of $\pi/3$

This rotation exchanges the graphene sublattice and transforms the kagome ones as $A \to C$, $B \to A$, $C \to B$. Its action on the momenta sends $k = (k_x, k_y) \to k' = \left(\frac{k_x}{2} + \frac{\sqrt{3}}{2}k_y, -\frac{\sqrt{3}}{2}k_x + \frac{k_y}{2} \right)$. The full operator is given by

$$R_{11}^{\bigcirc} = \frac{1}{2} \left(\sqrt{3}s_0 - is_3 \right) \otimes \sigma_1 \otimes \tau_1 \tag{2.51}$$

$$R_{11}^{\text{✡}} = \frac{1}{2} \left(\sqrt{3}s_0 - is_3 \right) \otimes \sigma_1 \otimes \begin{pmatrix} 0 & 0 & 1 \\ 1 & 0 & 0 \\ 0 & 1 & 0 \end{pmatrix} \tag{2.52}$$

The Hamiltonians transform

$$\varhexagon, \varstar : \qquad R_{11}H_{14}(k)R_{11}^{-1} = H_{25}(k')$$

R12: rotation of $2\pi/3$

The action on the momenta sends $k = (k_x, k_y) \rightarrow k' = \left(-\frac{k_x}{2} + \frac{\sqrt{3}}{2}k_y, -\frac{\sqrt{3}}{2}k_x - \frac{k_y}{2}\right)$. The full operator is given by

$$R_{12}^{\varhexagon} = \frac{1}{2}\left(s_0 - i\sqrt{3}s_3\right) \otimes \sigma_0 \otimes \tau_0 \tag{2.53}$$

$$R_{12}^{\varstar} = \frac{1}{2}\left(s_0 - i\sqrt{3}s_3\right) \otimes \sigma_0 \otimes \begin{pmatrix} 0 & 1 & 0 \\ 0 & 0 & 1 \\ 1 & 0 & 0 \end{pmatrix} \tag{2.54}$$

The Hamiltonian H_{14} transform under R_{12} as

$$\varhexagon, \varstar : \qquad R_{12}H_{14}(k)R_{12}^{-1} = H_{36}(k')$$

R13: rotation of π

This particular transformation inverts the momenta $k \rightarrow -k$.

$$R_{13}^{\varhexagon} = -is_3 \otimes \sigma_1 \otimes \tau_1 \tag{2.55}$$

$$R_{13}^{\varstar} = -is_3 \otimes \sigma_1 \otimes \mathbb{1}_3 \tag{2.56}$$

The Hamiltonian transforms as

$$\varhexagon, \varstar : \qquad R_{13}H_{14}(k)R_{13}^{-1} = H_{14}(-k)$$

R14, R15

The operators for rotations of $-2\pi/3$ and $-\pi/3$ are respectively given by

$$R_{14}^{\varhexagon} = \frac{1}{2}\left(s_0 + i\sqrt{3}s_3\right) \otimes \sigma_1 \otimes \tau_1 \tag{2.57}$$

$$R_{14}^{\varstar} = \frac{1}{2}\left(s_0 + i\sqrt{3}s_3\right) \otimes \sigma_0 \otimes \begin{pmatrix} 0 & 0 & 1 \\ 1 & 0 & 0 \\ 0 & 1 & 0 \end{pmatrix} \tag{2.58}$$

$$R_{15}^{\varhexagon} = \frac{1}{2}\left(\sqrt{3}s_0 + is_3\right) \otimes \sigma_0 \otimes \tau_0 \tag{2.59}$$

$$R_{15}^{\varstar} = \frac{1}{2}\left(\sqrt{3}s_0 + is_3\right) \otimes \sigma_1 \otimes \begin{pmatrix} 0 & 1 & 0 \\ 0 & 0 & 1 \\ 1 & 0 & 0 \end{pmatrix} \tag{2.60}$$

Note that these operators remind us of R_{11} and R_{12} respectively, but with the opposite valley relation (swapped instead of untouched, or viceversa). The symmetry relations are the same as R_{11}, R_{12}, but with $k \rightarrow -k'$.

2.3 Symmetries of the mass terms

We finally have all the tools to classify the bilinear mass terms, according to the symmetries they break or preserve. Table 2.2 shows such classification for graphene and kagome lattice, respectively. These results are partially present in literature for graphene[33]. A similar classification for kagome mass terms, however, was not known at the time of writing.

Honeycomb lattice (graphene)															
Idx ijk	Parity	T-rev	Char	Chiral	E1	E2	E3	E4	E5	E6	R11	R12	R13	R14	R15
{0,0,3}	×	✓	×	×	×	✓	×	×	✓	✓	×	✓	×	✓	×
{0,1,1}	✓	✓	✓	✓	✓	✓	✓	✓	✓	✓	✓	✓	✓	✓	✓
{0,2,1}	×	✓	✓	✓	✓	×	✓	✓	×	×	×	✓	×	✓	×
{0,3,3}	✓	×	✓	×	×	×	×	×	×	×	✓	✓	✓	✓	✓
{1,0,3}	×	×	✓	×	×	×	×	×	×	×	×	×	✓	×	×
{2,0,3}	×	×	✓	×	✓	✓	×	×	×	×	×	×	✓	×	×
{3,0,3}	×	×	✓	×	✓	×	✓	✓	×	×	×	✓	×	✓	×
{1,1,1}	✓	×	×	✓	✓	×	×	×	×	×	×	×	×	×	×
{2,1,1}	✓	×	×	✓	×	✓	×	×	×	×	×	×	×	×	×
{3,1,1}	✓	×	×	✓	×	×	×	×	×	×	✓	✓	✓	✓	✓
{1,2,1}	×	×	×	✓	✓	✓	×	×	×	×	×	×	✓	×	×
{2,2,1}	×	×	×	✓	×	×	×	×	×	×	×	×	✓	×	×
{3,2,1}	×	×	×	✓	×	✓	×	×	✓	✓	×	✓	×	✓	×
{1,3,3}	✓	✓	×	×	×	✓	×	×	×	×	×	×	×	×	×
{2,3,3}	✓	✓	×	×	✓	×	×	×	×	×	×	×	×	×	×
{3,3,3}	✓	✓	×	×	✓	✓	✓	✓	✓	✓	✓	✓	✓	✓	✓

Kagome lattice															
Idx ijk	Parity	T-rev	Char	Chiral	E1	E2	E3	E4	E5	E6	R11	R12	R13	R14	R15
{0,0,2}	✓	×	✓	×	×	×	×	×	×	×	✓	✓	✓	✓	✓
{0,1,0}	✓	✓	✓	✓	✓	✓	✓	✓	✓	✓	✓	✓	✓	✓	✓
{0,2,0}	×	✓	✓	✓	×	✓	×	×	✓	✓	×	✓	×	✓	×
{0,3,2}	×	✓	×	×	✓	×	✓	✓	×	×	×	✓	×	✓	×
{1,1,0}	✓	×	×	✓	✓	×	×	×	×	×	×	×	×	×	×
{2,1,0}	✓	×	×	✓	×	✓	×	×	×	×	×	×	×	×	×
{3,1,0}	✓	×	×	✓	×	×	×	×	×	×	✓	✓	✓	✓	✓
{1,2,0}	×	×	×	✓	×	×	×	×	×	×	×	×	✓	×	×
{2,2,0}	×	×	×	✓	✓	✓	×	×	×	×	×	×	✓	×	×
{3,2,0}	×	×	×	✓	✓	×	✓	✓	×	×	×	✓	×	✓	×
{1,0,2}	✓	✓	×	×	×	✓	×	×	×	×	×	×	×	×	×
{2,0,2}	✓	✓	×	×	✓	×	×	×	×	×	×	×	×	×	×
{3,0,2}	✓	✓	×	×	✓	✓	✓	✓	✓	✓	✓	✓	✓	✓	✓
{1,3,2}	×	×	✓	×	✓	✓	×	×	×	×	×	×	✓	×	×
{2,3,2}	×	×	✓	×	×	×	×	×	×	×	×	×	✓	×	×
{3,3,2}	×	×	✓	×	×	✓	×	×	✓	✓	×	✓	×	✓	×

Table 2.2: **Graphene and kagome gap terms** and their symmetries.

Chapter 3

Mass terms

MAGNETIC DISCUSSION

3.1 Graphene masses and their symmetries

In this section, we are going to explore the variety of graphene mass terms, and link them to physical phenomena. We will carry out detailed derivation for the most significant ones.

3.1.1 Staggered potential

One simple term is given by an on-site potential which takes two different values $V = \pm\mu$ on the two sublattices A,B. This term was proposed in 1984 by Semenoff, who was studying 2+1 QED theories and their anomalies, and naturally looked at graphene as a prominent condensed matter realization [35]. The staggered potential corresponds to $\mathcal{M}_{003}$, which consistently preserves time-reversal symmetry but breaks sublattice (chiral) and charge symmetry. The resulting phase is a trivial insulating phase, with a gap at the 6 Dirac points.

3.1.2 Haldane mass and the anomalous quantum Hall effect
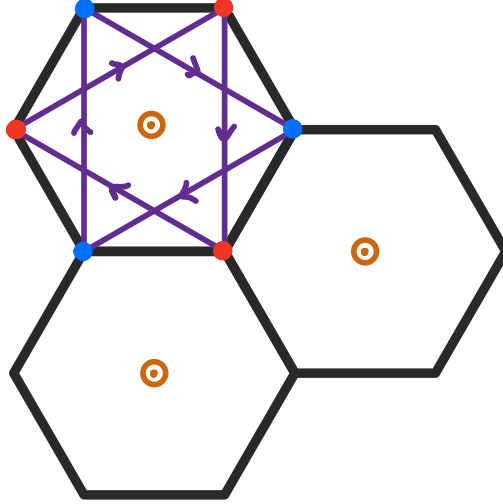
Figure 3.1: Haldane model on graphene lattice: arrows indicate hopping direction with a positive phase. NN hoppings acquire a null phase, since the flux through the unit cell is zero.

In 1987 Haldane proposed a model of the quantum Hall effect (QHE) on graphene, characterized by no magnetic flux through the unit cell [36]. This realisation can be obtained by placing one magnetic moment at the centre of each unit cell, ferromagnetically aligned in the direction perpendicular to the 2D plane. We investigate how this magnetic field affects the TB Hamiltonian. Using Peierls substitution, the nearest-neighbour (NN) hopping amplitude t acquires a phase $t \to te^{i\theta}$, which is proportional to the integral of the vector potential along the hopping path ξ:

$$\theta = \frac{q}{\hbar} \int_{\xi} \mathbf{A}(\mathbf{r}) \cdot d\mathbf{r} \tag{3.1}$$

A closed path made of only NN hoppings results in an overall phase in the hopping amplitude $\phi_{tot} = N\phi$ (N here is the number of NN hops) which is proportional to the integral of $\mathbf{A(r)}$ along the closed path. The closed-path integral is equal to the flux of the magnetic field through the area enclosed by the path (Stokes theorem). Such area is (an integer multiple of) the unit cell, which is traversed by a null flux:

$$N\theta = \frac{q}{\hbar} \oint_{\xi} \mathbf{A(r)} \cdot \mathbf{dr} = \frac{q}{\hbar} \int_{\Sigma} (\nabla \times \mathbf{A}) \cdot d^2\Sigma = \frac{q}{\hbar} \int_{\Sigma} (\mathbf{B}) \cdot d^2\Sigma = 0 \tag{3.2}$$

In conclusion, the nearest-neighbour hopping amplitude is not affected by such kind of magnetic fields. However, if one includes second-nearest neighbour hoppings (with amplitude t_2), one has to take into account the non-zero flux enclosed by their path. This results in the hopping amplitude gaining a phase $t_2 \to t_2 e^{\pm i\phi}$, which sign depends on the hopping direction (see Figure 3.1). The resulting contribution to the TB Hamiltonian becomes

$$H_{QHE} = t_2 \sum_i \left[e^{-i\phi} \left(a_i^\dagger a_{i+\alpha_1} + a_i^\dagger a_{i+\alpha_2} \right) + e^{i\phi} \left(a_i^\dagger a_{i-\alpha_1} + a_i^\dagger a_{i-\alpha_2} \right) \right] + \boxed{a \leftrightarrow b, \ \ \phi \leftrightarrow -\phi} \tag{3.3}$$

$$= t_2 \sum_k \left[e^{i\phi} \left(e^{ik\alpha_1} + e^{ik\alpha_2} \right) + e^{-i\phi} \left(e^{-ik\alpha_1} + e^{-ik\alpha_2} \right) \right] a_k^\dagger a_k + \boxed{a \leftrightarrow b, \ \ \phi \leftrightarrow -\phi} \tag{3.4}$$

$$= 2t_2 \sum_k \left[\cos\phi \sum_j \cos(k \cdot \alpha_j) - \sin\phi \sum_j \sin(k \cdot \alpha_j) \right] a_k^\dagger a_k + \boxed{a \leftrightarrow b, \ \ \phi \leftrightarrow -\phi} \tag{3.5}$$

$$= 2t_2 \sum_k \begin{pmatrix} a_k^\dagger \\ b_k^\dagger \end{pmatrix}^T \left[\cos\phi \sum_j \cos(k \cdot \alpha_j)\,\tau_0 - \sin\phi \sum_j \sin(k \cdot \alpha_j)\,\tau_3 \right] \begin{pmatrix} a_k \\ b_k \end{pmatrix} \tag{3.6}$$

We expand this Hamiltonian around the two Dirac points $K_{D1,2}$ using that $\forall j$

$$\cos(K_{D1} \cdot \alpha_j) = -\frac{1}{2} \qquad\qquad\qquad \cos(K_{D2} \cdot \alpha_j) = -\frac{1}{2} \tag{3.7}$$

$$\sin(K_{D1} \cdot \alpha_j) = -\frac{\sqrt{3}}{2} \qquad\qquad\qquad \sin(K_{D2} \cdot \alpha_j) = \frac{\sqrt{3}}{2} \tag{3.8}$$

Including spin and valley degrees of freedom, the low-energy Hamiltonian becomes

$$H_{QHE} = -2t_2 \cos\phi \left[s_0 \otimes \sigma_0 \otimes \tau_0 \right] - \sqrt{3}t_2 \sin\phi \left[s_0 \otimes \sigma_3 \otimes \tau_3 \right] \tag{3.9}$$

While the first term (proportional to $\mathcal{M}_{000}$) can be seen as a shift of the chemical potential, the second term opens a gap at the Dirac points, and it corresponds to $\mathcal{M}_{033}$. In the presence of this magnetic field, time-reversal is broken, while inversion symmetry is preserved. All reflection symmetries are broken, while all rotations are preserved, as one can check by the sketch in Figure 3.1.

Chern insulator on the honeycomb lattice   When Haldane's model and the staggered potential are simultaneously introduced, the parameters can be tuned to close the gap exclusively at one of the two Dirac points. As result, a conducting state appears on the surface, while the bulk remains gapped [36]. Such configuration resembles the Quantum Hall Effect, even though the total magnetic flux is zero. For this reason, it has been named "Anomalous Quantum Hall Effect". This phase is topologically protected: The conducting surface state is a global property, and it's therefore protected by local perturbation. The transverse conductance is indeed quantized and related to a topological feature, the Berry curvature. This phase cannot be adiabatically deformed into a trivial insulating one, without closing the gap in the bulk.

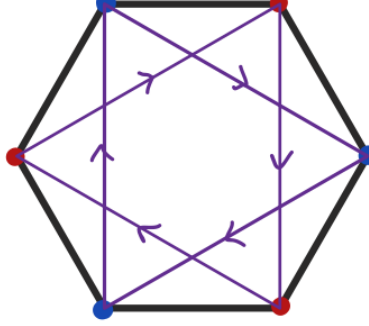### 3.1.3 Spin orbit coupling and the quantum spin Hall effect

Figure 3.2: Spin-orbit coupling on the hexagonal lattice: arrows indicate hopping direction with a positive factor $+\lambda$ for a spin up (reversed for a spin down). NN hoppings have no angular momentum, as one can prove by reflecting the plane with respect to the NN axis.

Spin-orbit coupling (SOC) emerges for spinful electrons in motion through an electrostatic field, when a non-zero angular momentum is present. Assuming SO interaction to open a gap, we expect the corresponding mass term to be time-reversal invariant. In addition, we expect all the lattice rotation symmetries to be preserved in the planar configuration. In Table 2.2, the only spin-dependent mass terms which are $\mathcal{T}$-invariant are $\mathcal{M}_{j33}$, for $j = 1, 2, 3$. In this section, we are going to derive the microscopic form of the intrinsic SO interaction, and show it corresponds to these terms. Following the work of Kane and Mele [37], we'll relate SO interaction with the quantum spin Hall effect.

In the lattice description, we consider the electrostatic potential generated by the nuclei's periodic arrangement and its effect on the spinful, hopping electrons. For the honeycomb lattice, it's simple to observe that such interaction vanishes for nearest neighbour (NN) hoppings. Taking any NN bond as a reflection axis, the lattice is transformed into itself, indicating a vanishing angular momentum. A finite contribution comes instead from next-nearest neighbours (NNN) hoppings: the path α_{ij} connecting two NNN sites ij corresponds to the angular momentum

$$L_{ij} = \sin\left(\theta_{ikj}\right) \delta_{ik} \times \delta_{kj} = \frac{\ell^2 \sqrt{3}}{2} \hat{\delta}_{ik} \times \hat{\delta}_{kj}$$

where δ_{ik}, δ_{kj} are the two NN traversed vectors of length ℓ, and $\hat{\delta}_{ik}, \hat{\delta}_{kj}$ the corresponding versors. In a planar setup, the angular momentum always points orthogonal to the plane, therefore only the z spin component is retained. The Hamiltonian is:

$$H_{soc} = i\lambda \sum_{\langle\langle i,j \rangle\rangle} \sum_{\nu} \left(L_{ij}^{\nu} \cdot s_{\alpha\beta}^{\nu} \right) \psi_{i\alpha}^{\dagger} \psi_{j\beta}$$

$$= i\lambda \sum_{\langle\langle i,j \rangle\rangle} \nu_{ij} \left(\psi_{i\uparrow}^{\dagger} \psi_{j\uparrow} - \psi_{i\downarrow}^{\dagger} \psi_{j\downarrow} \right) \tag{3.10}$$

where we absorbed the factor $\frac{\sqrt{3}\ell^2}{2}$ into the SOC amplitude λ. The sign of the contribution is contained in $\nu_{ij} = \pm 1$. For fixed spin and reversed path the contribution changes sign, so that

$\nu_{ij} = -\nu_{ji}$. The hopping directions for a positive contribution to a up-spin are drawn in Figure 3.2. Defining as α_j the NNN vectors, the Hamiltonian takes the form

$$H_{soc} = i\lambda \sum_{i \in A} \sum_{j=1}^{3} \left[a_{i,\uparrow}^{\dagger} a_{i+\alpha_j,\uparrow} - a_{i,\downarrow}^{\dagger} a_{i+\alpha_j,\downarrow} \right] - \boxed{a \leftrightarrow b} \tag{3.11}$$

After Fourier transform:

$$H_{soc} = -\lambda \sum_{k} \sum_{j} a_{k}^{\dagger} a_{k} \sin\left(k \cdot \alpha_j\right) - \boxed{a \leftrightarrow b}$$

$$= -\lambda \sum_{k} \Phi_{k}^{\dagger} \left[s_3 \otimes \begin{pmatrix} \sum_{j} \sin\left(k \cdot \alpha_j\right) & 0 \\ 0 & -\sum_{j} \sin\left(k \cdot \alpha_j\right) \end{pmatrix} \right] \Phi_{k}$$

$$\tag{3.12}$$

At the Dirac points the Hamiltonian results in the mass term $\mathcal{M}_{333}$:

$$H_{soc} \simeq -\lambda \left[s_3 \otimes \sigma_3 \otimes \tau_3 \right] \tag{3.13}$$

As previously stated, the SO coupling is time-reversal invariant but breaks sublattice symmetry. From the geometric perspective, all the rotations and reflection symmetries are preserved. While rotation invariance it's intuitive, Figure 3.2 seems to indicate a reflection symmetry breaking: all the arrows on the NNN hoppings are reversed by such transformations. However, one has to keep in mind that a reflection in the $x - y$ plane reverses the z component of the spin (the reader is encouraged to use a mirror to get convinced of this fact). In conclusion, a spin-flip together with the arrow inversion does not affect the SOC contribution. The presence of eventual curvature results in non-zero x and y components of the angular momentum. Contributions proportional to the gap-opening terms $\mathcal{M}_{133}$ and $\mathcal{M}_{233}$ appear in such a case.

We compare the SOC term $\mathcal{M}_{333}$ and the Haldane's mass $\mathcal{M}_{033}$, Section 3.1.2. Taking spin up or down separately, the SO coupling resembles Haldane's mass term and violates time-reversal symmetry. We, therefore, expect a similar emergence of a topological phase, with quantized transverse conductance and edge states. It has been proven this is the case [37]. However, the different gap signs for the two spin orientations result in currents with opposite directions $J_{\uparrow}$, $J_{\downarrow}$ for the two spins. The emerging total spin current $J_s = \frac{\hbar}{2e}\left(J_{\uparrow} - J_{\downarrow}\right)$ is distinct from the charge current deriving by the AHE of Haldane's model. While the latter is derived on each Hamiltonian sub-block ($H_{\uparrow}$, $H_{\downarrow}$), the former results from the interplay of the two sub-blocks. This study promoted the research of a new class of Hall effect, named "Quantum Spin Hall Effect".

3.1.4 Kekulé dimerization

We review a study by Claudio Chamon, who considered a specific variation of the hopping parameter resulting in a O-type Kekulé dimerization pattern (see Figure 3.3) [38–40]. Different lattice distortions have been considered, however, the gap-opening is not guaranteed. For example, it has been shown that Y-type Kekulé dimerization has gapless excitations [41].

The distortion of interest is obtained by adding to the Hamiltonian the following perturbation:

$$\delta H = \sum_{i \in A} \sum_{j} \delta t_{ij} \psi_{i}^{\dagger} \psi_{j} \tag{3.14}$$

where

$$\delta t_{ij} = \frac{\Delta}{3} e^{iK_D \cdot \delta_{ij}} e^{iG \cdot x_i} \tag{3.15}$$
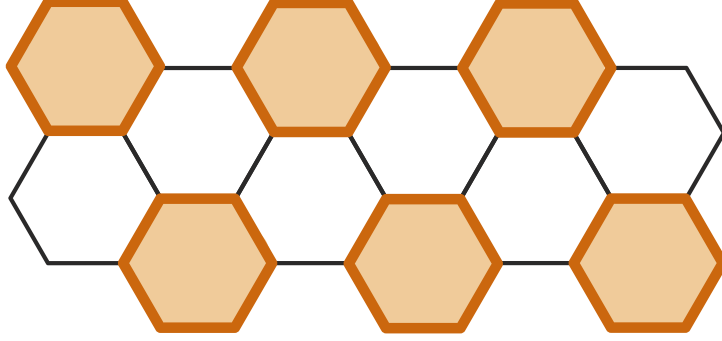
Figure 3.3: O-type Kekulé dimerization pattern on the honeycomb lattice. Orange lines indicate enhanced bonds.

The periodicity of the hopping parameter is given by the reciprocal of $G = K_D - K'_D$, and Δ is a complex number, which phase infers the dimerization pattern direction. By Fourier transformation, this equation becomes

$$
\begin{aligned}
\delta H &= \frac{\Delta}{3} \sum_{i \in A} \sum_{k,k'} a_k^\dagger b_{k'} e^{ix_i \cdot (k-k'+G)} \sum_j e^{i(k'+K_D)\cdot\delta_j} + h.c. \\
&= \frac{\Delta}{3} \sum_k a_k^\dagger b_{k+G} \sum_j e^{i(k+K_D+G)\cdot\delta_j} + h.c. \\
&= \frac{\Delta}{3} \sum_k \begin{pmatrix} a_k^\dagger \\ b_k^\dagger \end{pmatrix}^T \begin{pmatrix} 0 & \sum_j e^{i(k+K_D+G)\cdot\delta_j} \\ \sum_j e^{-i(k+K_D+G)\cdot\delta_j} & 0 \end{pmatrix} \begin{pmatrix} a_k \\ b_k \end{pmatrix}
\end{aligned}
\tag{3.16}
$$

A low-energy expansion around the Dirac point K'_D gives

$$
\begin{aligned}
\delta H &= \frac{\Delta}{3} \begin{pmatrix} a_{K_D}^\dagger \\ b_{K_D}^\dagger \end{pmatrix}^T \begin{pmatrix} 0 & \sum_j e^{i2K_D\cdot\delta_j} \\ \sum_j e^{-i2K_D\cdot\delta_j} & 0 \end{pmatrix} \begin{pmatrix} a_{K'_D} \\ b_{K'_D} \end{pmatrix} \\
&= \frac{\Delta}{3} \begin{pmatrix} a_{K_D}^\dagger \\ b_{K_D}^\dagger \end{pmatrix}^T \begin{pmatrix} 0 & \frac{3}{2} - i\frac{\sqrt{3}}{2} \\ \frac{3}{2} + i\frac{\sqrt{3}}{2} & 0 \end{pmatrix} \begin{pmatrix} a_{K'_D} \\ b_{K'_D} \end{pmatrix}
\end{aligned}
\tag{3.17}
$$

In fact, such perturbation mixes the two valleys. Including the spin degrees of freedom, and requiring the Hamiltonian to be hermitian, we see that

$$
\delta H = \frac{1}{2}\mathrm{Re}(\Delta)\mathcal{M}_{011} + \frac{1}{2}\mathrm{Im}(\Delta)\mathcal{M}_{021} + \frac{1}{2\sqrt{3}}\mathrm{Re}(\Delta)\mathcal{M}_{012} - \frac{1}{2\sqrt{3}}\mathrm{Im}(\Delta)\mathcal{M}_{022}
\tag{3.18}
$$

The first two terms open a gap at the Dirac points. Remarkably, $\mathcal{M}_{011}$ preserves all the considered symmetries, while $\mathcal{M}_{012}$ breaks some geometrical ones. Time reversal, charge and chiral symmetry are however preserved. Such gap-opening is one example of Dirac-cones merging: the two valleys are located at two equivalent points (i.e. related by a reciprocal lattice vector), the two cones are merged and the gap is open without symmetry breaking [42].

3.1.5 Spin-orbit coupling in Kekulé distorted graphene

When O-type Kekulé distortion is present, the reflection symmetry w.r.t. a NN bond is broken. The spin-orbit coupling in the NN hoppings becomes therefore relevant, with an amplitude strength λ_{ij} that has the same periodicity of the dimerization pattern (see Figure 3.3). This can be written in analogy to Equation 3.15

$$\lambda_{ij} = \pm \frac{\lambda}{3} e^{iK_D \cdot \delta_{ij}} e^{iG \cdot x_i} \tag{3.19}$$

where the $\pm$ stands for spins up/down in the z direction. Following the same derivation of the previous section, we get that

$$\delta H = \pm \frac{\lambda}{3} \begin{pmatrix} a_{K_D}^\dagger \\ b_{K_D}^\dagger \end{pmatrix}^T \begin{pmatrix} 0 & \frac{3}{2} - i\frac{\sqrt{3}}{2} \\ \frac{3}{2} + i\frac{\sqrt{3}}{2} & 0 \end{pmatrix} \begin{pmatrix} a_{K_D'} \\ b_{K_D'} \end{pmatrix} \tag{3.20}$$

which corresponds to

$$\delta H = \frac{1}{2}\mathrm{Re}(\lambda)\mathcal{M}_{311} + \frac{1}{2}\mathrm{Im}(\lambda)\mathcal{M}_{321} + \frac{1}{2\sqrt{3}}\mathrm{Re}(\lambda)\mathcal{M}_{312} - \frac{1}{2\sqrt{3}}\mathrm{Im}(\lambda)\mathcal{M}_{322} \tag{3.21}$$

Again, the first two terms open a gap at the Dirac points. Sublattice symmetry is preserved, and time reversal is broken by $\mathcal{M}_{321}$.
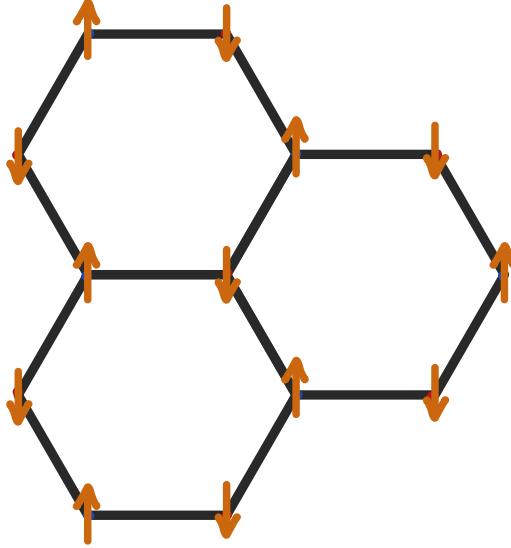
3.1.6 Anti-ferromagnetism

Figure 3.4: Antiferromagnetic pattern on graphene

The Heisenberg model is a well-established model for magnetism, which is based on the spin-spin interaction of localized particles [48]. The Hamiltonian takes the form

$$H = \frac{1}{2} \sum_{i,j} J_{ij} \mathbf{S}_i \cdot \mathbf{S}_j \tag{3.22}$$

where $\mathbf{S}_i = (S_i^x, S_i^y, S_i^z)$ is the spin degree of freedom sitting at the site i. We consider the specific case of interaction between nearest neighbours only, with uniform interaction strength.

$$H = \frac{J}{2} \sum_{\langle i,j \rangle} \mathbf{S}_i \cdot \mathbf{S}_j = \frac{J}{2} \left(S_i^z S_j^z + \frac{1}{2} S_i^+ S_j^- + \frac{1}{2} S_i^- S_j^+ \right) \tag{3.23}$$

Depending on the sign of J, the interaction is ferromagnetic ($J < 0$) or antiferromagnetic ($J > 0$). We focus on spin $1/2$ systems, where the Hamiltonian takes the following field theory form:

$$H = \frac{J}{8} \sum_{\langle i,j \rangle} \sum_\nu = \psi_{i\alpha}^\dagger s_{\alpha\beta}^\nu \psi_{i\beta} \; \psi_{j\gamma}^\dagger s_{\gamma\delta}^\nu \psi_{j\delta} \tag{3.24}$$

here s^ν is the ν-th Pauli matrix. The interaction is quartic in the fields. We thus make some approximations to include it in our picture, where all terms are quadratic in the fields.

Mean field approximation   We consider the expansion of the spin around its expectation value, and we neglect the second-order terms in the fluctuations (mean field approximation:

$$\mathbf{S}_i = \langle \mathbf{S}_i \rangle + \delta \mathbf{S}_i = \langle \mathbf{S}_i \rangle + (\mathbf{S}_i - \langle \mathbf{S}_i \rangle) \tag{3.25}$$

$$H = \frac{J}{2} \sum_{\langle i,j \rangle} \mathbf{S}_i \cdot \mathbf{S}_j \approx \frac{J}{2} \sum_{\langle i,j \rangle} \left(\langle \mathbf{S}_i \rangle \langle \mathbf{S}_j \rangle + \mathbf{S}_i \langle \mathbf{S}_j \rangle + \mathbf{S}_j \langle \mathbf{S}_i \rangle - \langle \mathbf{S}_i \rangle \langle \mathbf{S}_j \rangle \right)$$

$$= J \sum_{\langle i,j \rangle} \mathbf{S}_i \langle \mathbf{S}_j \rangle \tag{3.26}$$

Note that this approximation corresponds to the diagonal part $U_{x,x,y,y}$ of the Hartree approximation[1]. In Hamiltonian Equation 3.24, the MF treatment Equation 3.26 takes the form:

$$H_{MF} = J \sum_{\langle i,j \rangle} \sum_{\sigma,\sigma'} U_{\sigma,\sigma'} \psi_{i\sigma}^\dagger \psi_{j\sigma'}^\dagger \psi_{j\sigma'} \psi_{i\sigma}$$

$$\approx \frac{J}{4} \sum_{\langle i,j \rangle} \sum_\nu \sum_{\sigma,\sigma'} s_{\sigma,\sigma}^\nu s_{\sigma',\sigma'}^\nu \psi_{i\sigma}^\dagger \psi_{i\sigma} \left\langle \psi_{j\sigma'}^\dagger \psi_{j\sigma'} \right\rangle$$

$$= \frac{J}{4} \sum_{\langle i,j \rangle} \left[\psi_{i\uparrow}^\dagger \psi_{i\uparrow} \left\langle \psi_{j\uparrow}^\dagger \psi_{j\uparrow} \right\rangle + \psi_{i\downarrow}^\dagger \psi_{i\downarrow} \left\langle \psi_{j\downarrow}^\dagger \psi_{j\downarrow} \right\rangle - \psi_{i\uparrow}^\dagger \psi_{i\uparrow} \left\langle \psi_{j\downarrow}^\dagger \psi_{j\downarrow} \right\rangle - \psi_{i\downarrow}^\dagger \psi_{i\downarrow} \left\langle \psi_{j\uparrow}^\dagger \psi_{j\uparrow} \right\rangle \right]$$

$$= \frac{J}{2} \sum_{\langle i,j \rangle} \begin{pmatrix} \psi_{i\uparrow}^\dagger & \psi_{i\downarrow}^\dagger \end{pmatrix} \begin{pmatrix} m_j & 0 \\ 0 & -m_j \end{pmatrix} \begin{pmatrix} \psi_{i\uparrow} \\ \psi_{i\downarrow} \end{pmatrix}$$

$$\tag{3.28}$$

where $m_j = \frac{1}{2} \left\langle \psi_{i\uparrow}^\dagger \psi_{i\uparrow} - \psi_{i\downarrow}^\dagger \psi_{i\downarrow} \right\rangle$ is the expectation value of the magnetization at the site j. Our approximation neglects any exchange term, both in the lattice sites (i,j) and in the spin $(\uparrow,\downarrow)$.

---

[1]The Hartree - or direct - approximation has the general form:

$$\sum_{x,x',y,y'} U_{x,x',y,y'} \; \psi_x^\dagger \psi_y^\dagger \psi_{y'} \psi_{x'} \approx \frac{1}{2} \sum_{x,x',y,y'} U_{x,x',y,y'} \; \psi_x^\dagger \psi_{x'} \left\langle \psi_y^\dagger \psi_{y'} \right\rangle \tag{3.27}$$

where the lower index (x) represents any collection of quantum numbers.

Graphene is made of two identical sublattices, labelled A and B. Equation 3.28 becomes

$$H_{MF} = \frac{J}{4}\sum_{\langle i,j\rangle}\left[a_{i\uparrow}^\dagger a_{i\uparrow}\left\langle b_{j\uparrow}^\dagger b_{j\uparrow}\right\rangle + a_{i\downarrow}^\dagger a_{i\downarrow}\left\langle b_{j\downarrow}^\dagger b_{j\downarrow}\right\rangle - a_{i\uparrow}^\dagger a_{i\uparrow}\left\langle b_{j\downarrow}^\dagger b_{j\downarrow}\right\rangle - a_{i\downarrow}^\dagger a_{i\downarrow}\left\langle b_{j\uparrow}^\dagger b_{j\uparrow}\right\rangle + \boxed{a\leftrightarrow b}\right]$$

$$= \frac{J}{2}\sum_{\langle i,j\rangle}\left[\begin{pmatrix}a_{i\uparrow}^\dagger & a_{i\downarrow}^\dagger\end{pmatrix}\begin{pmatrix}m_j^B & 0 \\ 0 & -m_j^B\end{pmatrix}\begin{pmatrix}a_{i\uparrow} \\ a_{i\downarrow}\end{pmatrix} + \boxed{a\leftrightarrow b}\right]$$

$$(3.29)$$

where the operator a_i (b_i) is the field operator on the sublattice A (B). The goal now is to make the magnetization expectation values on the two sublattices, using geometrical arguments. The honeycomb lattice is a good candidate for antiferromagnetic ordering since it's free from frustration. One can in fact draw an antiferromagnetic ground state in which all the spins are pointing up on one sublattice and down on the other. This ground state is unique up to an overall spin rotation. Under this consideration, we assume the following:

- The expected magnetization values m_j^A, m_j^B are independent of the site j

- m^A and m^B differ only from a sign: $m^A = -m^B = m$

Making use of these results and translational symmetry we can transform the Hamiltonian in Fourier space. The resulting expression for the Hartree Hamiltonian is:

$$H_{MF} = \frac{J}{4}\sum_k\left[\begin{pmatrix}a_{k\uparrow}^\dagger & a_{k\downarrow}^\dagger\end{pmatrix}\begin{pmatrix}m & 0 \\ 0 & -m\end{pmatrix}\begin{pmatrix}a_{k\uparrow} \\ a_{k\downarrow}\end{pmatrix} - \boxed{a\leftrightarrow b}\right]$$

$$= \frac{Jm}{4}\sum_k\begin{pmatrix}a_{k\uparrow}^\dagger & b_{k\uparrow}^\dagger & a_{k\downarrow}^\dagger & b_{k\downarrow}^\dagger\end{pmatrix}s_3\otimes\tau_3\begin{pmatrix}a_{k\uparrow} \\ b_{k\uparrow} \\ a_{k\downarrow} \\ b_{k\downarrow}\end{pmatrix}$$

$$(3.30)$$

where s_i, and τ_i are the i-th Pauli matrices in spin and sublattice spaces respectively. Expanding the Hamiltonian around two inequivalent Dirac points K_D, K_D' we obtain a low-energy theory with an additional degree of freedom (valley). Since the Hamiltonian is independent of k, we obtain

$$H_{MF} = \frac{Jm}{4}s_3\otimes\sigma_0\otimes\tau_3 \qquad (3.31)$$

where the i-th Pauli matrix σ_i acts on the valley space ($\pm$), and the full field operator is given by Equation 1.15 In conclusion, the direct contribution corresponds to $\mathcal{M}_{303}$ which opens a gap at the Dirac points. A similar derivation has been previously conducted by Yazyev [47]. Moreover, it has been indicated that antiferromagnetic interaction might emerge from Coulomb interaction [47]. We postpone investigations about spontaneous generation to the next section. It's important to stress that the full Hamiltonian Eq.3.23 is time-reversal symmetric, but a generic mean-field approximation is not. In particular, the ground state of the full Hamiltonian (the saddle point of the mean-field expansion) represents a spontaneous symmetry-breaking. This argument indicates why $\mathcal{M}_{303}$ breaks both time-reversal $\mathcal{T}$ and sublattice (chiral) $\mathcal{S}$ symmetry. Consistently, however, the product of the two $\mathcal{C} = \mathcal{T}\mathcal{S}$ (charge symmetry) is preserved. Its action indeed consists of the exchange of the two sublattices and a spin-flip, which brings to the initial configuration.

3.2 Kagome masses and their symmetries

Although honeycomb and kagome lattices share several properties, their gap terms are generally hard to be related. Kagome lattice indeed is made of three sublattices, and the low-energy fields Eq.1.28 are delocalized on such sublattices: the new variables giving rise to a Dirac Hamiltonian are obtained through a linear combination of the original, site-related fields. We make use of unitary transformation to represent these terms in real space and symmetry arguments to map each mass term into a physical phenomenon. On other occasions instead, we derive a matrix form from first-principle calculations.

Interestingly, not all gap-opening terms in graphene open a gap in kagome, and viceversa. One simple example is given by a staggered potential on the three sublattices (μ_a, μ_b, μ_c), which corresponds to a linear combination of $\mathcal{M}_{000}$, $\mathcal{M}_{001}$ and $\mathcal{M}_{003}$ in the low-energy subspace. None of these mass terms results in a semimetal-insulator phase transition. Kagome gap terms are off-diagonal in the sublattice space, either in the valleys.

3.2.1 Haldane's model on kagome lattice
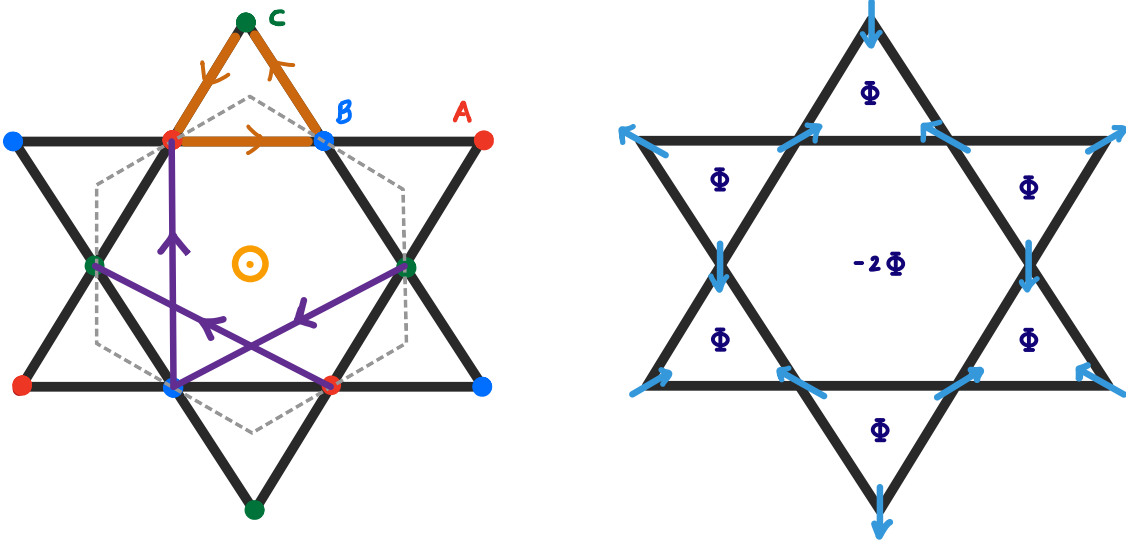
Figure 3.5: **(a)** Kagome unit cell, with nearest neighbour (NN, orange) and second-nearest neighbour (SNN, purple) bonds. Arrows mark the direction of positive phase hopping when Haldane's periodic magnetic field is present. A dotted, grey line encloses a surface of vanishing magnetic flux. **(b)** Magnetic fluxes through the triangles and the hexagons and the spin-chiral arrangement on the kagome lattice background. When electron spins are perfectly aligned to the nuclei spins (strong Hund's coupling), this chiral background order acts effectively as Haldane's magnetic field.

In this section, we consider the effect of a magnetic field $\mathbf{B}(\mathbf{r}) = B(\mathbf{r})\mathbf{z}$ perpendicular to the 2D plane, with zero flux through the unit cell. Following the path of Haldane's work[36], we consider a magnetic field with the periodicity of the lattice. This configuration can for instance be obtained by placing magnetic dipoles at the centre of each hexagon[50]. Using Peierls substitutions we absorb the effect of the magnetic field in the hopping amplitude t, which acquires a complex phase: $t \to te^{i\pm\theta}$. Differently from graphene, θ is finite since kagome geometry results in a finite flux of

B through NN hoppings closed paths. Defining Φ as the flux of the magnetic field through the triangles we compute the phase considering an anti-clockwise path, and by using Stokes theorem:

$$3\theta = -\frac{e}{\hbar} \oint_{\partial \triangle} \mathbf{A}(\mathbf{r}) \cdot d\mathbf{r} = -\frac{e}{\hbar} \int_{\triangle} \mathbf{B}(\mathbf{r}) \cdot d^2\mathbf{s} \qquad \rightarrow \qquad \theta = \frac{e}{3\hbar}\Phi \tag{3.32}$$

The sign of the acquired phase depends on the path direction, as shown in Figure 3.5: hoppings as $A \rightarrow B$, $B \rightarrow C$, $C \rightarrow A$ will gain a phase $+\theta$, while a phase $-\theta$ is obtained for opposite hoppings.

The TB Hamiltonian between nearest neighbours becomes

$$H_\theta = t \sum_{i \in A} e^{-i\theta} \left[a_i^\dagger b_{i \pm \delta_{ab}} + b_{i+\delta_{ab}}^\dagger c_{i \pm \delta_{ac}} + 5c_{i \pm \delta_{ac}}^\dagger a_i \right] + h.c. \tag{3.33}$$

After Fourier transform, we obtain

$$H_\theta = 2t \sum_k e^{-i\theta} \left[\cos\left(k \cdot \delta_{ab}\right) a_k^\dagger b_k + \cos\left(k \cdot \delta_{bc}\right) b_k^\dagger c_k + \cos\left(k \cdot \delta_{ac}\right) c_k^\dagger a_k \right] + h.c. \tag{3.34}$$

$$= 2t \sum_k \begin{pmatrix} a_k^\dagger \\ b_k^\dagger \\ c_k^\dagger \end{pmatrix}^T \begin{pmatrix} 0 & e^{-i\theta}\cos\left(k \cdot \delta_{ab}\right) & e^{i\theta}\cos\left(k \cdot \delta_{ac}\right) \\ e^{i\theta}\cos\left(k \cdot \delta_{ab}\right) & 0 & e^{-i\theta}\cos\left(k \cdot \delta_{bc}\right) \\ e^{-i\theta}\cos\left(k \cdot \delta_{ac}\right) & e^{i\theta}\cos\left(k \cdot \delta_{bc}\right) & 0 \end{pmatrix} \begin{pmatrix} a_k \\ b_k \\ c_k \end{pmatrix} \tag{3.35}$$

We consider a low-energy approximation evaluating this Hamiltonian at the two Dirac points $K_{D1,4}$, where

$$\cos\left(K_{D1} \cdot \delta_{ab}\right) = -1/2 \qquad\qquad \cos\left(K_{D1} \cdot \delta_{ac}\right) = \cos\left(K_{D1} \cdot \delta_{bc}\right) = 1/2$$
$$\cos\left(K_{D4} \cdot \delta_{ij}\right) = \cos\left(K_{D1} \cdot \delta_{ij}\right)$$

Including spin and valley degree of freedom the low-energy Hamiltonian becomes

$$H_\theta = t\cos\theta \left[s_0 \otimes \sigma_0 \otimes \begin{pmatrix} 0 & -1 & 1 \\ -1 & 0 & 1 \\ 1 & 1 & 0 \end{pmatrix} \right] + $$
$$- t\sin\theta \left[s_0 \otimes \sigma_0 \otimes \begin{pmatrix} 0 & -i & -i \\ i & 0 & i \\ i & -i & 0 \end{pmatrix} \right] \tag{3.36}$$

The first term is equal to the TB Hamiltonian in absence of magnetic field, multiplied by a factor $\cos\theta$. The second term instead corresponds to $\mathcal{M}_{002}$, which opens a gap at the Dirac points. The strength of this perturbation is $-t\sin\theta$. Since θ is proportional to the flux of $B(r)$, the Hamiltonian 3.36 reduces to the original TB form when $B(r) = 0$, and a gap of size $\Delta = \left| t\sqrt{3}\sin\theta \right|$ opens at the Dirac points when the magnetic field is switched on.

One can additionally include second-nearest neighbour hoppings (SNN), with amplitude t_2. Again, the hopping amplitude acquires a phase ϕ which sign depends on the direction of motion. The phase ϕ is different from θ, as one can show by considering the flux through the area surrounded by a closed path of SNN hoppings. In particular, we define Φ' as the flux through the triangle enclosed by one SNN bond, and two NN bonds. We have that

$$\phi = \frac{e}{\hbar}\Phi' + 2\theta \tag{3.37}$$

We define the vectors connecting second-nearest neighbours:

$$\alpha_{ab} = \left(0, \sqrt{3}\right) \qquad \alpha_{ac} = \frac{1}{2}\left(3, -\sqrt{3}\right) \qquad \alpha_{bc} = \frac{3}{2}\left(3, \sqrt{3}\right) \tag{3.38}$$

The derivation for such Hamiltonian is identical to the one shown above, after the substitution $t \to t_2$, $\delta_{ij} \to \alpha_{ij}$ and $\theta \to -\phi$. At the two Dirac points $K_{D1,4}$, we have

$$\cos\left(K_{D1} \cdot \alpha_{ij}\right) = \cos\left(K_{D4} \cdot \alpha_{ij}\right) = -1/2 \qquad \forall i \neq j \in \{a,b,c\}$$

Including spin and valley degree of freedom the low-energy Hamiltonian is

$$H_\phi = -t_2 \left[s_0 \otimes \sigma_0 \otimes \begin{pmatrix} 0 & e^{i\phi} & e^{-i\phi} \\ e^{-i\phi} & 0 & e^{i\phi} \\ e^{i\phi} & e^{-i\phi} & 0 \end{pmatrix} \right] \tag{3.39}$$

The imaginary part of Hamiltonian 3.39 corresponds to $\mathcal{M}_{002}$, with a proportionality factor of $-t_2 \sin\phi$. Since θ and ϕ have the same sign, one can easily see that SNN hoppings enforce our previous conclusion, resulting in a larger gap at the Dirac points: $\Delta = \left| t\sqrt{3}\sin\theta + \frac{t_2}{\sqrt{3}}\sin\phi \right|$ As in the graphene case, the Haldane's mass term breaks time-reversal and chiral symmetry, keeping intact charge symmetry. From a geometrical perspective, all the reflections are broken, while all the rotations are preserved, as one can check from Figure 3.5.

Hund's coupling and spin chirality In a previous section, we pointed out the relation between Haldane's model and the anomalous Hall effect (AHE). So far, we considered the emergence of Haldane's mass by artificially applying an external, well-tuned magnetic field. The AHE however has been experimentally observed in different materials, promoting several studies to address the origin of such effect [51]. One prominent explanation relates the AEH to the interplay between conducting electrons and a non-trivial magnetic background [53, 54]. In particular, conducting electrons strongly coupled to the nuclei spins (Hund's coupling) acquire a Berry phase if their spin is twisted to align to the background spins: a configuration of tilted spins in the underlying structure acts as an effective magnetic field [52]. Such structures are obtained, for example, in frustrated ferromagnets [54]. Kagome lattice promotes one interesting spin configuration, with pattern of alternating spin-chirality [55], represented in Figure 3.5. The effective magnetic field resulting from this background configuration is identical to the magnetic field of Haldane's model and is responsible for the same[2] gap-opening in the spectrum. It is shown that such interaction is responsible for the anomalous quantum Hall effect, as described in Section 3.1.2 for graphene.

3.2.2 Spin-orbit coupling and the topological insulator

Differently from graphene, intrinsic spin-orbit coupling (SOC) in kagome becomes relevant for nearest-neighbour hoppings too. The symmetry argument used in Section 3.1.3] is no longer valid here: a NN hop is associated with a SO coupling with amplitude $\pm i\lambda$, which sign depends on the spin and hopping direction, as shown in Figure 3.5. Guo and Franz [57] explored a similar interaction, considering instead hoppings between next-nearest neighbors. We expect however the SOC in NN hops to carry a more significant contribution. The SOC Hamiltonian is given by

$$H_{soc} = \pm i\frac{\lambda}{2} \sum_{\langle i,j \rangle} \psi_{i\alpha}^\dagger \psi_{j\beta} \left(s_3\right)_{\alpha\beta} = \pm i\frac{\lambda}{2} \sum_{\langle i,j \rangle} \left(\psi_{i\uparrow}^\dagger \psi_{j\uparrow} - \psi_{i\downarrow}^\dagger \psi_{j\downarrow} \right) \tag{3.40}$$

---

[2]In this last work, an infinite Hund's coupling is considered. The electron spin is always aligned to the background, and its variations when the site is changed are entirely absorbed into the Berry phase. The electrons become therefore fully fledged spinless.

where the $\pm$ is related to the hopping direction pictured in Figure 3.5, and s_3 is the z Pauli matrix in spin space. The explicit form in terms of the sublattice fields is

$$H_{soc} = i\frac{\lambda}{2} \sum_{x_i \in A} \left(a_{i,\uparrow}^{\dagger} b_{i\pm\delta_{ab},\uparrow} + b_{i+\delta_{ab},\uparrow}^{\dagger} c_{i\pm\delta_{ac},\uparrow} + c_{i\pm\delta_{ac},\uparrow}^{\dagger} a_{i,\uparrow} - \boxed{\uparrow \leftrightarrow \downarrow} \right) + h.c. \tag{3.41}$$

After Fourier transform, this reads

$$H_{soc} = i\lambda \sum_{k} \Phi_k^{\dagger} \left[s_3 \otimes \begin{pmatrix} 0 & \cos\left(k \cdot \delta_{ab}\right) & -\cos\left(k \cdot \delta_{ac}\right) \\ -\cos\left(k \cdot \delta_{ab}\right) & 0 & \cos\left(k \cdot \delta_{bc}\right) \\ \cos\left(k \cdot \delta_{ac}\right) & -\cos\left(k \cdot \delta_{bc}\right) & 0 \end{pmatrix} \right] \Phi_k \tag{3.42}$$

where $\Phi_k = \begin{pmatrix} a_{k\uparrow} & b_{k\uparrow} & c_{k\uparrow} & a_{k\downarrow} & b_{k\downarrow} & c_{k\downarrow} \end{pmatrix}^T$. Expanding around the Dirac points one gets

$$H_{soc} = i\frac{\lambda}{2} s_3 \otimes \sigma_0 \otimes \begin{pmatrix} 0 & -1 & -1 \\ 1 & 0 & 1 \\ 1 & -1 & 0 \end{pmatrix} \tag{3.43}$$

which corresponds to the gap-opening term $\mathcal{M}_{302}$. SO coupling for second-nearest neighbours hopping corresponds to the same mass term [57], with a different SOC amplitude λ', which enlarges the gap. As one would expect from spin-orbit coupling, time-reversibility is ensured. In addition, all reflections and rotations are preserved. No x or y spin couplings are present in the case of planar kagome lattice, because of the $\hat{z} \to -\hat{z}$ reflection symmetry. If curvature is present, however, the angular momentum vector acquires non-zero components in the x and y directions, resulting in additional terms $\mathcal{M}_{102}$ and $\mathcal{M}_{202}$. Such couplings enjoy time-reversal symmetry but break certain lattice symmetries which were preserved in the planar case. Guo and Franz demonstrated the presence of edge gapless states in the SO phase, which characterize it as a topological insulator [57].

3.2.3 (Resonating) Plaquette ordered phases
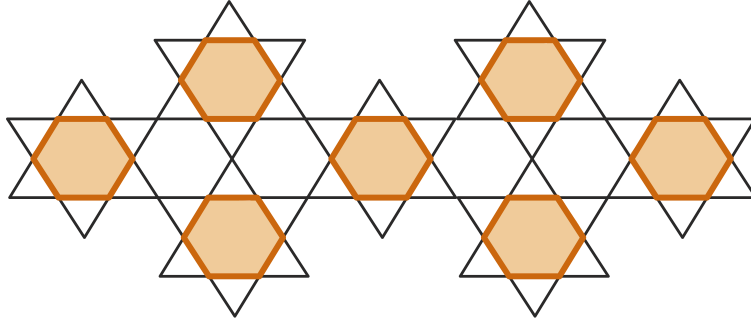
Figure 3.6: O-type Kekulé dimerization pattern on kagome lattice, also referred as plaquette ordered phase.

Within the list of gap terms, the only off-diagonal in the valleys are instead diagonal in sublattice space. Such terms live on the lattice sites, rather than on the bonds. In this section, we address two families of mass terms which have the peculiarity to be off-diagonal in valley space.

The first family is composed by $\mathcal{M}_{010}$ and $\mathcal{M}_{020}$, which are spin-independent. In the previous section, we derived valley-mixing terms from O-type Kekulé distortion of the lattice. Although in this case, hopping amplitude anisotropy due to such distortion is not responsible for gap-opening.

However, when the coupling within the rings is strong, the emerging charge order results in a mean-field, on-site potential of the form:

$$V(r) = \text{Re}\,(\xi)\cos\,(r \cdot G) + \text{Im}(\xi)\sin\,(r \cdot G) \tag{3.44}$$

which is Fourier transformed into

$$
\delta H = \frac{\text{Re}(\xi)}{2}\sum_k \left[a_k^\dagger a_{k-G} + a_k^\dagger a_{k+G}\right] + \frac{\text{Im}(\xi)}{2i}\sum_k \left[a_k^\dagger a_{k-G} - a_k^\dagger a_{k+G}\right] + \\
+ \boxed{a \leftrightarrow b} + \boxed{a \leftrightarrow c} \tag{3.45}
$$

This term takes the desired form at the Dirac points, and a gap is open. All the quantum symmetries (time-reversal, charge, chiral symmetry) are preserved. The valley mixing results indeed in merging the two Dirac points [42], as discussed in the previous section for Kekulé dimerization of graphene.

The second family resembles the first while showing an additional spin dependence: $\mathcal{M}_{j10}$ and $\mathcal{M}_{j20}$ are its members, where $j = 1, 2, 3$. These terms break time reversal and charge while preserving chiral symmetry. We present two fascinating phases of strongly interacting electrons on kagome lattice, explored by Pollmann et al. [59], which give rise to these terms in a mean-field treatment. In second quantization language, Coulomb interaction can be approximated in the extended Hubbard model, which takes into account on-site and NN repulsions. The Hamiltonian is given by

$$
\begin{aligned}
H &= -t\sum_{\sigma,\sigma'}\sum_{\langle ij\rangle}\psi_{i\sigma}^\dagger \psi_{j\sigma'} + U\sum_i \psi_{i\uparrow}^\dagger \psi_{i\uparrow}\psi_{i\downarrow}^\dagger \psi_{i\downarrow} + V\sum_{\sigma,\sigma'}\sum_{\langle ij\rangle}\psi_{i\sigma}^\dagger \psi_{i\sigma}\psi_{j\sigma'}^\dagger \psi_{j\sigma'} \\
&= -t\sum_{\sigma,\sigma'}\sum_{\langle ij\rangle}\psi_{i\sigma}^\dagger \psi_{j\sigma'} + U\sum_i n_{i\uparrow}n_{i\downarrow} + V\sum_{\sigma,\sigma'}\sum_{\langle ij\rangle}n_{i\sigma}n_{j\sigma'}
\end{aligned}
\tag{3.46}
$$

In the strong coupling limit, where $0 < t \ll V < U$ two main contributions approximate the Hamiltonian. The first is a ring-exchange term of three electrons occupying non-NN sites on hexagons, and it describes charge fluctuations. The amplitude of such interaction is given by $g = \frac{6t^3}{V^2}$. The second contribution describes a spin-exchange term, and takes the form of a NN Heisenberg interaction with amplitude $J = \frac{2t^2}{U-V} + \frac{2t^3}{V^2}$:

$$H_s = \sum_{\langle ij\rangle}\left[S_i \cdot S_j - \frac{1}{2}n_i n_j\right] \tag{3.47}$$

Two observations are in order. Firstly, we notice that the two amplitudes are independent. Secondly, taking the two contributions separately results in two distinct ground states. When spin fluctuations dominate over charge fluctuations, the lowest energy is reached when electrons form loops with shorter possible length [59]. This corresponds to the so-called "short loop phase", sketched in figure 3.6. Spin ordering within the hexagonal loop depends on the sign of J: for $t > 0$ antiferromagnetic ordering appears, while both ferromagnetic and antiferromagnetic exchanges are possible for $t < 0$. Such phase resembles a O-type Kekulé dimerization pattern with spin dependence, and periodicity given by a wave vector $G = K_{D1} - K_{D4}$, which results in a valley mixing. When instead charge fluctuations dominate, electrons are disposed as sketched in Figure 3.7: three electrons resonating on the hexagons are surrounded by three localised ones. Spin exchange lifts the ground state degeneracy favouring the depicted antiferromagnetic pattern. A mean-field treatment of such interactions results in the desired terms, with freedom in the choice of spin direction.
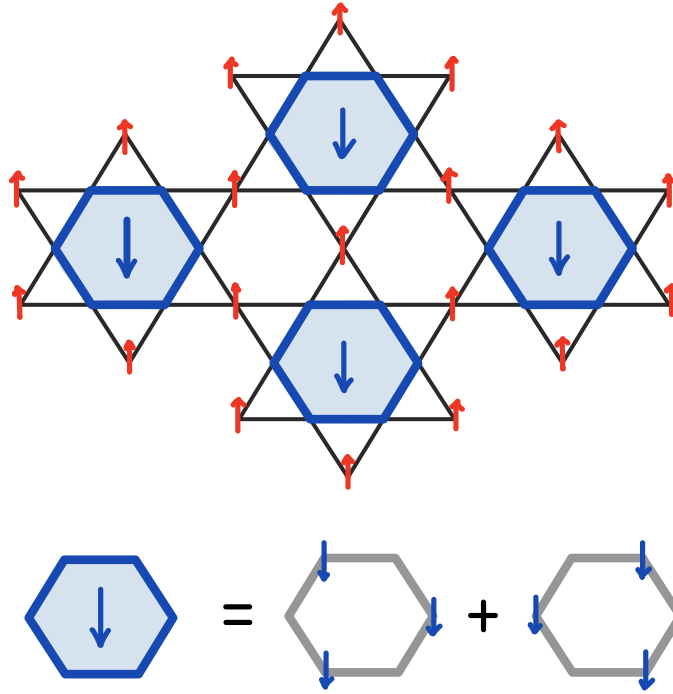
Figure 3.7: Kagome lattice at 1/3 filling of strongly interacting electrons is in a resonating plaquette phase [59]. An antiferromagnetic perturbation lifts the spin-degeneracy of the ground state, favouring a magnetic ordering: three resonating, parallel spins form a 3/2 spin on the hexagon, surrounded by localised spins pointing in the opposite direction.
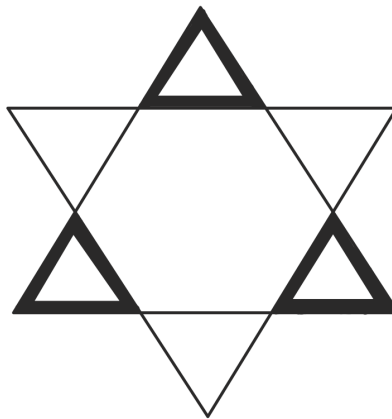
Figure 3.8: Trimerization pattern of the kagome lattice. Thick (thin) lines depict stronger (weaker) bonds.

3.2.4 Dimerization and trimerization

We consider a trimerized phase[61], represented in Figure 3.8. Such structure is given by bonds with alternating values of hopping amplitude $t \to t \pm \eta$, and it is often named "breathing kagome" phase. After Fourier transform, the Hamiltonian becomes

$$H_{tr} = H_{TB} + 2\eta i \sum_k \begin{pmatrix} a_k^\dagger \\ b_k^\dagger \\ c_k^\dagger \end{pmatrix}^T \begin{pmatrix} 0 & \sin(k \cdot \delta_{ab}) & \sin(k \cdot \delta_{ac}) \\ -\sin(k \cdot \delta_{ab}) & 0 & \sin(k \cdot \delta_{bc}) \\ -\sin(k \cdot \delta_{ac}) & -\sin(k \cdot \delta_{bc}) & 0 \end{pmatrix} \begin{pmatrix} a_k \\ b_k \\ c_k \end{pmatrix} \tag{3.48}$$

A second term is added to the original TB Hamiltonian, which can be expanded around Dirac points, obtaining:

$$H_\eta = 2\eta i \left[s_0 \otimes \sigma_3 \otimes \begin{pmatrix} 0 & 1 & 1 \\ -1 & 0 & -1 \\ -1 & 1 & 0 \end{pmatrix} \right] \tag{3.49}$$

where the spin and valley degrees of freedom have been included. This Hamiltonian corresponds to the gap-opening term $\mathcal{M}_{032}$, which breaks sublattice symmetry while keeping time-reversal intact.

We consider in addition a more generic case of lattice distortion, in which we allow the hopping amplitude variation to be orientation-dependent. In particular we consider $\eta = (\eta_{ab}, \eta_{ac}, \eta_{bc})$. In such case the additional Hamiltonian becomes

$$H_\eta = 2i \left[s_0 \otimes \sigma_3 \otimes \begin{pmatrix} 0 & \eta_{ab} & \eta_{ac} \\ -\eta_{ab} & 0 & -\eta_{bc} \\ -\eta_{ac} & \eta_{bc} & 0 \end{pmatrix} \right] \tag{3.50}$$

This Hamiltonian corresponds to the same gap terms $\mathcal{M}_{032}$, given that $\eta \neq (0,0,0)$. We conclude that dimerization patterns (obtained with one non-zero component of η) open a gap too. In the next section, we will address the spontaneous emergence of dimerization patterns from Coulomb interactions, explored in a recent work [61].

3.2.5 Spin-orbit coupling in trimerized kagome lattice
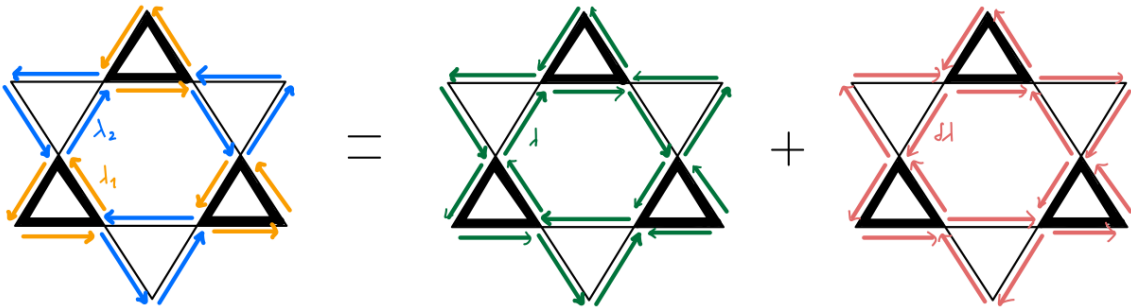
Figure 3.9: Spin-orbit coupling in the trimerized phase (breathing anisotropy), where thick (thin) lines represent strong (weak) bonds. Arrows mark the direction of positive amplitudes hopping $+\lambda_{1,2}$ for a spin-up. Down spins have reversed arrows. The alternating amplitude pattern $\lambda_{1,2}$ can be decoupled into a regular SOC arrow pattern and a contribution of the anisotropy (first and second term on the RHS respectively).

We investigate how the trimerization pattern named "breathing kagome" affects spin-orbit coupling (SOC). Such anisotropy, characterised by stronger (weaker) bonds between up(down)-facing triangles, has been taken into account in the previous section. In that context we investigated the effect of this bonding pattern from the point of view of the hopping amplitude t, proving that a gap is open because of the $\mathcal{M}_{032}$ mass term appearing in the Hamiltonian. In this section, we look at how this ordering affects a spinful system with SOC.

Following the procedure of Section 3.2.2 we look at the SOC in this configuration: the anisotropy is translated in two different SOC amplitudes[62] $\pm\lambda_1$ and $\pm\lambda_2$, when they are associated to a stronger or weaker bond respectively [51]. Again, the sign of such amplitudes depends on the hopping direction and on the electron spin pointing up (or down). As shown in Figure 3.9, one can introduce the following hopping amplitudes:

$$\lambda = \frac{\lambda_1 + \lambda_2}{2} \qquad\qquad \delta\lambda = \frac{\lambda_1 - \lambda_2}{2} \tag{3.51}$$

With this transformation, one can decouple the spin-orbit interaction into a regular SOC pattern with strength given by the average of λ_1, λ_2 and a hopping pattern which takes into account the trimerization effects. The first contribution is equal to Equation 3.40, and therefore corresponds to the gap term $\mathcal{M}_{302}$. The second instead is substantially different, as we show below.

The anisotropy effects on the SOC can be expressed as

$$\delta H_{soc} = i\frac{\delta\lambda}{2} \sum_{x_i \in A} \left(a_{i,\uparrow}^\dagger b_{i+\delta_{ab},\uparrow} - a_{i,\uparrow}^\dagger b_{i-\delta_{ab},\uparrow} - \boxed{b \leftrightarrow c} - \boxed{a \leftrightarrow c} - \boxed{\uparrow \leftrightarrow \downarrow} \right) + h.c. \tag{3.52}$$

where we stress that for a fixed spin (up or down) the trimerization results in an alternating pattern of SOC strength. After Fourier transformation the Hamiltonian reads

$$\delta H_{soc} = i\delta\lambda \sum_k \Phi_k^\dagger \left[s_3 \otimes \begin{pmatrix} 0 & \sin\left(k\cdot\delta_{ab}\right) & -\sin\left(k\cdot\delta_{ac}\right) \\ -\sin\left(k\cdot\delta_{ab}\right) & 0 & \sin\left(k\cdot\delta_{bc}\right) \\ \sin\left(k\cdot\delta_{ac}\right) & -\sin\left(k\cdot\delta_{bc}\right) & 0 \end{pmatrix} \right] \Phi_k \tag{3.53}$$

This Hamiltonian is odd in k: the expansion around the two Dirac points results in opposite signs.

$$\delta H_{soc} = i\frac{\delta\lambda}{2} \, s_3 \otimes \sigma_3 \otimes \begin{pmatrix} 0 & 1 & -1 \\ -1 & 0 & -1 \\ 1 & 1 & 0 \end{pmatrix} \tag{3.54}$$

which corresponds to the gap-opening term $\mathcal{M}_{332}$. As one can see from Table 2.2 and Figure 3.9 (second contribution, pattern of arrows), such term is invariant under rotations of $\pm\frac{2\pi}{3}$ and under certain reflections. When the effect of trimerization is taken into account both for hopping amplitude and spin-orbit coupling ($\mathcal{M}_{032}$ and $\mathcal{M}_{332}$ respectively), all reflection symmetries are broken.

Again, a non-planar setup gives rise to x and y components in the spin-coupling, which correspond to the gap-opening terms $\mathcal{M}_{132}$ and $\mathcal{M}_{232}$.

3.3   Remarks

Tables 3.1, 3.2 resume the physical nature of the mass terms. We observe strong analogies between certain masses in the two lattices. Haldane's model [36] for instance, originally proposed on the honeycomb lattice, can be promoted in the kagome lattice with equivalent consequences: the gap is

opened, and a phase transition to a topological phase occurs. The related **anomalous quantum Hall effect** (AHE) can be extended on the kagome lattice with an interesting remark: in the latter, the effect becomes relevant already for nearest neighbour hoppings, while the original model on graphene needs to incorporate second-nearest sites. These same arguments are applicable to the spin-orbit coupling, and the related **quantum spin-Hall effect**. This phenomenon, in fact, proposed in first place on graphene by Kane and Mele [37], has been transposed on the kagome lattice by Guo and Franz [57]. The two cited studies consider second-nearest neighbours hopping. In this work, however, we show that nearest-neighbour hoppings are relevant for SOC in kagome lattice, and they possibly represent the leading contribution. This fact might indicate kagome materials as more promising candidates to observe such kind of topological phases, compared to graphene.

A different scenario regards instead **lattice deformations**. The simplest patterns which open a gap while keeping intact the size of the unit cell are substantially different in the two lattices. Semenoff showed in 1984 that a staggered potential, which takes different values on the two sublattices of graphene, drives the system to a trivial insulating phase. Such deformation has no direct match in the collection of kagome mass terms. In the latter, however, a dimerization pattern of bonds with alternating strengths takes its respective place. One interpretation of such difference can be given in the following terms. kagome lattice at 1/3 filling can be mapped into a dimer model on the honeycomb lattice [59]. Quantum states (along with bilinear terms) which are localised on the sites are mapped into states which live on the bonds, and viceversa. This can also be seen in more sophisticated distortions, as O-type **Kekulé patterns**. Such lattice modifications enlarge the unit cell and are described by a periodicity which mixes the two valleys in momentum space. In graphene the related hopping-amplitude distortion opens a gap at the Dirac points [38]. In kagome materials instead, the gap is opened by the effective on-site potential which has such periodicity. Again, a mass term living on the bonds of one lattice (graphene) is mapped into one living on the sites of the other lattice (kagome). It is reasonable to consider such masses as characteristics of different regimes. The Kekulé dimerization mass of graphene is finite at any small deviation of the hopping amplitude. Instead, the corresponding effective potential which opens a gap in kagome materials is a significant description only for strongly-dimerized configurations. A different way to see such discrepancy is to compare the weak and the strong coupling limits. In the former regime, the physics is dominated by hopping phenomena, and hopping amplitude distortions are relevant. In the latter limit instead, the hopping exchange is typically treated as a perturbation acting on a state of localised charges, and small hopping deviations are negligible compared to on-site potentials. A side note is in order here: the Kekulé pattern opens a gap in the two materials by merging the two independent Dirac points and preserving all the quantum symmetries. Contrarily, all the other masses break either time reversal, charge, or chiral symmetry[3].

One interesting comparison concerns **antiferromagnetic ordering**. Graphene is a good candidate for Néel ordering at 1/2 filling because composed of two sublattices, and therefore free of frustration. One can draw a spin pattern with a magnetic cell which corresponds to the lattice unit cell. A mean-field treatment of such ordering indicates a gapped and trivial insulating phase. While the kagome lattice at 1/2 filling frustrates antiferromagnetic ordering, there is some chance when the chemical potential is tuned at the Dirac points (1/3 filling). In specific, we explored the resonating plaquette phase, described by a mean-field, spin-dependent potential that mixes the two valleys. Such antiferromagnetic ordering opens a gap at the Dirac points, enlarging however the unit cell of three times.

---

[3]Such exceptional mechanism of Dirac points merging represents the unique way to open a gap in Weyl semimetals. For these reasons, the semimetallic phase is strongly protected in these last materials.

Honeycomb lattice (graphene)						
Idx ijk	Parity	T-rev	Char	Chiral	Instability	Section
{0,0,3}	✗	✓	✗	✗	Staggered potential	3.1.1
{0,1,1}	✓	✓	✓	✓	Kekulé dimerization	3.1.4
{0,2,1}	✗	✓	✓	✓	Kekulé dimerization	
{0,3,3}	✓	✗	✓	✗	Haldane's model	3.1.2
{1,0,3}	✗	✗	✓	✗	Anti-ferromagnet - x	3.1.6
{2,0,3}	✗	✗	✓	✗	Anti-ferromagnet - y	
{3,0,3}	✗	✗	✓	✗	Anti-ferromagnet - z	
{1,1,1}	✓	✗	✗	✓	SOC in Kekulé	3.1.5
{2,1,1}	✓	✗	✗	✓	SOC in Kekulé	
{3,1,1}	✓	✗	✗	✓	SOC in Kekulé	
{1,2,1}	✗	✗	✗	✓	SOC in Kekulé	
{2,2,1}	✗	✗	✗	✓	SOC in Kekulé	
{3,2,1}	✗	✗	✗	✓	SOC in Kekulé	
{1,3,3}	✓	✓	✗	✗	Spin-orbit coupling - x	3.1.3
{2,3,3}	✓	✓	✗	✗	Spin-orbit coupling - y	
{3,3,3}	✓	✓	✗	✗	Spin-orbit coupling - z	

Table 3.1: Graphene mass terms and their physical interpretation.

Kagome lattice						
Idx ijk	Parity	T-rev	Char	Chiral	Instability	Section
{0,0,2}	✓	✗	✓	✗	Haldane's model (spin-chiral)	3.2.1
{0,1,0}	✓	✓	✓	✓	Plaquette phase (rings)	3.2.3
{0,2,0}	✗	✓	✓	✓	Plaquette phase (rings)	3.2.3
{0,3,2}	✗	✓	✗	✗	Lattice dimerization & trimerization	3.2.4
{1,1,0}	✓	✗	✗	✓	Resonating plaquette phase - x	3.2.3
{2,1,0}	✓	✗	✗	✓	Resonating plaquette phase - y	
{3,1,0}	✓	✗	✗	✓	Resonating plaquette phase - z	
{1,2,0}	✗	✗	✗	✓	Resonating plaquette phase - x	
{2,2,0}	✗	✗	✗	✓	Resonating plaquette phase - y	
{3,2,0}	✗	✗	✗	✓	Resonating plaquette phase - z	
{1,0,2}	✓	✓	✗	✗	Spin-orbit coupling - x	3.2.2
{2,0,2}	✓	✓	✗	✗	Spin-orbit coupling - y	
{3,0,2}	✓	✓	✗	✗	Spin-orbit coupling - z	
{1,3,2}	✗	✗	✓	✗	SOC in trimerized latt. x	3.2.5
{2,3,2}	✗	✗	✓	✗	SOC in trimerized latt. y	
{3,3,2}	✗	✗	✓	✗	SOC in trimerized latt. z	

Table 3.2: Kagome mass terms and their physical interpretation.

Chapter 4

Spontaneous mass generation

So far, we managed to classify and identify all the mass terms, without addressing whether they spontaneously emerge. In the present section, we review different studies on spontaneous mass generation, which makes kagome materials and graphene two insulators. Specifically, we look at Coulomb repulsion between electrons as a possible source for some of the interactions studied above. In the first part, we derive antiferromagnetic interaction from the Hubbard model with simple perturbative arguments, and we report similar results previously obtained on the kagome lattice [59]. In the second part, we review one study which makes use of self-consistent, field theory calculation to measure the gap. In this last case, the phase transition is analyzed as a function of the interaction strength, making it possible to determine the potential occurrence in real materials.

4.1 Antiferromagnetism

4.1.1 From the Hubbard model to the Heisenberg interaction: a simple approach to antiferromagnetism

In this section, we derive the Heisenberg antiferromagnetic interaction from the Hubbard model using perturbative arguments, proposed by Cleveland in 1976 [63]. The Hubbard model mimics Coulomb interaction on a discrete lattice in the simplest approximation possible, i.e. when repulsion between electrons occurs only within each site. The Hubbard Hamiltonian is

$$H = -t \sum_{\sigma} \sum_{\langle i,j \rangle} c_{i\sigma}^{\dagger} c_{j\sigma} + U \sum_{i} n_{i\uparrow} n_{i\downarrow} \qquad (4.1)$$

where $n_{i\sigma} = c_{i\sigma}^{\dagger} c_{i\sigma}$ is the occupation number of electrons on the site i, with spin σ. We focus on the strong coupling limit, where $t \ll U$ and the hopping term (in the following named $\hat{T}$) is treated as a perturbation. At half-filling (when the number of electrons equals the number of lattice sites N) the ground state of the unperturbed Hamiltonian ($t = 0$) has exactly one electron for lattice site. The degeneracy of the ground state is 2^N, that is the number of possible spin arrangements one can obtain. The perturbation $\hat{T}$ however can lift this degeneracy.

In the following part, we consider just two neighbouring sites i and j, and we ignore any other lattice site; we expand our lattice landscape in the last part of the present section. The unperturbed ground state is four times degenerate, and it's represented by the states $|\uparrow \ \uparrow\rangle, |\uparrow \ \downarrow\rangle, |\downarrow \ \uparrow\rangle, |\downarrow \ \downarrow\rangle$, where the two spins sit at the two different sites i, j. The first-order energy correction is clearly

vanishing. We, therefore, focus on second-order terms. Because of the Pauli principle, electrons can hop only towards neighbours with opposite spin:

$$
\begin{aligned}
\hat{T}\,|\uparrow\ \ \uparrow\rangle &= \hat{T}\,|\downarrow\ \ \downarrow\rangle = 0 \\
\hat{T}\,|\uparrow\ \ \downarrow\rangle &= -t\left(|\quad\uparrow\downarrow\rangle - |\uparrow\downarrow\quad\rangle\right) \\
\hat{T}\,|\downarrow\ \ \uparrow\rangle &= +t\left(|\quad\downarrow\uparrow\rangle - |\downarrow\uparrow\quad\rangle\right)
\end{aligned}
\tag{4.2}
$$

The second-order corrections to the four degenerate states are

$$
\begin{aligned}
E_{\uparrow\uparrow}^{(2)} &= E_{\downarrow\downarrow}^{(2)} = 0 \\
E_{\uparrow\downarrow}^{(2)} &= -\frac{1}{U}\left|\langle\quad\downarrow\uparrow|\,\hat{T}\,|\uparrow\ \ \downarrow\rangle\right|^{2} - \frac{1}{U}\left|\langle\downarrow\uparrow\quad|\,\hat{T}\,|\uparrow\ \ \downarrow\rangle\right|^{2} = -\frac{2t^{2}}{U} \\
E_{\downarrow\uparrow}^{(2)} &= -\frac{1}{U}\left|\langle\quad\downarrow\uparrow|\,\hat{T}\,|\downarrow\ \ \uparrow\rangle\right|^{2} - \frac{1}{U}\left|\langle\downarrow\uparrow\quad|\,\hat{T}\,|\downarrow\ \ \uparrow\rangle\right|^{2} = -\frac{2t^{2}}{U}
\end{aligned}
\tag{4.3}
$$

We conclude that anti-aligned neighbouring spins are favoured by the $\hat{T}$ because they allow for hopping exchanges. We can rewrite the problem in a different manner. The relations for the second-order corrections to the ground-state energy is

$$
H = \langle g.s.|\,\hat{T}\sum_{n\neq 0}\frac{|n\rangle\langle n|}{E_{0}^{(0)} - E_{n}^{(0)}}\,\hat{T}\,|g.s.\rangle
\tag{4.4}
$$

The n-summation, which generally runs over the entire spectrum, can be restricted here to the first excited states since all the other matrix elements are automatically vanishing. Alternatively, one can keep the entire summation and substitute $-U$ to the energy difference (denominator). The case $n = 0$ is added to the summation since $\langle g.s.|\,\hat{T}\,|g.s.\rangle = 0$:

$$
H = -\frac{1}{U}\,\langle g.s.|\,\hat{T}\left(\sum_{n}|n\rangle\langle n|\right)\hat{T}\,|g.s.\rangle = -\frac{1}{U}\,\langle g.s.|\,\hat{T}^{2}\,|g.s.\rangle
\tag{4.5}
$$

The second-order correction to the energy corresponds indeed to the eigenvalues of $-\hat{T}^{2}/U$ in the ground-energy subspace. We can therefore write an effective Hamiltonian as this last operator, projected in the low-energy subspace: $H_{\mathrm{eff}} = P_{0}\left(-\hat{T}^{2}/U\right)P_{0}^{-1}$. Its matrix elements can be obtained from the following equations:

$$
\begin{aligned}
\hat{T}^{2}\,|\uparrow\ \ \uparrow\rangle &= \hat{T}^{2}\,|\downarrow\ \ \downarrow\rangle = 0 \\
\hat{T}^{2}\,|\uparrow\ \ \downarrow\rangle &= 2t^{2}\left(|\uparrow\ \ \downarrow\rangle - |\downarrow\ \ \uparrow\rangle\right) \\
\hat{T}^{2}\,|\downarrow\ \ \uparrow\rangle &= 2t^{2}\left(|\downarrow\ \ \uparrow\rangle - |\uparrow\ \ \downarrow\rangle\right)
\end{aligned}
$$

And then

$$
\begin{aligned}
V_{\mathrm{eff}} &= -\frac{1}{U}\sum_{n,n'\in g.s.}\left(\langle n|\,\hat{T}^{2}\,|n'\rangle\right)|n\rangle\langle n'| = \\
&= -\frac{2t^{2}}{U}\Big[\,|\uparrow\ \ \downarrow\rangle\langle\uparrow\ \ \downarrow| + |\uparrow\ \ \downarrow\rangle\langle\uparrow\ \ \downarrow| - |\uparrow\ \ \downarrow\rangle\langle\downarrow\ \ \uparrow| - |\downarrow\ \ \uparrow\rangle\langle\uparrow\ \ \downarrow|\,\Big]
\end{aligned}
\tag{4.6}
$$

We rewrite the effective Hamiltonian for the two neighbouring sites i, j in second quantization:

$$
\begin{aligned}
V_{\text{eff}} &= P_0 \left(-\hat{T}^2/U \right) P_0^{-1} = P_0 \left(-\frac{2t^2}{U} \sum_\sigma c_{i\sigma}^\dagger c_{j\sigma} \sum_\eta c_{j\eta}^\dagger c_{i\eta} \right) P_0^{-1} \\
&= -\frac{2t^2}{U} P_0 \sum_{\sigma\eta} c_{i\sigma}^\dagger c_{i\eta} \left(\delta_{\sigma\eta} - c_{j\eta}^\dagger c_{j\sigma} \right) P_0^{-1} \\
&= \frac{2t^2}{U} P_0 \sum_\sigma \left(c_{i\sigma}^\dagger c_{i\sigma} c_{j\sigma}^\dagger c_{j\sigma} + c_{i\sigma}^\dagger c_{i-\sigma} c_{j-\sigma}^\dagger c_{j\sigma} - c_{i\sigma}^\dagger c_{i\sigma} \right) P_0^{-1}
\end{aligned}
\tag{4.7}
$$

Now we use that

$$
\begin{aligned}
P_0 \left(S_i^z S_j^z \right) P_0^{-1} &= P_0 \left(1/4 \sum_{ab} \sigma_{aa}^z \sigma_{bb}^z c_{ia}^\dagger c_{ia} c_{jb}^\dagger c_{jb} \right) P_0^{-1} \\
&= P_0 \left(1/4 \sum_a c_{ia}^\dagger c_{ia} c_{ja}^\dagger c_{ja} - 1/4 \sum_{a \neq b} c_{ia}^\dagger c_{ia} c_{jb}^\dagger c_{jb} \right) P_0^{-1}
\end{aligned}
\tag{4.8}
$$

and that the second term is proportional to the identity in the ground-state subspace:

$$
P_0 \left(\sum_{a \neq b} c_{ia}^\dagger c_{ia} c_{jb}^\dagger c_{jb} \right) P_0^{-1} = P_0 \, \mathbb{1} \, P_0^{-1}
\tag{4.9}
$$

We conclude that the first term in equation 4.7 is

$$
P_0 \left(\sum_a c_{ia}^\dagger c_{ia} c_{ja}^\dagger c_{ja} \right) P_0^{-1} = P_0 \left(4 S_1^z S_2^z + \mathbb{1} \right) P_0^{-1}
\tag{4.10}
$$

The second term in Eq. 4.7 correspond to ladder operators:

$$
\sum_\sigma c_{i\sigma}^\dagger c_{i-\sigma} c_{j-\sigma}^\dagger c_{j\sigma} = S_i^+ S_j^- + S_i^- S_j^+
\tag{4.11}
$$

Using that $\sum_\sigma c_{i\sigma}^\dagger c_{i\sigma} = 1$ at half filling (third term in Eq. 4.7), the effective Hamiltonian becomes

$$
V_{\text{eff}} = \frac{2t^2}{U} P_0 \left(2 S_i^z S_j^z + S_i^+ S_j^- + S_i^- S_j^+ - 1/2 \right) P_0^{-1} = \frac{2t^2}{U} P_0 \left(\vec{S}_i \cdot \vec{S}_j - 1/2 \right) P_0^{-1}
\tag{4.12}
$$

which is the Heisenberg Hamiltonian with anti-ferromagnetic coupling, restricted in the ground-state subspace. In conclusion, the hopping Hamiltonian in the strong coupling limit of the Hubbard model acts as an antiferromagnetic interaction. States with anti-aligned neighbouring spins are favoured since they allow hopping phenomena, as sketched in Figure 4.1.

Lattice generalization

So far we considered only two lattice sites. However, all our arguments can be generalised in a straightforward manner to lattices without frustration. When we can draw a spin pattern of anti-aligned neighbours we say that the magnetic ordering is commensurate to the lattice, meaning

Figure 4.1: Hopping phenomena contributing to second-order corrections of the strong-coupling hamiltonian. Pauli's principle enforces these terms to vanish in ferromagnetic configurations: antiferromagnetic ordering is energetically favoured and the ground-state degeneracy is relieved.

that the periodicity of the atoms and the periodicity of the magnetic order are commensurate. In such case, perturbation lifts the degeneracy of the ground state selecting these anti-aligned spin patterns, where each couple of sites i,j can be treated separately, in the same manner explained before. The effective Hamiltonian will be a summation of Hamiltonian Eq.4.12, over all the couples $\langle i, j \rangle$ of neighbouring sites, resembling exactly the Heisenberg Hamiltonian. On the contrary, when a spin pattern of anti-aligned neighbours cannot be drawn we say that the antiferromagnet is frustrated by the lattice geometry. The perturbation selects a large number of states, none of which is optimal: the ground state of the effective Hamiltonian is highly degenerate, and some neighbour spins might be aligned. In this case, we say that magnetic ordering and the lattice are incommensurate. Generalising the effective Hamiltonian to these models can be hard. However, the previous derivation for a single couple of sites holds, and it gives crucial insight regarding the interaction at the fundamental level, which is antiferromagnetic.

Graphene Honeycomb lattice at half filling is a perfect host for antiferromagnetic ordering since commensurate magnetic order can exist. It's therefore reasonable to expect the spontaneous mass generation of M_{303} in graphene when Coulomb electron-electron repulsion becomes relevant. Numerical simulations allowed to detect the phase transition between the insulating and semimetallic phase, for hopping amplitude t in the interval $4 \leq U/t \leq 5$. Rough estimations of U and t in graphene result in $U/t \sim 2 - 4$, indicating the absence of the gap. We notice however that the regime is close to the phase transition, suggesting that slight modification of the model might result in a spontaneous gap opening.

In a recent work Semenoff expanded the previous argument of the Hubbard model to a long-range Coulomb interaction [45]:

$$V = \alpha \sum_{i \neq j} \rho_i \frac{1}{|x_i - x_j|} \rho_j \qquad\qquad \rho_i = c_i^\dagger c_i - 1 \qquad\qquad (4.13)$$

Combining analytical arguments and numerical simulations, the predictions of the Hubbard model on the effective interaction are confirmed: the first relevant correction is the Heisenberg AFM

Hamiltonian. The ground state and the excitation (particle-hole pair) of the two models correspond. In the Hubbard model however, the excitation energy does not depend on the distance between the hole and the excited electron, while in the Coulomb interaction the two attract each other. This makes the ground state of the Coulomb interaction more stable.

4.1.2 The extended Hubbard model in kagome metals promotes the resonating plaquette phase

Kagome lattice at half filling belongs to the second category of lattices: its geometry frustrates the anti-ferromagnetic ordering. In the context of this thesis work we consider however low-energy interaction at the Dirac points, and we focus on $1/3$ filling. In this last case, certain periodic orderings are possible. We review a recent work by Pollmann, where the extended Hubbard model on the kagome lattice is considered [59]. Compared to the standard Hubbard model, repulsion between electrons at neighbouring sites is included, making the model a better approximation of the Coulomb interaction on a discrete lattice.

$$H = -t \sum_\sigma \sum_{\langle i,j \rangle} c_{i\sigma}^\dagger c_{j\sigma} + U \sum_i n_{i\uparrow} n_{i\downarrow} + V \sum_{\sigma,\eta} \sum_{\langle i,j \rangle} n_{i\sigma} n_{j\eta} \tag{4.14}$$

As long as $U > V > 0$ the argument line of the previous section remains consistent. The ground state for $t = 0$ is given by electrons sitting at different sites. The extension of the Hubbard model (repulsion between NN) ensures 2 electrons for each triangle, in order to lower the overall repulsion energy. This unperturbed ground state is highly degenerate: the usual spin degeneracy gets multiplied by the additional freedom of placing two electrons on each triangle, which grows exponentially with the size of the system. The authors use the same methods of the previous section, including perturbatively the hopping Hamiltonian to lift the degeneracy. Perturbations in t/V and $t/(U - V)$ are considered. Again, first-order corrections vanish. Second and third-order perturbations are taken into account, resulting in two effective Hamiltonians: The Heisenberg interaction, and the ring exchange. The former is given by

$$H_{\text{spin}} = J \sum_{\langle ij \rangle} \left(\vec{S}_i \cdot \vec{S}_j - \frac{1}{2} n_i n_j \right) \qquad\qquad J = \frac{2t^2}{U - V} + \frac{2t^3}{V^2} \tag{4.15}$$

The latter describes the simultaneous hopping of three electrons on the hexagon, sitting on every other site:

$$H_{\text{ring}} = g \sum_{\bigcirc} \sum_{\sigma,\sigma'\sigma''} c_{i\sigma}^\dagger c_{j\sigma} c_{k\sigma'}^\dagger c_{l\sigma'} c_{m\sigma''}^\dagger c_{n\sigma''} + h.c. \qquad\qquad g = \frac{6t^3}{V^2} \tag{4.16}$$
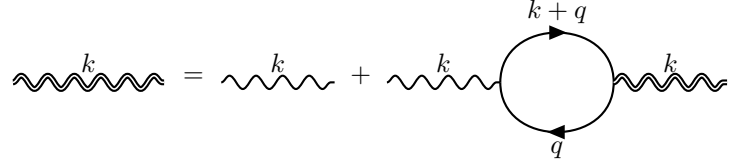
where i,j,k,l,m,n are sites oriented clockwise on the hexagon $\bigcirc$.

The two interactions have different perturbative orders in t, but they both may be relevant, depending on the relative values of U and V. Note indeed that the two amplitudes g and J are independent, because of the freedom on U and V. For $t > 0$ the spin exchange is always anti-ferromagnetic. Depending on which interaction dominates, the ground states might look different (compare Figures 3.6,3.7). When ring interaction wins, three spins resonate on each hexagon, occupying every other site and pointing in the same direction. Anti-aligned spins sit at the corners outside of the hexagon. The resulting spin ordering has a larger magnetic cell, which is a multiple of the lattice unit cell. We then conclude that kagome lattice at $1/3$ filling can show commensurate magnetic order. The two phases correspond to spin-dependent mass terms when treated in mean field theory. Since the (extended) Hubbard model mimics a repulsion between electrons we expect this mass to spontaneously emerge when the Coulomb interaction is large enough.

Is the strong-coupling limit relevant?   The calculations considered in the first part of the present section rely on the strong coupling limit, where interactions between electrons are much larger than the hopping amplitude. The framework of the present thesis is placed instead on the opposite limit, where interaction effects are added perturbatively to a theory of free electrons. One may wonder whether is meaningful to look at the former limit while being rooted in the latter. The answer is two-fold. The strong coupling limit gives a powerful insight about the interaction when other effects are weak. This can be extremely useful to picture the interaction features at the fundamental level. Additionally, since the phase transition between the semimetallic and insulating phases sits in between these two limits it is reasonable to look at instabilities from the opposite perspective. However, the presence of additional phases in the medium range cannot be excluded.

4.2   Spontaneous dimerization of kagome lattice

We report a recent study on the kagome lattice, where the dimerization instability $\mathcal{M}_{302}$ is considered [61]. The authors start from the tight-binding Hamiltonian of non-interacting electrons, and perturbatively add coulomb interaction effects. In quantum field theory, this can be done considering all the Feynman diagrams which contribute to the two-point functions. Since they are infinitely many, some approximations have to be done. One important is named "Random Phase Approximation" (RPA), which takes into account the screening due to the polarization of the neutral background (particle-hole excitations, described by the bubble diagram of fermion lines). In other words, the electron-electron interaction gets screened by other electrons and nuclei, which constitute the background. This approximation is valid when the density of charge carriers is high. The interaction line V^{RPA} is obtained self-consistently using the following renormalization procedure, which describes an effective interaction:

$$(4.17)$$

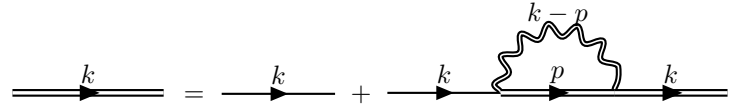Note that such relation resembles a Schwinger-Dyson equation for the interactin line. Its solution is given by

$$V_{RPA}(k) = \frac{V_C(k)}{1 - V_C(k)\Pi(k,\omega)}$$

$$V_C(q) = -\alpha \frac{4\pi\hbar v_F}{q^2}$$

$$(4.18)$$

where $V_C(q)$ is the Coulomb interaction in Fourier space, and the fine structure constant α encodes the interaction strength. The polarization function is given by the bubble diagram:

$$\Pi(k,\omega) = -2 \int \frac{d\nu}{2\pi} \int \frac{d^2q}{(2\pi)^2} G_0(k+q,\omega+\nu)G_0(q,\nu) \tag{4.19}$$

The fermion propagator G is approximated in the following Schwinger-Dyson equation:

$$(4.20)$$

which solution is

$$G(k,\omega) = \frac{G_0(k,\omega)}{1 + G_0(k,\omega)\Sigma(k)} \tag{4.21}$$

It is worth noticing that the interacting Green's function for the electrons resembles the self-consistent Fock approximation, where however the interaction line is "dressed" (i.e. renormalised according to Equation 4.17). The RPA approximation is therefore infinite-order in the Coulomb interaction.

The key of the reviewed study is to associate the self-energy of Eq. 4.20 to the perturbation in tight-binding theory of kagome materials:

$$\delta H(k) = \Sigma(k) = \int \frac{d^2p}{(2\pi)^2} \int \frac{d\nu}{2\pi} V^{RPA}(k-p)G(p,\nu) \tag{4.22}$$

$$\delta H(k) = 2i\eta \begin{pmatrix} 0 & \sin(k \cdot \delta_{ab}) & \sin(k \cdot \delta_{ac}) \\ -\sin(k \cdot \delta_{ab}) & 0 & \sin(k \cdot \delta_{bc}) \\ -\sin(k \cdot \delta_{ac}) & -\sin(k \cdot \delta_{bc}) & 0 \end{pmatrix} \tag{4.23}$$

The propagator G can be written in terms of the band equation $E[p, \eta(p)]$ which depends on the gap η. Equations 4.22,4.23 lead to the self-consistent equation for the gap width:

$$\eta(k) = -\int_{BZ} \frac{d^2p}{(2\pi)^2} \frac{\sin(p \cdot \delta_{ab})}{\sin(k \cdot \delta_{ab})} \frac{V^{RPA}(k-p)}{2E(p, \eta(p))} \eta(p) \tag{4.24}$$

This last equation can be numerically solved at the Dirac points for different values of α, i.e. the strength of the Coulomb interaction. The authors detect a phase transition occurring at $\alpha_c \approx 1.224$: for subcritical interaction $(\alpha < \alpha_c)$ the gap is closed and the system is in the semimetallic phase; the mass is generated when the interaction is stronger than the critical one, as shown in Figure 4.2.
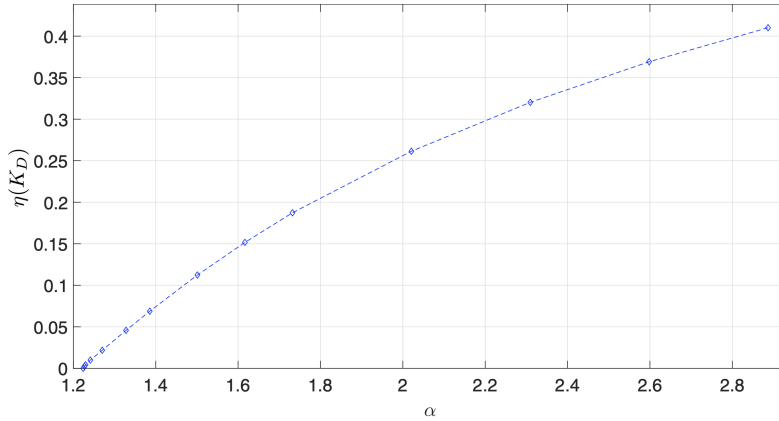

Figure 4.2: Dimerization gap at the Dirac point, as a function of the fine structure constant (numerical solutions of the self-consistent equation Eq.4.24). At $\alpha_c \approx 1.224$ a semimetal-insulator phase transition occurs. Image is taken from [61].

Chapter 5

Conclusions

Motivated by recent attention on kagome materials we addressed the behaviour of free electrons on such structures, with reference to a similar and well-known material, graphene. We, therefore, considered the tight-binding model of electrons on the honeycomb and kagome lattice, which host massless, Dirac quasiparticles at specific fillings. We included three degrees of freedom in the low-energy description, namely spin, valley and sublattice. From first-principle calculations, we derived two families (for the two lattices) of sixteen bilinear Hamiltonians which open a gap at the Dirac points. When such terms are present the quasiparticles gain mass, and the system is driven from a semimetallic to an insulating phase. In the second chapter, we implemented operators for the reflection and rotation symmetries of the lattice, along with additional symmetries of the quantum Hamiltonians (time reversal, charge and chiral symmetry). The mass terms have been classified according to the symmetries they break and preserve. In this context, we investigated a non-trivial feature of the TB Hamiltonian, and its low-energy approximations. Each valley can be chosen between three "equivalent" Dirac points of the Brillouin zone, but lattice symmetries such as rotations or reflections mix these points. One result of our work is to identify the gauge transformation which relates low-energy Hamiltonians expanded around different Dirac points, and therefore to characterise their equivalence with a gauge symmetry.

Leveraging the classification in terms of symmetry breaking, we found a physical interpretation for the unknown mass terms and we reviewed in detail the ones previously studied. Each of the sixteen mass terms of graphene and kagome semimetals has therefore been related to one specific effect or interaction. A similar discussion was partially present in the literature on graphene, but unknown at the time of writing for kagome materials. The main remarks of this investigation are resumed as follows. The anomalous Hall effect (Haldane's model) and the quantum spin-Hall effect (spin-orbit coupling), originally proposed in graphene, are promoted in kagome materials with similar consequences: the gap is open and a topological, insulating phase is obtained. Contrarily to graphene however, these effects are relevant in the kagome lattice already for nearest-neighbour hoppings, which indicates the latter as a prominent host for these phenomena. A different category of instabilities concerns lattice deformation, which is peculiar for the following reason. The kagome lattice at 1/3 filling can be mapped into a dimer model on the honeycomb lattice of graphene; remarkably, this relation emerges explicitly in the two families of masses: terms living on the lattice sites of graphene have a correspondent living on the bond of kagome materials, and viceversa. The simplest, gap-opening lattice deformations are represented by a staggered potential in graphene and a dimerization of the kagome lattice. Moreover, we considered distortion patterns with enlarged unit cells that couple the two valleys in momentum space, such as O-type Kekulé patterns. Again, such patterns open a gap in the two materials in two conjugate ways: Graphene quasiparticles

become massive because of the hopping amplitude distortion, while kagome ones thanks to on-site potential with identical periodicity. This fact gives an indication of the characteristic regimes where these masses might be relevant: any small dimerization results in a finite gap for graphene; the periodic, on-site potential instead, (kagome mass) becomes a meaningful description in strongly-dimerized structures. As last, we compared masses originating from antiferromagnetic interaction. Honeycomb lattice at 1/2 filling is a perfect host for Néel ordering, and a mean-field treatment reveals the trivial gapped nature of the antiferromagnetic phase. More sophisticated conclusions regard kagome materials; because of the magnetic frustration originating in the corner-sharing triangles, the antiferromagnetic interaction might generate exotic magnetic phases, such as spin-liquids. In this work, however, we focus on 1/3 filling of the kagome lattice, with, on average, 2 electrons for each triangle. The presence of empty sites leaves space for different antiferromagnetic orderings. We explored the resonating plaquette phase, characterised by enlarged magnetic cells, and known to emerge in the strong-coupling limit. Similarly to graphene, a mean-field treatment reveals the gapped nature of this phase. In the conclusive chapter, we discussed spontaneous mass generation: we showed how the antiferromagnetic exchange can be derived in the strong-coupling limit as a perturbative correction to the Hamiltonian, and we reviewed a study on spontaneous lattice dimerization of kagome, which is obtained in mean-field theory in the weak-coupling limit. Additionally, we characterise all the masses with the respective symmetry breaking (time reversal, charge, chiral symmetry) with one exception, i.e. the Kekulé dimerization pattern which mixes the two valleys and opens a gap by merging the two independent Dirac points. Remarkably, this last mechanism leaves intact the symmetries of the low-energy Hamiltonian.

In conclusion, the relationship between graphene and kagome structures, which proved to be complex and multifaced, gives precious indications about the relevant instabilities of these materials. These insights, together with the characterisation of masses in terms of symmetries and their physical interpretation, are powerful tools to address the the spontaneous gap opening and estimate the conductive behaviours of real materials.

Acknowledgements

Appendix A

Computational methods

The linearisation of the TB Hamiltonian, the identification of the mass terms and their classification in terms of symmetries have been performed using `Wolfram Mathematica` [64]. Here we report some of the principal routines for the Kagome lattice. The case of graphene is equivalent, with a simplification: there are two sublattices, and there is no need to decouple the flat band.

TB Hamiltonian and low-energy approximation

```
1  (* Lattice vectors & TB Hamiltonian *)
2  deltaAB = {1, 0};
3  deltaAC = 1/2 {1, Sqrt[3]};
4  deltaBC = 1/2 {-1, Sqrt[3]};
5  HNL[kkx_, kky_] :=  {{0, Cos[{kkx, kky}.deltaAB], Cos[{kkx, kky}.deltaAC]},
6                      {Cos[{kkx, kky}.deltaAB],  0, Cos[{kkx, kky}.deltaBC]},
7                      {Cos[{kkx, kky}.deltaAC], Cos[{kkx, kky}.deltaBC], 0}};
8
9  (* Routine to expand the TB Hamiltonian HNL around the Dirac points Kd_, KdPrime_ *)
10 Hexpand[kkx_, kky_, Kd_, KdPrime_] := Module[{H1, H2, HValley},
11    (* Expanding around the first valley Kd_ *)
12    H1[kkx, kky] := Normal[ Series[
13       2 HNL[Kd[[1]] + kkx t, Kd[[2]] + kky t], {t, 0, 1}]] /. t -> 1 ;
14    (* Expanding around the second valley KdPrime_ *)
15    H2[kkx, kky] := Normal[ Series[
16       2 HNL[KdPrime[[1]] + kkx t, KdPrime[[2]] + kky t], {t, 0, 1}]] /. t -> 1 ;
17
18    HValley[kkx, kky] :=   (* Putting together the two valleys *)
19        KroneckerProduct[ {{1, 0}, {0, 0}}, H1[kkx, kky]] +
20        KroneckerProduct[ {{0, 0}, {0, 1}}, H2[kkx, kky]];
21    (* Return: *)
22    KroneckerProduct[
23        PauliMatrix[0],        (* Spin dof *)
24        HValley[kkx, kky]]     (* Valley + Subl. dof *)
25    ];
```

Derivation of the mass terms

```
1  (*  Mass term operator M_{ijk} *)
2  M[i_, j_, k_] := KroneckerProduct[
3          PauliMatrix[i],
4          PauliMatrix[j],
5          PauliMatrix[k]
6  ];
7
8  (* Routine to find the mass terms *)
9  Anticomm[ A_, B_] := A.B + B.A;        (* Anticommutation operation *)
10 allowedindeces = {0, 1, 2, 3};         (* Indices of Pauli matrices *)
11 gaps = {};
12 h0 = vf ( k1 M[0, 3, 3] + k2 M[0, 3, 1]);
13
14 Do[
15     If[ FullSimplify[ Anticomm[h0, M[i, j, k]]] === 0 IdentityMatrix[8],
16         AppendTo[gaps, {i, j, k}]],
17     {i, allowedindeces}, {j, allowedindeces}, {k, allowedindeces}
18 ];
```

Embedding the mass terms in the full Hilbert space

```
1  (* Routine for increasing the dimension to 3 sublattices *)
2  from2to3[A_] := Module[ {M},
3      M = Table[ Join[{0}, A[[i]] ], {i, 1, 2}];
4      M = Join[ {{0, 0, 0}}, M];
5      M
6  ]
7  increaseDim[i_, j_, k_] := Module[{A, M},
8      M = from2to3[PauliMatrix[k]];
9      A = KroneckerProduct[
10         PauliMatrix[i], (* Spin dof *)
11         PauliMatrix[j], (* Valley dof *)
12       M];              (* Sublattice dof *)
13     A
14 ]
```

Checking the symmetry of the mass terms

```
1  (* Routine for checking the reflection symmetry E1 of the mass terms *)
2  checkE1 = Table[  Module[{mass, bool},
3      (* Embedding the mass term in the full Hilbert space H_3 *)
4      mass = increaseDim[ gaps[[i, 1]], gaps[[i, 2]], gaps[[i, 3]] ];
5      (* Transforming back to original lattice basis  *)
6      mass = Inverse[U14].mass.U14;
7      (* Checking the symmetry  *)
8      bool =  FullSimplify[ E1.mass ] === FullSimplify[ mass.E1] ;
9      bool
10     ], {i, 1, Length[gaps]}]
```

Bibliography

Introduction

[1]   Anthony Zee. *Quantum field theory in a nutshell*. Vol. 7. Princeton university press, 2010.

[2]   N. W. Ashcroft and N. D. Mermin. *Solid State Physics*. Holt-Saunders, 1976.

[3]   Gerald D Mahan. *Many-particle physics*. Springer Science & Business Media, 2013.

[4]   Henk TC Stoof, Koos B Gubbels, and Dennis Dickerscheid. *Ultracold quantum fields*. Springer, 2009.

[5]   Richard D Mattuck. *A guide to Feynman diagrams in the many-body problem*. Courier Corporation, 1992.

[6]   Xiao-Gang Wen. *Quantum field theory of many-body systems: from the origin of sound to an origin of light and electrons*. OUP Oxford, 2004.

[7]   Jean Zinn-Justin. *Quantum field theory and critical phenomena*. Vol. 171. Oxford university press, 2021.

[8]   Stefano Forte and Luca Rottoli. *Fisica quantistica*. Zanichelli, 2018.

[9]   Palash B Pal. "Dirac, majorana, and weyl fermions". In: *American Journal of Physics* 79.5 (2011), pp. 485–498.

[10]   Steve M Young and Charles L Kane. "Dirac semimetals in two dimensions". In: *Physical review letters* 115.12 (2015), p. 126803.

[11]   NP Armitage, EJ Mele, and Ashvin Vishwanath. "Weyl and Dirac semimetals in three-dimensional solids". In: *Reviews of Modern Physics* 90.1 (2018), p. 015001.

[12]   KS Novoselov et al. "Room-temperature electric field effect and carrier-type inversion in graphene films". In: *arXiv preprint cond-mat/0410631* (2004).

[13]   NMR Peres. "Graphene, new physics in two dimensions". In: *Europhysics News* 40.3 (2009), pp. 17–20.

[14]   Franz Utermohlen. "Tight-Binding Model for Graphene". In: (2018).

[15]   A. H. Castro Neto et al. "The electronic properties of graphene". In: *Reviews of Modern Physics* 81.1 (2009), pp. 109–162. DOI: `10.1103/revmodphys.81.109`.

[16]   MI Katsnelson, KS Novoselov, and AK Geim. "Chiral tunnelling and the Klein paradox in graphene". In: *Nature physics* 2.9 (2006), pp. 620–625.

[17]   Mildred S Dresselhaus et al. "Carbon nanotubes". In: *The physics of fullerene-based and fullerene-related materials*. Springer, 2000, pp. 331–379.

[18]   Sumathi Rao. "Weyl semi-metals: a short review". In: *arXiv preprint arXiv:1603.02821* (2016).

[19]   MR Norman. "Colloquium: Herbertsmithite and the search for the quantum spin liquid". In: *Reviews of Modern Physics* 88.4 (2016), p. 041002.

[20]   Lucile Savary and Leon Balents. "Quantum spin liquids: a review". In: *Reports on Progress in Physics* 80.1 (2016), p. 016502.

[21]   C Mielke III et al. "Nodeless kagome superconductivity in LaRu 3 Si 2". In: *Physical Review Materials* 5.3 (2021), p. 034803.

[22]   Mingu Kang et al. "Topological flat bands in frustrated kagome lattice CoSn". In: *Nature communications* 11.1 (2020), pp. 1–9.

[23]   II Mazin et al. "Theoretical prediction of a strongly correlated Dirac metal". In: *Nature communications* 5.1 (2014), pp. 1–7.

[24]   Linda Ye et al. "Massive Dirac fermions in a ferromagnetic kagome metal". In: *Nature* 555.7698 (2018), pp. 638–642.

[25]   Riccardo Ciola. "Chiral Symmetry Breaking in Novel Kagome Materials". MA thesis. 2021.

Symmetries

[26]   Anthony Zee. *Group theory in a nutshell for physicists*. Vol. 17. Princeton University Press, 2016.

[27]   Ramón J Flores. "Classifying Spaces for Wallpaper Groups". In: *Geometric Group Theory*. Springer, 2007, pp. 51–64.

[28]   Adolfo Grushin. "Introduction to topological Phases in Condensed Matter". In: *Lecture notes* ().

[29]   Andreas W W Ludwig. "Topological phases: classification of topological insulators and superconductors of non-interacting fermions, and beyond". In: *Physica Scripta* T168 (2015), p. 014001. DOI: 10.1088/0031-8949/2015/t168/014001.

[30]   Ching-Kai Chiu et al. "Classification of topological quantum matter with symmetries". In: *Reviews of Modern Physics* 88.3 (2016). DOI: 10.1103/revmodphys.88.035005.

[31]   János K Asbóth, László Oroszlány, and András Pályi. "A short course on topological insulators". In: *Lecture notes in physics* 919 (2016), p. 166.

[32]   Martin R. Zirnbauer. "Particle–hole symmetries in condensed matter". In: *Journal of Mathematical Physics* 62.2 (Feb. 2021), p. 021101. DOI: 10.1063/5.0035358. URL: https://doi.org/10.10632F5.0035358.

Mass terms

[33]   Claudio Chamon et al. "Masses and Majorana fermions in graphene". In: *Physica Scripta* T146 (2012), p. 014013. DOI: 10.1088/0031-8949/2012/t146/014013.

[34]   Joon-Suh Park and Hyoung Joon Choi. "Band-gap opening in graphene: A reverse-engineering approach". In: *Physical Review B* 92.4 (2015), p. 045402.

[35]   Gordon W Semenoff. "Condensed-matter simulation of a three-dimensional anomaly". In: *Physical Review Letters* 53.26 (1984), p. 2449.

[36] F. D. M. Haldane. "Model for a Quantum Hall Effect without Landau Levels: Condensed-Matter Realization of the "Parity Anomaly"". In: *Phys. Rev. Lett.* 61 (18 Oct. 1988), pp. 2015–2018. DOI: 10.1103/PhysRevLett.61.2015. URL: https://link.aps.org/doi/10.1103/PhysRevLett.61.2015.

[37] Charles L Kane and Eugene J Mele. "Quantum spin Hall effect in graphene". In: *Physical review letters* 95.22 (2005), p. 226801.

[38] Claudio Chamon. "Solitons in carbon nanotubes". In: *Physical Review B* 62.4 (2000), p. 2806.

[39] Chang-Yu Hou, Claudio Chamon, and Christopher Mudry. "Electron fractionalization in two-dimensional graphenelike structures". In: *Physical review letters* 98.18 (2007), p. 186809.

[40] Zhi-Cheng Yang et al. "Hierarchical Majoranas in a programmable nanowire network". In: *Physical Review B* 99.15 (2019), p. 155138.

[41] OV Gamayun et al. "Valley-momentum locking in a graphene superlattice with Y-shaped Kekulé bond texture". In: *New Journal of Physics* 20.2 (2018), p. 023016.

[42] Gilles Montambaux et al. "Merging of Dirac points in a two-dimensional crystal". In: *Physical Review B* 80.15 (2009), p. 153412.

[43] Vitor M Pereira, AH Castro Neto, and NMR Peres. "Tight-binding approach to uniaxial strain in graphene". In: *Physical Review B* 80.4 (2009), p. 045401.

[44] Giulio Cocco, Emiliano Cadelano, and Luciano Colombo. "Gap opening in graphene by shear strain". In: *Physical Review B* 81.24 (2010), p. 241412.

[45] Gordon W Semenoff. "Chiral symmetry breaking in graphene". In: *Physica Scripta* T146 (Jan. 2012), p. 014016. DOI: 10.1088/0031-8949/2012/t146/014016.

[46] Indrani Bose. "Spin gap antiferromagnets: materials and phenomena". In: *Current Science* (2005), pp. 62–70.

[47] Oleg V Yazyev. "Emergence of magnetism in graphene materials and nanostructures". In: *Reports on Progress in Physics* 73.5 (2010), p. 056501.

[48] Xueyang Li et al. "Spin Hamiltonians in magnets: Theories and computations". In: *Molecules* 26.4 (2021), p. 803.

[49] Valeri N Kotov et al. "Electron-electron interactions in graphene: Current status and perspectives". In: *Reviews of modern physics* 84.3 (2012), p. 1067.

[50] Guocai Liu et al. "Simulating and detecting the quantum spin Hall effect in the kagome optical lattice". In: *Physical Review A* 82.5 (2010), p. 053605.

[51] Naoto Nagaosa et al. "Anomalous hall effect". In: *Reviews of modern physics* 82.2 (2010), p. 1539.

[52] FDM Haldane. "Berry curvature on the fermi surface: Anomalous hall effect as a topological fermi-liquid property". In: *Physical review letters* 93.20 (2004), p. 206602.

[53] Jinwu Ye et al. "Berry phase theory of the anomalous Hall effect: application to colossal magnetoresistance manganites". In: *Physical review letters* 83.18 (1999), p. 3737.

[54] Y Taguchi et al. "Spin chirality, Berry phase, and anomalous Hall effect in a frustrated ferromagnet". In: *Science* 291.5513 (2001), pp. 2573–2576.

[55] Kamil K Kolincio et al. "Kagomé lattice promotes chiral spin fluctuations". In: *arXiv preprint arXiv:2206.05756* (2022).

[56] Kenya Ohgushi, Shuichi Murakami, and Naoto Nagaosa. "Spin anisotropy and quantum Hall effect in the kagomé lattice: Chiral spin state based on a ferromagnet". In: *Physical Review B* 62.10 (2000), R6065.

[57] H-M Guo and M Franz. "Topological insulator on the kagome lattice". In: *Physical Review B* 80.11 (2009), p. 113102.

[58] Satoshi Nishimoto et al. "Metal-insulator transition of fermions on a kagome lattice at 1/3 filling". In: *Physical Review Letters* 104.19 (2010), p. 196401.

[59] Frank Pollmann et al. "Interplay of charge and spin fluctuations of strongly interacting electrons on the kagome lattice". In: *Physical Review B* 90.3 (2014), p. 035118.

[60] SA Nikolaev, IV Solovyev, and SV Streltsov. "Quantum spin liquid and cluster Mott insulator phases in the Mo3O8 magnets". In: *npj Quantum Materials* 6.1 (2021), pp. 1–8.

[61] Riccardo Ciola et al. "Chiral symmetry breaking through spontaneous dimerization in kagomé metals". In: *Physical Review B* 104.24 (2021), p. 245138.

[62] Adrien Bolens and Naoto Nagaosa. "Topological states on the breathing kagome lattice". In: *Physical Review B* 99.16 (2019), p. 165141.

Others

[63] Charles L Cleveland and Rodrigo Medina A. "Obtaining a Heisenberg Hamiltonian from the Hubbard model". In: *American Journal of Physics* 44.1 (1976), pp. 44–46.

[64] Wolfram Research Inc. *Mathematica, Version 13.2*. Champaign, IL, 2022. URL: https://www.wolfram.com/mathematica.